

HARTREE-FOCK-BOGOLIUBOV CALCULATIONS  
FOR NUCLEI FAR FROM STABILITY

By

Edgar Teran Balbuena

Dissertation

Submitted to the Faculty of the  
Graduate School of Vanderbilt University  
in partial fulfillment of the requirements  
for the degree of

DOCTOR OF PHILOSOPHY

in

Physics

May, 2003

Nashville, Tennessee

Approved

Prof. A. Sait Umar

Prof. Volker E. Oberacker

Prof. David J. Ernst

Prof. Akunuri V. Ramayya

Prof. Leonard C. Feldman

## ACKNOWLEDGEMENTS

I would like to acknowledge the training and support I have received during my dissertation research from my main advisor – Dr. Sait Umar. His guidance and expertise have been invaluable. I must also mention the feedback of Dr. Volker Oberacker who, in addition to providing direction, also contributed to this work with his notes on the derivation of a number of equations. I must mention also, the rest of my Ph.D. committee: Dr. David Ernst, Dr. Akanuri A. Rammayya and Dr. Leonard Feldman. Their continuous feedback and interest through our meetings contributed in a special way to the success of the project.

Special thanks are also due to Dr. Jacek Dobaczewski and Dr. Mario Stoitsov. The provision of their results has been tremendously helpful in the development of this work.

I want to thank to my friends in the Physics Department. Our daily discussions help not only to envision my project, but also to learn about projects in other areas of Physics. My wife and daughter receive special thanks for their patience and love. Finally, this work is specially dedicated to my parents, brother and sister, whose constant encouragement has been really important in the success of my academic career.

This work was partially supported under U.S. Department of Energy grant DE-FG02-96ER40963 to Vanderbilt University. Some of the numerical calculations were carried out on Cray supercomputers at the National Energy Research Scientific Computing Center (NERSC).

# TABLE OF CONTENTS

	Page
ACKNOWLEDGEMENTS . . . . .	ii
LIST OF TABLES . . . . .	v
LIST OF FIGURES . . . . .	vi
Chapter	
I. INTRODUCTION . . . . .	1
1.1 Nuclear Landscape . . . . .	1
1.2 Physics near the driplines . . . . .	3
1.3 Pairing and coupling to the continuum . . . . .	5
1.4 HFB contribution to nuclear structure . . . . .	6
1.5 Overview . . . . .	7
II. HARTREE-FOCK-BOGOLIUBOV THEORY . . . . .	9
2.1 Hartree-Fock + BCS . . . . .	10
2.1.1 BCS Equations . . . . .	11
2.2 Standard HFB Formalism . . . . .	13
2.2.1 Quasiparticle wave functions in coordinate space . . . . .	16
Normal density and pairing density . . . . .	18
2.2.2 Kinetic and spin-orbit densities . . . . .	18
2.2.3 Energy functional and mean fields . . . . .	18
2.2.4 Pairing interaction. . . . .	19
2.2.5 HFB equations in coordinate space . . . . .	21
2.3 Two-dimensional Reduction for Axially Symmetric Systems . . . . .	22
2.3.1 Densities and currents . . . . .	25
III. HFB EQUATIONS USING THE SKYRME INTERACTION . . . . .	28
3.1 Standard Skyrme interaction . . . . .	28
3.2 Energy density . . . . .	30
3.3 Single Particle Hamiltonian . . . . .	32
3.3.1 Kinetic Energy Operator . . . . .	33
3.3.2 Nuclear Potential Operator . . . . .	34
3.3.3 Evaluation of the Coulomb Potential . . . . .	35
3.3.4 Spin-orbit Operator . . . . .	35
IV. BASIS SPLINE REPRESENTATION . . . . .	38

4.1	B-Spline representation of functions . . . . .	38
4.1.1	Collocation method . . . . .	39
4.1.2	Representation of the eigenvalue problem . . . . .	40
4.1.3	Basis Spline Galerkin method . . . . .	42
V.	NUMERICAL IMPLEMENTATION . . . . .	44
5.1	Initialization . . . . .	45
5.1.1	Deformed Woods-Saxon potential . . . . .	45
5.2	Description of the main iterative process . . . . .	48
5.3	First test of a trivial case: $^{16}\text{O}$ . . . . .	50
VI.	RESULTS . . . . .	53
6.1	Numerical parameters: $^{22}\text{O}$ calculations . . . . .	53
6.1.1	Energy cutoff . . . . .	53
6.1.2	Lattice box size . . . . .	56
6.1.3	Number of mesh points . . . . .	56
6.1.4	Projection of the angular momentum, $\Omega$ . . . . .	57
6.2	Tests of Axially symmetric HFB results. . . . .	58
6.2.1	Light, spherical nucleus $^{22}\text{O}$ . . . . .	59
6.2.2	Deformed neutron-rich nucleus: $^{102}\text{Zr}$ . . . . .	60
6.2.3	Heavy nucleus $^{150}\text{Sn}$ . . . . .	61
6.3	Analysis of the quasiparticle spectrum in $^{150}\text{Sn}$ . . . . .	63
6.3.1	Quasiparticle states in $^{150}\text{Sn}$ . . . . .	63
6.3.2	$^{150}\text{Sn}$ wavefunctions . . . . .	64
6.4	Calculations in the sulfur isotope chain . . . . .	66
6.4.1	Sulfur dripline . . . . .	66
6.4.2	Skins and Halos . . . . .	69
VII.	CONCLUSIONS . . . . .	72
7.1	Possible future work . . . . .	73
Appendices		
A.	ALTERNATIVE DIAGONALIZATION: SYMMETRIC EIGENVALUE PROBLEM . . . . .	75
B.	EXPECTATION VALUES OF ONE-BODY OPERATORS IN 2-D . . . . .	78
REFERENCES . . . . .		80



## LIST OF TABLES

Table	Page
1. Skyrme parameters for different forces in terms of $x_0, x_1, x_2, x_3, t_0, t_1, t_2, t_3, W_0$ .	29
2. More recent Skyrme parameters for different forces in terms of $b_0, b'_0, b_1, b'_1, b_2, b'_2, b_3, b'_3, b_4, b'_4$ . . . . .	32
3. $^{16}O$ observables for calculations with 1-D HF, 3-D HF, 2-D HF+BCS and 2-D HFB . . . . .	51
4. Calculations for $^{22}O$ with 1-D HFB, 2-D HFB+THO and 2-D HFB . . . . .	59
5. Calculations for $^{102}Zr$ with 2-D HFB+THO and 2-D HFB . . . . .	60
6. Calculations for $^{150}Sn$ with 1-D HFB and 2-D HFB . . . . .	62
7. Sulfur isotopes calculations from A=42 to A=52 . . . . .	66

## LIST OF FIGURES

Figure	Page
1. Nuclear chart showing the number of protons in nuclei vs. number of neutrons	2
2. Schematic nuclear potentials in stable and radioactive nuclei. . . . .	3
3. Angular momentum nuclear Cooper pairs . . . . .	5
4. Prolate and oblate nuclear shapes . . . . .	6
5. Single particle state occupancies for a spherical nucleus and a non-spherical nucleus . . . . .	13
6. Quasiparticle energy spectrum generated by the Hartree-Fock-Bogoliubov solution	22
7. Cylindrical coordinates for the representation of axially symmetric objects . .	23
8. Skyrme forces in two-neutron separation energies calculations of tin isotopes compared with the experimental values . . . . .	36
9. Single spline of order 5 showing the knots and collocation points . . . . .	39
10. Set of order-5 splines with boundary conditions at the extremes showing the position of the knots and the collocation points . . . . .	40
11. One-dimensional neutron potential from Woods-Saxon and from HF+BCS. . .	46
12. Flowchart of the HFB algorithm, including the initialization . . . . .	47
13. $^{22}\text{Ne}$ binding energy evolution for different damping factors . . . . .	49
14. Wavefunctions corresponding to the low-lying states of spherical $^{16}\text{O}$ . . . . .	51
15. Binding energy in $^{22}\text{O}$ vs. quasiparticle cutoff and equivalent single-particle energy cutoff . . . . .	54
16. Binding energy vs. box size ( $R$ ) in $^{22}\text{O}$ . . . . .	55
17. Binding energy, neutron Fermi level and pairing gap vs. number of mesh points in $^{22}\text{O}$ . . . . .	57
18. Binding energy, neutron Fermi level and pairing gap vs. $\Omega_{max}$ in $^{22}\text{O}$ . . . . .	58
19. Two-dimensional intensity plot of the $^{102}\text{Zr}$ total mass density, $\rho(r, z)$ . . . . .	61
20. Quasiparticle energy spectrum and equivalent single particle spectrum for neutrons in $^{150}\text{Sn}$ . . . . .	63

21.	Three-dimensional plots of the $^{150}\text{Sn}$ wavefunctions corresponding to selected neutron states with $\Omega = 1/2$ . . . . .	65
22.	Two-neutron separation energies in sulfur isotopes around the dripline . . . . .	67
23.	Neutron Fermi level in sulfur isotopes near the dripline . . . . .	69
24.	Radial plots of the neutron and proton densities in $^{32}\text{S}$ and $^{48}\text{S}$ . . . . .	70
25.	Two-dimensional intensity plots of the neutron densities of $^{32}\text{S}$ and $^{48}\text{S}$ . . . . .	71

# CHAPTER I

## INTRODUCTION

The nucleus is the core of the atom and contains most of its mass. It determines the chemical nature of the atom through its electrical charge. Atoms, based on their chemical properties, form the molecules, compounds and materials that surround us, and from which living things are made. Understanding the structure of the nucleus is a major challenge.

New discoveries about the properties of the nucleus have been achieved through experimental and theoretical initiatives that push our knowledge of nuclear systems to the limits. Such extreme conditions have included the study of nuclei in terms of atomic number and mass, angular momentum, excitation energy, deformation, temperature. Along with these advances increased computing power and progress in computational techniques have greatly enhanced theoretical progress in addressing the nuclear many-body problem[1].

### 1.1 Nuclear Landscape

Nuclei come in a large variety of combinations of protons and neutrons. However, due to the underlying forces and physical symmetries, only certain combinations are possible. Figure 1 shows the landscape of those nuclei that we presently think might exist. The neutron number is along the horizontal axis and the proton number along the vertical axis. The nuclear chart shows several thousands of nuclei that are expected to be bound by the strong force. The black region shows the stable nuclei, non-radioactive or long-lived, with half lives comparable to, or longer than the age of the earth. There are fewer than 300 such species. This is the *valley of  $\beta$ -stability*. Light nuclei are stable if the number of protons and the number of neutrons are approximately equal. Furthermore, nuclei with N or Z equal to certain numbers show a special stability: the *magic numbers* (the ones labeling the horizontal and vertical red lines in Figure 1). These nuclei are spherical in shape with major nuclear shells closed. While other nuclei found away from the valley of stability are also bound, they are not completely stable. Nuclei with an excess or deficiency of neutrons relative to the

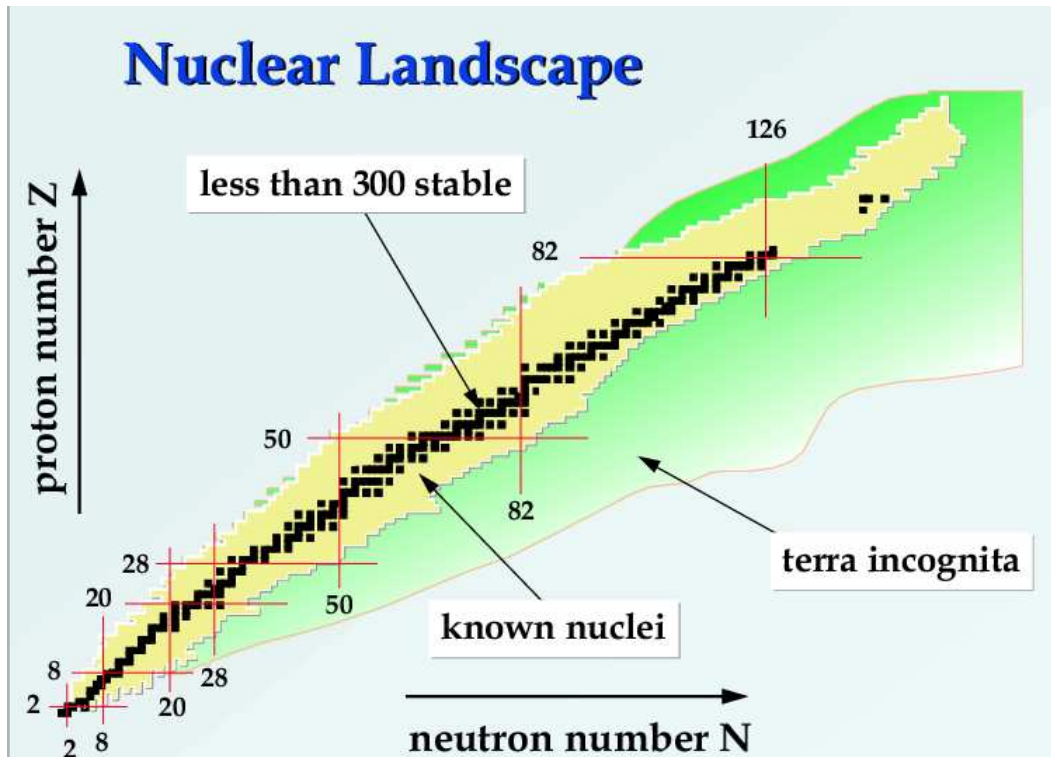


Figure 1: Chart of the nuclides showing the valley of particle stability and the limits of nuclear existence, or driplines.

valley of stability are unstable and therefore decay. The yellow region around the  $\beta$ -stability area in Fig. 1 indicates the man-made nuclei produced in laboratories with short half-lives [2]. Thousands of radioactive nuclei with very small or very large neutron to proton ratios are yet to be explored (*terra incognita*, indicated by the green area in Fig. 1). By adding protons or neutrons ( $\beta$ -decay) we move away from the valley of stability, finally reaching the *driplines* -where the nuclear binding ends. The forces between protons and neutrons are no longer strong enough to hold them together. The proton dripline is already determined experimentally up to  $Z=83$ . On the other hand, the neutron dripline is considerably further from the valley of stability and harder to approach. The width difference of the proton and neutron driplines with respect to the stability line is explained by the repulsive Coulomb force, which gains strength as more protons are added. The driplines have been predicted heuristically but are strongly model-dependent. Calculation of nuclear properties far from

stability, based on the experience gained by studying stable nuclei, is an important and difficult challenge to nuclear structure theory.

## 1.2 Physics near the driplines

The scientific community has clearly identified that the exploration of the structure of radioactive nuclei far from stability represents a new frontier in our understanding of nuclear structure and nuclear astrophysics[1].

For nuclei far from stability, the relevant experimental data are almost nonexistent, especially on the neutron-rich side. Until recently, the use of nuclei as beams has almost always been restricted to stable nuclei. Radioactive ion beams (RIB) will enable the exploration of a few thousand new nuclides. RIB facilities aim at opening a new era for nuclear physics, providing us with an opportunity to study the properties of nuclei in a wide range of proton and neutron number combinations and are expected to give access to the limits of nuclear existence.

Unlike the well-understood behavior of nuclei near the valley of stability, there are still many unknown phenomena as we move towards the proton and neutron driplines and the mass number limits (superheavy region).

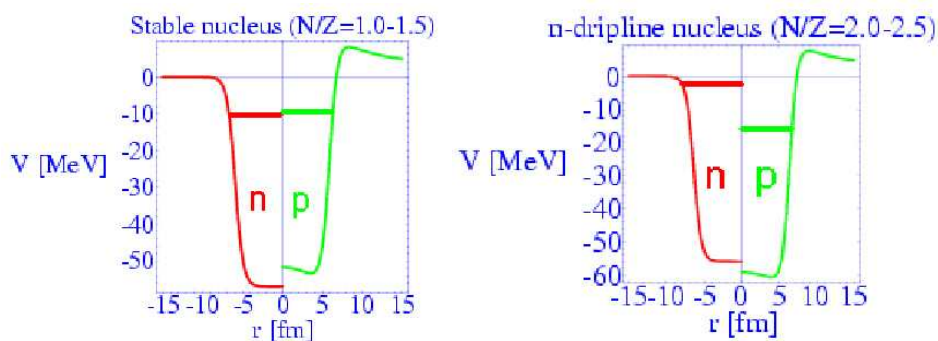


Figure 2: Nuclear potential for protons and neutrons in a typical stable nucleus, and another nucleus near the neutron dripline.

On the neutron-rich side, the dripline has been approached only for the lightest nuclei [3]. In contrast with proton-rich systems, which are stabilized by the Coulomb barrier, nuclei close to the neutron dripline are very weakly bound and, consequently, are very extended spatially. Hence, the influence of the particle continuum is very important.

As stated above, in the exotic regions of the nuclear chart (driplines, superheavy region), new phenomena are yet to be explored [4]. Near the neutron dripline, the neutron distribution of nuclei starts to diffuse out, making the nuclear surface less defined and giving rise to low density *neutron halos* and *neutrons skins*. Furthermore, in proton-rich nuclei, we have recently seen both spherical and deformed proton emitters; the observed *proton radioactivity* is caused by the tunneling of weakly bound protons through the Coulomb barrier.

Some differences can be observed for nuclei with high isospin (i.e. neutron to proton ratio) in comparison to nuclei in the valley of stability (see Fig. 2): 1)unstable nuclei show large neutron o proton excess; 2)the separation energy of one nucleon is not as constant with increasing nucleon number; 3)the spatial distribution is quite different for protons and neutrons (e.g. halo or skin are formed).

With RIB facilities, nuclear theorists see an opportunity to study the effective nucleon-nucleon interaction at large isospin, as well as large pairing correlations. It is generally acknowledged that an accurate treatment of the pairing interaction is essential for describing exotic nuclei [5, 6]. The present work specifically aims to calculate the ground state observables for even-even nuclei. The associated variables include the total binding energy, charge radii, proton and neutron densities, separation energies for neutrons and protons and pairing gaps. Besides the theoretical and experimental interest in the nuclear physics aspects of exotic nuclei, calculations for nuclei far from stability have strong physical implications for astrophysical nucleosynthesis processes, e.g. the *r*-process [7, 8].

In order to understand the nature of the nuclear structure, it becomes essential to explore and study not only the behavior of the well-known stable nuclei, but also those near the driplines.

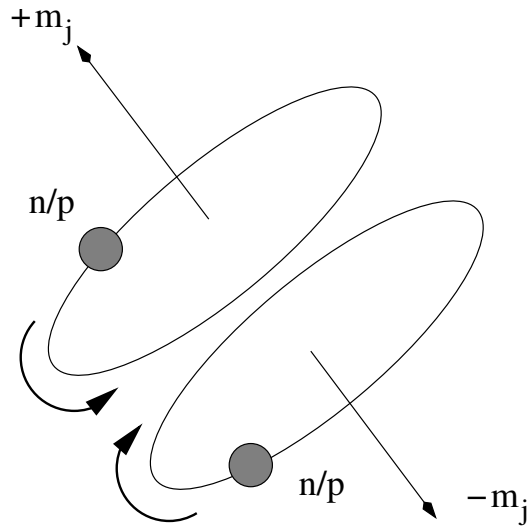


Figure 3: The nuclear Cooper pairs in angular momentum are analogous to the linear momentum pairs in condensed matter

### 1.3 Pairing and coupling to the continuum

As mentioned above, nuclei close to the limit of nuclear existence present interesting features. The most difficult implications from the point of view of theoretical modeling arise from the strong pairing correlations and coupling to the continuum. As nuclei move away from stability and approach the driplines, the corresponding Fermi surface gets closer to zero, as seen in Figure 2. A significant number of the available single-particle states then form part of the continuum. Several approximations in the mean field theory (using quasiparticles) have been used to address the physics of the pairing correlations (e.g. BCS and Lipkin-Nogami), but have failed to converge for far-from-stability-line nuclei. The Hartree-Fock-Bogoliubov theory provides a considerable framework for the correct treatment of such correlations.

The large pairing correlations near the driplines can no longer be described by a small residual interaction. It becomes necessary to treat the mean field and the pairing field in a single self-consistent theory, i.e. Hartree-Fock-Bogoliubov (HFB). Furthermore, the outermost nucleons are weakly bound, implying a large spatial extent, with these nucleons being strongly coupled to the particle continuum. These features represent major challenges for the mean field theories. We overcome these difficulties by solving the HFB equations



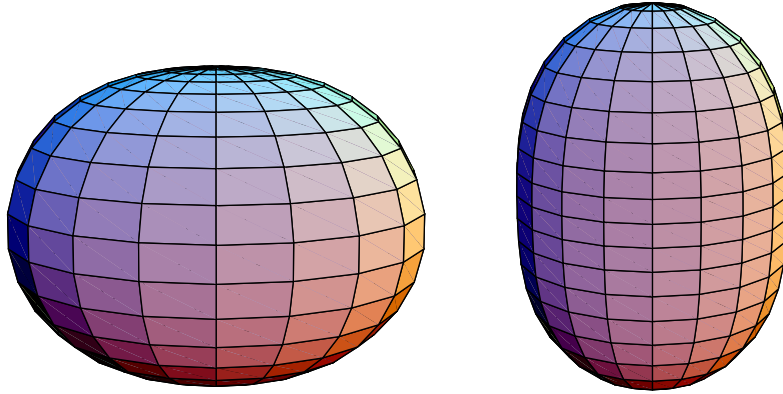


Figure 4: Prolate and oblate shapes of nuclei. The axial symmetry enables the simulation of nuclei with these deformed configurations, including the spherical shape.

for deformed, axially symmetric even-even nuclei on a two-dimensional lattice, without any further approximations.

#### 1.4 HFB contribution to nuclear structure

There are several types of approaches in nuclear structure theory [9]: for the lightest nuclei, ab-initio calculations (Green's function - Monte Carlo shell model) based on bare N-N interaction are possible [10]. Medium-mass nuclei up to  $A \sim 60$  may be treated in the large-scale shell model [11]. For heavier nuclei one utilizes either nonrelativistic [5, 12, 13] or relativistic [14, 15, 16] mean field theories.

In the framework of HFB theory, several approaches have already been applied to nuclear calculations. For some time, one-dimensional HFB calculations in coordinate space have been performed, producing very interesting results [5, 6]. However, the radial code used for such calculations is limited because it imposes a spherical symmetry. This approach has obvious unrealistic assumptions for nuclei that have a considerable degree of deformation (see Fig.4 ). Another attempt to solve the HFB equations in coordinate space has been made in three dimensional symmetry[17, 18]. These calculations have been successful in describing triaxial deformations for some nuclei near the neutron dripline, with states in the continuum *only*

up to 5 MeV. For some light nuclei this is sufficient, but not for heavy nuclei near the driplines. Recently, a configurational code in the harmonic oscillator (HO) basis [19, 20] has successfully been tested with axial symmetry. However, the HO basis of this code is very limited for representing the wavefunctions of nuclei away from stability. Although a nice approximation of axially deformed calculations, it remains unreliable for describing dripline nuclei.

The coordinate-space, axially-symmetric calculations shown in this work represent a consistent description of axial deformations, which are present in many nuclei [21]. The two-dimensional code presented here specifically addresses the computational challenges encountered with nuclei near the driplines.

## 1.5 Overview

The work presented in this thesis emphasizes not only the nuclear structure theory, but also the numerical methods involved in the development of the code used for the calculations.

One of the most important resources in the development of this work is the extensive utilization of Fortran 90/95 programming. Fortran provides features suitable for the kind of numerical representation required for handling matrices and storing arrays. The available B-spline and LAPACK libraries were the two basic foundations of the general structure of the programs developed.

The first part of this thesis deals with the general Hartree-Fock-Bogoliubov formalism. A detailed description of the Hartree-Fock-Bogoliubov equations is given in Chapter II. The HFB equations in coordinate space representation are derived and presented in the form of axially symmetric objects. The Skyrme interaction is reviewed in Chapter III. We limit this work to the  $SkM^*$  and  $SLy4$  Skyrme-type forces, according to the parameters shown in this chapter.

The numerical technique details are presented. The derivation of the formalism gives us two-dimensional matrices that later will be implemented on the lattice. High accuracy is achieved with the implementation of the differential equations using the B-Spline representation (Chapter IV), which is very convenient for programming. In Chapter V a review of the numerical process in actual Nuclear Physics calculations is given. The initialization is

made with the help of Hartree-Fock + BCS/Lipkin-Nogami theory and the Woods-Saxon potential generation of wavefunctions. The iterative process under the HFB formalism is explained in this Chapter.

The results and conclusions are presented in the last part. Calculations of  $^{22}\text{O}$  are shown in Chapter VI. A study of the four-spinor wavefunctions is performed based on  $^{150}\text{Sn}$  calculations. Finally, the determination for the Sulfur two-neutron dripline is done by means of a series of calculations of two-neutron separation energies in the sulfur isotope chain. The summary and main conclusions of this thesis are presented in Chapter VII.

## CHAPTER II

### HARTREE-FOCK-BOGOLIUBOV THEORY

It has been shown that self-consistent mean-field models based on effective interactions are successful in describing nuclear properties. These models describe independent particles moving in an average potential, derived from the sum of two-body interactions only [22, 23, 24]. With unfilled shells, we find additional correlations -pairing correlations- between these particles. A key ingredient in mean-field models is the treatment of such correlations. For nuclei close to stability, the pairing correlations are usually incorporated with the help of the BCS approximation [25]. However, the BCS approach becomes unreliable for nuclei close to the drip lines because the coupling between the bound and single-particle states is not properly treated [5, 6, 26]. This kind of simple treatment of the pairing correlations leads to a non-negligible probability of finding particles outside the nucleus, forming a non-physical nucleon gas.

The standard Hartree-Fock theory (HF) is the precursor to the Hartree-Fock-Bogoliubov (HFB) formalism. The former, based on the single-particle picture, does not incorporate the pairing correlations. This does not have a great impact when dealing with nuclei close to stability. However, the pairing effects are stronger for nuclei near the driplines and they must be incorporated. The latter includes pairing correlations self-consistently, allowing HFB to correctly treat the pairing effect.

In order to have a good understanding of the HFB theory, it is useful to go over a brief summary of the most general Hartree-Fock theory and of the BCS theory of pairing. With that goal in mind, the first section of this chapter is focused in these two topics. Also, in this chapter it will be shown that in the limit of the stability –and no pairing effects– the HFB formalism agrees with the results of the HF theory.

In the following sections, the standard HF and HFB formalisms are reviewed in energy representation. This information has been extracted mainly from Refs. [22, 23, 24], which specialize in many-body theory applied to nuclear systems.

## 2.1 Hartree-Fock + BCS

This mean field theory provides a solution to the nuclear many-body problem, based on a Hamiltonian containing a suitable two-body interaction. In second quantization, this is given by

$$\hat{H} = \sum_{ij} t_{ij} \hat{c}_i^\dagger \hat{c}_j + \frac{1}{2} \sum_{ijkl} \bar{v}_{i,j,k,l} \hat{c}_i^\dagger \hat{c}_j^\dagger \hat{c}_l \hat{c}_k \quad , \quad (1)$$

where  $t$  is the one-body operator (e.g., the kinetic energy) and  $\bar{v}_{i,j,k,l} = \langle i, j | v | k, l \rangle - \langle i, j | v | l, k \rangle$  represents the antisymmetric two-body interaction matrix elements, with single-particle creation and annihilation operators  $\hat{a}_i^\dagger, \hat{a}_i$ .

In Hartree-Fock theory, a single Slater determinant is selected to be the many-body wavefunction

$$|\Psi^{HF}\rangle = \prod_{i=1}^A \hat{c}_i^\dagger |0\rangle \quad , \quad (2)$$

where the index over the product corresponds to a set of single particle states with orthonormal wavefunctions  $\phi_i(r), i = 1, \dots, A$ . These are eigenfunctions of the single particle Hamiltonian  $h$ ,

$$h(x)\phi_i(x) = \mathcal{E}_i\phi_i(x) \quad , i = \mathbf{r}, s, t \quad (3)$$

where the single-particle wavefunctions,  $\phi_i(x)$ , are represented in coordinate space and  $\mathcal{E}_i$  are the corresponding single-particle energies. The approximate ground state function is determined from the variational principle applied to the Hamiltonian with the normalization condition

$$\delta \langle \Psi^{HF} | \hat{H} - E | \Psi^{HF} \rangle = 0 \quad , \quad (4)$$

where the average single-particle Hartree-Fock potential is

$$\hat{H}^{HF} = \sum_{i=1}^A \hat{h}(i) \quad . \quad (5)$$

The single-particle density associated with the state  $|\Psi^{HF}\rangle$  is defined as

$$\rho_{ij} = \langle i | \rho | j \rangle = \langle \Psi^{HF} | \hat{a}_i^\dagger \hat{a}_j | \Psi^{HF} \rangle \quad (6)$$

It is more convenient to represent the ground state wavefunction (2) in terms of the density matrix, since it is diagonal in the basis  $\hat{a}_i^\dagger, \hat{a}_j$ .

The variation of the energy functional (4) with respect to the single particle wavefunctions  $\phi_i$  leads to a set of coupled, non-linear equations

$$h_{kl} = t_{kl} + \sum_{i=1}^A \bar{v}_{kili} = \mathcal{E}_k \delta_{kl} \quad (7)$$

The *Hartree-Fock equations* in coordinate space are written

$$\begin{aligned} \mathcal{E}_k \phi_k(\mathbf{r}, \sigma) = & -\frac{\hbar^2}{2m} \nabla^2 \phi_k(\mathbf{r}, \sigma) + \left( \int d^3r' v(\mathbf{r}, \mathbf{r}') \sum_{j=1}^A |\phi_j(\mathbf{r}')|^2 \right) \phi_k(\mathbf{r}, \sigma) \\ & - \sum_{j=1}^A \phi_j(\mathbf{r}, \sigma) \int d^3r' \sum_{\sigma'} v(\mathbf{r}, \sigma, \mathbf{r}', \sigma') \phi_j^*(\mathbf{r}', \sigma) \phi_k(\mathbf{r}', \sigma') \end{aligned} \quad (8)$$

In this integro-differential equation, the integral in brackets on the second term is the *mean field*, and the third term is called the *exchange (Fock) term*. The Hartree-Fock equations present a *self-consistent* problem, since the mean field and the exchange terms depend on the single-particle wavefunctions of the solution of the single-particle eigenvalue problem. It is usually solved by iteration methods, as it will be shown for the HFB case.

Finally, in terms of the density matrix, the variational equation (4) can also be written

$$[h, \rho] = 0 \quad (9)$$

This is the density matrix formulation of the Hartree-Fock equations.

### 2.1.1 BCS Equations

The Bardeen-Cooper-Schrieffer theory (BCS) was first developed in condensed-matter physics to explain the superconductivity phenomena [25]. It was introduced to Nuclear Physics by Belyaev [27] as a way to account for the pairing correlations in nuclei. The BCS theory states basically that the pairing strength is constant for the matrix elements corresponding to the pairing tensor. A many-body Hamiltonian containing single-particle part plus a residual interaction represented by the pairing correlations is

$$\hat{H} = \sum_k \mathcal{E}_k \hat{c}_k^\dagger \hat{c}_k + \sum_{kk'>0} v_{k,-k,k',-k'} \hat{c}_k^\dagger \hat{c}_{-k}^\dagger \hat{c}_{-k'} \hat{c}_{k'} \quad , \quad q = n, p \quad . \quad (10)$$

with the pairing potential matrix elements

$$v_{k,-k,k',-k'} = \langle k, -k | v | k', -k' \rangle = -G_q = - \left( g_0 \mp g_1 \frac{N-Z}{A} \right) A^{-1} \text{ MeV} \quad . \quad (11)$$

The notation  $(k, k')$  denotes the angular momentum projection pairs. These are mutually time-reversed conjugated states coupled by the pairing force. The values of  $G_q$  have been fitted to numerous nuclei, and they depend on the mass range [28]. Given that the pairing strength is somehow set or chosen, it is used to evaluate the BCS equations.

An approximate solution for Eq. (10), based on the BCS state, is given by

$$|BCS\rangle = \prod_{k>0}^{\infty} (u_k + v_k \hat{a}_k^\dagger \hat{a}_{-k}^\dagger) |0\rangle , \quad (12)$$

where  $v_k$  gives the probability that the pair  $(k, -k)$  is occupied. The normalization of the BCS state gives the condition for the coefficients  $u_k, v_k$

$$u_k^2 + v_k^2 = 1 . \quad (13)$$

The particle number in BCS theory is not conserved; the best it can be done is to conserve it on average, i.e.

$$\langle BCS | \hat{N} | BCS \rangle \stackrel{!}{=} \sum_{k>0} 2v_k^2 = N \quad (14)$$

This restriction can be reached by adding a constraint to the Hamiltonian and introducing the Lagrange parameter  $\lambda$ . As in HF, the variational principal is applied to

$$\delta \langle BCS | \hat{H} - \lambda \hat{N} | BCS \rangle = 0 . \quad (15)$$

This yields the equation for the occupation probabilities,

$$v_k^2 = \frac{1}{2} \left( 1 - \frac{\chi_k}{\sqrt{\chi_k^2 + \Delta^2}} \right) , \quad (16)$$

with the pairing energy level

$$\chi_k = \mathcal{E}_k - \lambda - Gv_k^2 , \quad (17)$$

where  $\lambda$  is the Fermi level introduced above. The pairing gap ( $\Delta$ ) is given by

$$\Delta = G \sum_{k>0} u_k v_k . \quad (18)$$

Finally, making use of the above equations the *gap equation* is found to be,

$$\Delta = \frac{G}{2} \sum_{k>0} \frac{\Delta}{\sqrt{\chi_k^2 + \Delta^2}} . \quad (19)$$

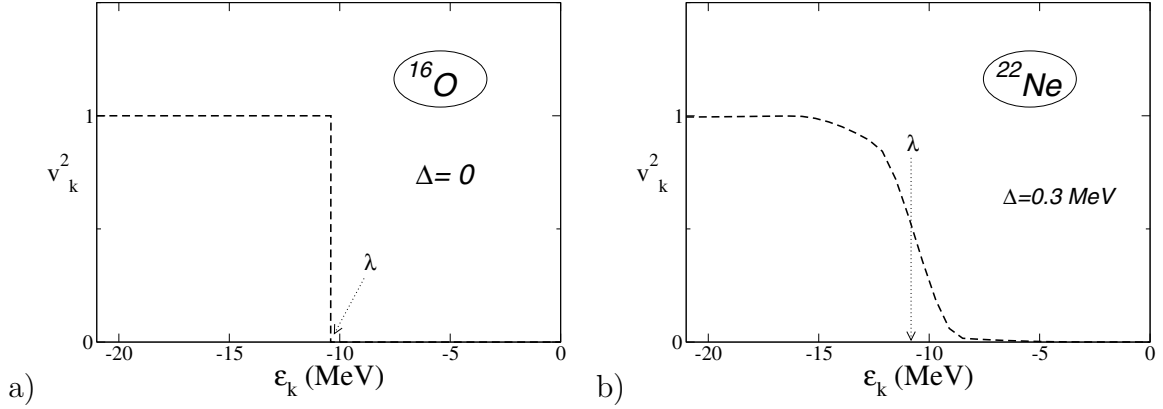


Figure 5: Occupation probabilities over the single-particle states generated by HF+BCS for: a) the trivial case where  $\Delta = 0$ . It looks like a step function; b) non-zero  $\Delta$ , it shows a smoother transition to non-occupied states.

In the  $v_k^2$  vs.  $\mathcal{E}_k$  energy distribution (see Fig. 5), the energy gap,  $\Delta$ , is a measure of the width of the transition between highly occupied states and unoccupied ones. The Fermi level,  $\lambda$ , is the energy at which  $v^2 = 1/2$ .

As mentioned before, the BCS equations give a description of the single-particle spectrum when using a constant pairing interaction. It has been shown that this approach works well when performing calculations for stable nuclei. For nuclei away from stability and close to the drip lines it reaches convergence problems. However, it gives a far better approximation than, say, generating the initial wavefunctions from a heuristic ad-hoc potential like the Woods-Saxon potential.

## 2.2 Standard HFB Formalism

In the HFB approximation the Hamiltonian is essentially reduced to two potentials: the self-consistent average potential  $\Gamma$  from Hartree-Fock theory, and an additional pairing field  $\Delta$ , known from the BCS theory. This section introduces the general quasiparticle picture in the standard HFB formalism and its application to axially symmetric systems.

The basic idea in the most general quasiparticle concept is to define the HFB approximate



ground state of the many-body system as a vacuum with respect to quasiparticles [29, 30]

$$\hat{\beta}_k |\Phi_0\rangle = 0 . \quad (20)$$

Handling the definition of quasi-particles in terms of exact eigenstates of the many-body Hamiltonian is rather difficult. Instead, we use the resulting quasiparticles from the Bogoliubov transformation [31, 32], which are now an approximation of the exact eigenfunctions of the Hamiltonian.

The many-body Hamiltonian in occupation number representation has the form [22]

$$\hat{H} = \sum_{i,j} t_{ij} \hat{c}_i^\dagger \hat{c}_j + \frac{1}{4} \sum_{i,j,m,n} \bar{v}_{ijmn}^{(2)} \hat{c}_i^\dagger \hat{c}_j^\dagger \hat{c}_n \hat{c}_m , \quad (21)$$

with the first term corresponding to the kinetic energy.  $\bar{v}_{ijmn}^{(2)}$  is the antisymmetrized two-body interaction, with single-particle operators  $\hat{c}, \hat{c}^\dagger$ . The BCS quasiparticle formulation can be obtained from the general linear transformation from particle operators  $\hat{c}, \hat{c}^\dagger$  to quasiparticle operators  $\hat{\beta}, \hat{\beta}^\dagger$ . Such a transformation takes the form [22]:

$$\begin{pmatrix} \hat{\beta} \\ \hat{\beta}^\dagger \end{pmatrix} = \begin{pmatrix} U^\dagger & V^\dagger \\ V^T & U^T \end{pmatrix} \begin{pmatrix} \hat{c} \\ \hat{c}^\dagger \end{pmatrix} . \quad (22)$$

Coefficients U and V are not arbitrary, since  $\beta$  and  $\beta^\dagger$  are to be chosen so they meet anti-commutation relations. However, U and V do not define uniquely the HFB wave function  $|\Phi_0\rangle$ .

Based on this transformation, the Hamiltonian (23) is then constructed in terms of quasiparticle operators  $\beta, \beta^\dagger$ :

$$\begin{aligned} \hat{H} - \lambda \hat{N} &= \hat{H}_0 + \sum_{i,j} \hat{H}_{ij} \beta_i^\dagger \beta_j + \sum_{i<j} (\hat{H}_{ij} \beta_i^\dagger \beta_j^\dagger + h.c.) + \hat{H}_{int} \\ &= \hat{H}_0 + \hat{H}_{11} + \hat{H}_{20} + \hat{H}_{40} + \hat{H}_{31} + \hat{H}_{22} , \end{aligned} \quad (23)$$

The particle number is no longer conserved, so the particle number operator  $\hat{N} = \sum_i \hat{c}_i^\dagger c_i$  is included as a constraint with a corresponding Lagrangian multiplier,  $\lambda$ . Eq. (23) represents the decomposition of the resulting Hamiltonian according to the number of quasiparticle operators. The indices in the Hamiltonian terms stand for the number of quasiparticle creation and annihilation operators they include, respectively. The *c-number*  $\hat{H}_0$ , is the

quasiparticle vacuum expectation value. The terms with four operators are neglected. The quasiparticle transformation is chosen such that  $\hat{H}_{20} = 0$  and  $\hat{H}_{11}$  is diagonal (see Ref.[22]).

To simplify the Hamiltonian (23), let's use *mean field* and *pairing field* definitions

$$\begin{aligned}\Gamma_{kl} &= \sum_{i,j} \bar{v}_{kjl} \rho_{ij} \\ \Delta_{kl} &= \frac{1}{2} \sum_{i,j} \bar{v}_{klj} \kappa_{ij} .\end{aligned}$$

These definitions include the basic building blocks of the theory, namely, the density matrix

$$\rho_{ij} = \langle \Phi_0 | \hat{c}_j^\dagger \hat{c}_i | \Phi_0 \rangle = (V^* V^T)_{ij} \quad (24)$$

and the pairing tensor

$$\kappa_{ij} = \langle \Phi_0 | \hat{c}_j \hat{c}_i | \Phi_0 \rangle = (V^* U^T)_{ij} \quad (25)$$

The densities  $\rho_{ij}$  and  $\kappa_{ij}$  do define uniquely the wave function  $|\Phi_0\rangle$ . Now we can write the Hamiltonian and the particle number constraint in terms of quasiparticle operators as

$$\hat{H} - \lambda \hat{N} = \sum_{i,j} \left( (t_{ij} + \frac{1}{2} \Gamma_{i,j} - \lambda) \rho_{ji} + \frac{1}{2} \Delta_{ij} \kappa_{ji}^* \right) + \sum_i E_i \hat{\beta}_i^\dagger \hat{\beta}_i + \hat{H}_{int} \quad (26)$$

The first sum corresponds to  $\hat{H}_0$ , the quasiparticle vacuum expectation value. The second term comes from  $\langle k | \hat{H}_{11} | l \rangle = E_k \delta_{kl}$  and includes the quasiparticle energy  $E_k$  (to be determined from HFB diagonalization). Finally,  $\hat{H}_{int}$  includes the neglected terms from the quasiparticle interactions.

Now, in quasiparticle representation, the HFB ground state energy including the constraint on the particle number  $N$  is given by

$$E(\mathcal{R}) = \langle \Phi_0 | \hat{H} - \lambda \hat{N} | \Phi_0 \rangle . \quad (27)$$

We now introduce the *generalized density matrix*

$$\mathcal{R} = \begin{pmatrix} \rho & \kappa \\ -\kappa^* & 1 - \rho^* \end{pmatrix} . \quad (28)$$

The hermitian  $\mathcal{R}$  matrix meets the condition  $\mathcal{R}^2 = \mathcal{R}$  for the HFB ground state (quasiparticle vacuum). In analogy with the HF case (where  $E = E(\rho)$ ), the equations of motion are derived from applying the variational principle with respect to the solution  $|\Phi_0\rangle$  to

$$\delta [E(\mathcal{R}) - \text{tr} \Lambda (\mathcal{R}^2 - \mathcal{R})] = 0 , \quad (29)$$

which results in the standard HFB equations (compare with Eq. (9))

$$[\mathcal{H}, \mathcal{R}] = 0 \quad , \quad (30)$$

with the generalized single-particle Hamiltonian

$$\mathcal{H} = \begin{pmatrix} (h - \lambda) & \Delta \\ -\Delta^* & -(h - \lambda)^* \end{pmatrix} , \quad (31)$$

where  $h = t + \Gamma$  is the *mean field Hamiltonian*, and  $\Delta$  denote the pairing potential. Later on, the Lagrange multiplier  $\lambda$  will turn out to be the Fermi energy of the system.

In the case where there is no pairing (e.g.  $\Delta = 0, \kappa = 0$ ), the Hartree-Fock Bogoliubov Eq.(30) is reduced to the expression that we get for the Hartree-Fock theory, Eq.(9). In this sense, the original HF theory with no pairing is a special case -a trivial one- of the more general HFB theory.

Equation (30) shows that there exist simultaneous eigenstates for Hamiltonian matrix in Eq. (31) and the density super-matrix  $\mathcal{R}$ . In terms of the transformation coefficients  $U, V$  we get

$$\begin{pmatrix} (h - \lambda) & \Delta \\ -\Delta^* & -(h - \lambda)^* \end{pmatrix} \begin{pmatrix} U_\alpha \\ V_\alpha \end{pmatrix} = +E_\alpha \begin{pmatrix} U_\alpha \\ V_\alpha \end{pmatrix} . \quad (32)$$

### 2.2.1 Quasiparticle wave functions in coordinate space

In practice, it is convenient to transform the standard HFB equations into a coordinate-space representation and solve the resulting differential equations on a lattice. We can then use the Skyrme forces (see Chapter III) to conveniently simplify further the HFB equations. First, we have to find the coordinate representation for a generalized mean field nuclear potential. For this purpose, we define two types of quasiparticle wave functions  $\phi_1$  and  $\phi_2$  [5],

$$\begin{aligned} \phi_1^*(E_\alpha, \mathbf{r}\sigma q) &= \sum_i U_{i\alpha} (2\sigma) \phi_i(\mathbf{r} - \sigma q), \\ \phi_2(E_\alpha, \mathbf{r}\sigma q) &= \sum_i V_{i\alpha}^* \phi_i(\mathbf{r}\sigma q) , \end{aligned} \quad (33)$$

where  $\hat{T}\phi_i(\mathbf{r}\sigma q) = -(2\sigma)\phi_i^*(\mathbf{r} - \sigma q)$  denotes the time-reversed state. These are the upper and lower components of the two-component single-quasiparticle HFB wave function. The basis

wave functions  $\phi_i$  in Eqs. (33) depend on the coordinate vector  $\mathbf{r}$ , the spin projection  $\sigma = \pm\frac{1}{2}$  and the isospin projection  $q$  ( $q = +\frac{1}{2}$  corresponds to protons and  $q = -\frac{1}{2}$  to neutrons).

The particle density matrix for the HFB ground state defined in terms of field operators  $\Psi^\dagger, \Psi$ , assumes a very simple mathematical structure in terms of  $\phi_1$  and  $\phi_2$  [6] :

$$\begin{aligned}
\rho(\mathbf{r}\sigma q, \mathbf{r}'\sigma'q') &= \langle \Phi_0 | \hat{\psi}^\dagger(\mathbf{r}'\sigma'q') \hat{\psi}(\mathbf{r}\sigma q) | \Phi_0 \rangle \\
&= \sum_{i,j} \rho_{ij} \phi_i(\mathbf{r}\sigma q) \phi_j^*(\mathbf{r}'\sigma'q') \\
&= \sum_{E_\alpha > 0}^{\infty} \phi_2(E_\alpha, \mathbf{r}\sigma q) \phi_2^*(E_\alpha, \mathbf{r}'\sigma'q') .
\end{aligned} \tag{34}$$

The sum over the states  $E_\alpha$  has replaced the integral form of the equations, since the HFB continuous spectrum has been discretized for practical calculations (see Ch. V).

Instead of the standard antisymmetric pairing tensor  $\kappa$  (Eq. 25) defined as

$$\kappa(\mathbf{r}\sigma q, \mathbf{r}'\sigma'q') = \langle \Phi_0 | \hat{\psi}(\mathbf{r}'\sigma'q') \hat{\psi}(\mathbf{r}\sigma q) | \Phi_0 \rangle \tag{35}$$

we introduce the pairing density matrix  $\tilde{\rho}$  which is Hermitian for a time-reversal invariant ground state and hence more convenient to use [6] :

$$\begin{aligned}
\tilde{\rho}(\mathbf{r}\sigma q, \mathbf{r}'\sigma'q') &= (-2\sigma') \kappa(\mathbf{r}\sigma q, \mathbf{r}' - \sigma'q') \\
&= (-2\sigma') \sum_{i,j} \kappa_{ij} \phi_i(\mathbf{r}\sigma q) \phi_j(\mathbf{r}' - \sigma'q') \\
&= - \sum_{E_\alpha > 0}^{\infty} \phi_2(E_\alpha, \mathbf{r}\sigma q) \phi_1^*(E_\alpha, \mathbf{r}'\sigma'q') .
\end{aligned} \tag{36}$$

In principle, the sums go over all the positive energy states, but in practice a cutoff in the number of states is done up to a reasonable number ( $\sim 60$  MeV). See Section 6.1 on Chapter V for the guideline on how to set the Energy Cutoff.

Proceeding in analogy to the pairing density matrix, we replace the antisymmetric pairing potential  $\Delta$  in Eq. (31) with the Hermitian pairing field  $\tilde{h}$

$$\tilde{h}(\mathbf{r}\sigma q, \mathbf{r}'\sigma'q') = (-2\sigma') \Delta(\mathbf{r}\sigma q, \mathbf{r}' - \sigma'q') . \tag{37}$$

## Normal density and pairing density

From expressions (34), and (36) for the density matrices we obtain the following expressions for the normal density  $\rho_q(\mathbf{r})$  and pairing density  $\tilde{\rho}_q(\mathbf{r})$  which are defined as the spin-averaged diagonal elements of their correspondent matrices

$$\begin{aligned}\rho_q(\mathbf{r}) &= \sum_{\sigma} \rho(\mathbf{r}\sigma q, \mathbf{r}\sigma q) \\ &= \sum_{\sigma} \sum_{\alpha} \phi_{2,\alpha}(\mathbf{r}\sigma q) \phi_{2,\alpha}^*(\mathbf{r}\sigma q) ,\end{aligned}\tag{38}$$

$$\begin{aligned}\tilde{\rho}_q(\mathbf{r}) &= \sum_{\sigma} \tilde{\rho}(\mathbf{r}\sigma q, \mathbf{r}\sigma q) \\ &= - \sum_{\sigma} \sum_{\alpha} \phi_{2,\alpha}(\mathbf{r}\sigma q) \phi_{1,\alpha}^*(\mathbf{r}\sigma q) .\end{aligned}\tag{39}$$

The quasiparticle energy  $E_{\alpha}$  is denoted by index  $\alpha$  for simplicity. The physical interpretation of  $\tilde{\rho}_q$  has been discussed in [6]: the quantity  $[\tilde{\rho}_q(\mathbf{r}) \Delta V/2]^2$  gives the probability to find a correlated pair of nucleons with opposite spin projection in the volume element  $\Delta V$  (see Fig. 3).

### 2.2.2 Kinetic and spin-orbit densities

The kinetic energy density  $\tau_q(\mathbf{r})$  is defined as a functional of the upper components  $\phi_2$

$$\begin{aligned}\tau_q(\mathbf{r}) &= \nabla \cdot \nabla' \rho_q(\mathbf{r}, \mathbf{r}')|_{\mathbf{r}=\mathbf{r}'} \\ &= \nabla \cdot \nabla' \left( \sum_{\sigma} \rho(\mathbf{r}\sigma q, \mathbf{r}'\sigma q) \right) |_{\mathbf{r}=\mathbf{r}'} \\ &= \sum_{\sigma} \sum_{\alpha} |\nabla \phi_{2,\alpha}(\mathbf{r}\sigma q)|^2 .\end{aligned}\tag{40}$$

The spin-orbit density does not appear directly in the nuclear potential, but rather its divergence (see Chapter III)

$$\nabla \cdot \mathbf{J}_q(\mathbf{r}) = -i \sum_{\alpha} (\nabla \phi_{2,\alpha}^{\dagger}(\mathbf{r}, q)) \cdot (\nabla \times \sigma) \phi_{2,\alpha}(\mathbf{r}, q) .\tag{41}$$

### 2.2.3 Energy functional and mean fields

Standard HFB theory yields the following expression for the total binding energy of the nucleus in its ground state, with contributions from the mean field and the pairing field

$$E_{HFB} = \langle \Phi_{HFB} | \hat{H} | \Phi_{HFB} \rangle = E_{mf} + E_{pair}\tag{42}$$

To simplify the notation, we drop the isospin indices  $q, q'$  in this section and in the following section. In coordinate space, the mean field contribution is given by [6]

$$E_{mf} = \frac{1}{2} \int d^3r \int d^3r' \sum_{\sigma, \sigma'} [ t(\mathbf{r}\sigma, \mathbf{r}'\sigma') + h(\mathbf{r}\sigma, \mathbf{r}'\sigma') ] \rho(\mathbf{r}'\sigma', \mathbf{r}\sigma) , \quad (43)$$

and pairing energy contribution has the form

$$E_{pair} = \frac{1}{2} \int d^3r \int d^3r' \sum_{\sigma, \sigma'} \tilde{h}(\mathbf{r}\sigma, \mathbf{r}'\sigma') \tilde{\rho}(\mathbf{r}'\sigma', \mathbf{r}\sigma) . \quad (44)$$

The quantity  $h$  denotes the mean field Hamiltonian, i.e. the particle-hole (p-h) channel of the interaction

$$h(\mathbf{r}\sigma, \mathbf{r}'\sigma') = t(\mathbf{r}\sigma, \mathbf{r}'\sigma') + \Gamma(\mathbf{r}\sigma, \mathbf{r}'\sigma') \quad (45)$$

with

$$\Gamma(\mathbf{r}\sigma, \mathbf{r}'\sigma') = \int d^3r_2 \int d^3r'_2 \sum_{\sigma_2, \sigma'_2} \bar{v}_{12}^{(2)}(\mathbf{r}\sigma, \mathbf{r}_2\sigma_2; \mathbf{r}'\sigma', \mathbf{r}_2'\sigma'_2) \rho(\mathbf{r}_2'\sigma'_2, \mathbf{r}_2\sigma_2) \quad (46)$$

where  $\bar{v}_{12}^{(2)}$  is the antisymmetrized two-body effective N-N interaction (see Chapter III). The kinetic energy matrix elements are given by

$$t(\mathbf{r}\sigma, \mathbf{r}'\sigma') = \delta(\mathbf{r} - \mathbf{r}') \delta_{\sigma, \sigma'} \left( -\frac{\hbar^2}{2m} \nabla^2 \right) \quad (47)$$

In a similar way, we find for the pairing mean field  $\tilde{h}$ , i.e. for the p-p and h-h channels of the interaction

$$\tilde{h}(\mathbf{r}\sigma, \mathbf{r}'\sigma') = \int d^3r'_1 \int d^3r'_2 \sum_{\sigma'_1, \sigma'_2} 2\sigma'_1\sigma'_2 \bar{v}_{pair}^{(2)}(\mathbf{r}\sigma, \mathbf{r}' - \sigma'; \mathbf{r}'_1\sigma'_1, \mathbf{r}'_2 - \sigma'_2) \tilde{\rho}(\mathbf{r}'_1\sigma'_1, \mathbf{r}'_2\sigma'_2) . \quad (48)$$

#### 2.2.4 Pairing interaction.

In practice, one tends to use effective N-N interactions for the p-h and for the p-p channel. If one assumes that the effective pairing interaction  $\bar{v}_{pair}^{(2)}$  is local

$$\bar{v}_{pair}^{(2)}(\mathbf{r}\sigma, \mathbf{r}' - \sigma'; \mathbf{r}'_1\sigma'_1, \mathbf{r}'_2 - \sigma'_2) = \delta(\mathbf{r}'_1 - \mathbf{r}) \delta_{\sigma'_1, \sigma} \delta(\mathbf{r}'_2 - \mathbf{r}') \delta_{\sigma'_2, \sigma'} V_p(\mathbf{r}\sigma, \mathbf{r}' - \sigma') , \quad (49)$$

the pairing mean field Hamiltonian becomes

$$\tilde{h}(\mathbf{r}\sigma, \mathbf{r}'\sigma') = V_p(\mathbf{r}\sigma, \mathbf{r}' - \sigma') \tilde{\rho}(\mathbf{r}\sigma, \mathbf{r}'\sigma') . \quad (50)$$

For the pairing interaction  $V_p$  we utilize the form

$$V_p(\mathbf{r}\sigma, \mathbf{r}' - \sigma') = V_0 \delta(\mathbf{r} - \mathbf{r}') \delta_{\sigma, \sigma'} F(\mathbf{r}) . \quad (51)$$

According to the prescription formulated in Refs. [33, 34], Dobaczewski et al. deduced a pairing strength of  $V_0 = -170 \text{ MeV fm}^3$ , with  $\mathcal{E}_{max} = 60 \text{ MeV}$  for the Skyrme SLy4 force with pure delta-pairing. The same parameters are utilized in all the 2-D calculations of this thesis. The pairing parameterization of Eq. (51) describes two primary pairing forces: a pure delta interaction ( $F = 1$ ) that gives rise to *volume pairing*, and a density dependent delta interaction (DDDI) that gives rise to *surface pairing*. In the latter case, one uses the following phenomenological ansatz [35] for the factor  $F$

$$F(\mathbf{r}) = 1 - \left( \frac{\rho(\mathbf{r})}{\rho_0} \right)^\gamma \quad (52)$$

where  $\rho(\mathbf{r})$  is the mass density, and  $\rho_0$  is the saturation density ( $0.16 \text{ fm}^{-3}$ ).

The DDDI interaction generates the following pairing mean field for the two isospin orientations  $q = \pm \frac{1}{2}$

$$\tilde{h}_q(\mathbf{r}\sigma, \mathbf{r}'\sigma') = \frac{1}{2} V_0^{(q)} \tilde{\rho}_q(\mathbf{r}) F(\mathbf{r}) \delta(\mathbf{r} - \mathbf{r}') \delta_{\sigma, \sigma'} . \quad (53)$$

The pairing contribution to the nuclear binding energy is then

$$\begin{aligned} E_{pair} &= E_{pair}^{(p)} + E_{pair}^{(n)} \\ &= \int d^3r \left[ \frac{V_0^{(p)}}{4} \tilde{\rho}_p^2(\mathbf{r}) + \frac{V_0^{(n)}}{4} \tilde{\rho}_n^2(\mathbf{r}) \right] F(\mathbf{r}) . \end{aligned}$$

An important related quantity is the average pairing gap for protons and neutrons which is defined as [5, 6]

$$\langle \Delta_q \rangle = -\frac{1}{N_q} \text{trace} (\tilde{h}_q \rho_q) = -\frac{1}{N_q} \int d^3r \int d^3r' \sum_{\sigma, \sigma'} \tilde{h}_q(\mathbf{r}\sigma, \mathbf{r}'\sigma') \rho_q(\mathbf{r}'\sigma', \mathbf{r}\sigma) \quad (54)$$

where  $N_q$  denotes the number of protons or neutrons. Inserting the expression derived earlier for the mean pairing field we arrive at

$$\langle \Delta_q \rangle = -\frac{1}{2} \frac{V_0^{(q)}}{N_q} \int d^3r \tilde{\rho}_q(\mathbf{r}) \rho_q(\mathbf{r}) F(\mathbf{r}) . \quad (55)$$

Note that the pairing gap is a positive quantity because  $V_0^{(q)} < 0$ .

### 2.2.5 HFB equations in coordinate space

Extensive HFB studies have been performed using density-dependent effective forces (i.e. Gogny [36, 37]) fitted to reproduce nuclear properties with relative success. The disadvantage of finite-range forces like the Gogny one is that it is impossible to take high-energy continuum states into account. For certain types of effective interactions like the Skyrme mean field (see Chapter III) and pairing delta-interactions, the particle Hamiltonian  $h$  and the pairing Hamiltonian  $\tilde{h}$  are diagonal in isospin space and local in position space. Now we make use of such a property to simplify our approach.

From inserting wavefunctions definitions, Eqs. (33), into matrix (32) we get the generalized HFB equations in coordinate space

$$\int d^3r' \sum_{\sigma'} \begin{pmatrix} h^q(\mathbf{r}\sigma, \mathbf{r}'\sigma') & \tilde{h}^q(\mathbf{r}\sigma, \mathbf{r}'\sigma') \\ \tilde{h}^q(\mathbf{r}\sigma, \mathbf{r}'\sigma') & -h^q(\mathbf{r}\sigma, \mathbf{r}'\sigma') \end{pmatrix} \begin{pmatrix} \phi_{1,\alpha}^q(\mathbf{r}'\sigma') \\ \phi_{2,\alpha}^q(\mathbf{r}'\sigma') \end{pmatrix} = \begin{pmatrix} E_\alpha + \lambda & 0 \\ 0 & E_\alpha - \lambda \end{pmatrix} \begin{pmatrix} \phi_{1,\alpha}^q(\mathbf{r}\sigma) \\ \phi_{2,\alpha}^q(\mathbf{r}\sigma) \end{pmatrix}. \quad (56)$$

Using the localized properties of the mean field Hamiltonian and pairing Hamiltonian of Eqs. (50) and (53), the mean fields become local. Inserting Hamiltonians  $h^q$  and  $\tilde{h}^q$  into the HFB equations (Eq. 56) results in a 4x4 structure in spin space:

$$\begin{pmatrix} (h^q - \lambda) & \tilde{h}^q \\ \tilde{h}^q & -(h^q - \lambda) \end{pmatrix} \begin{pmatrix} \phi_{1,\alpha}^q(\mathbf{r}) \\ \phi_{2,\alpha}^q(\mathbf{r}) \end{pmatrix} = E_\alpha^q \begin{pmatrix} \phi_{1,\alpha}^q(\mathbf{r}) \\ \phi_{2,\alpha}^q(\mathbf{r}) \end{pmatrix} \quad (57)$$

with

$$h^q = \begin{pmatrix} h_{\uparrow\uparrow}^q(\mathbf{r}) & h_{\uparrow\downarrow}^q(\mathbf{r}) \\ h_{\downarrow\uparrow}^q(\mathbf{r}) & h_{\downarrow\downarrow}^q(\mathbf{r}) \end{pmatrix}, \quad \tilde{h}^q = \begin{pmatrix} \tilde{h}_{\uparrow\uparrow}^q(\mathbf{r}) & \tilde{h}_{\uparrow\downarrow}^q(\mathbf{r}) \\ \tilde{h}_{\downarrow\uparrow}^q(\mathbf{r}) & \tilde{h}_{\downarrow\downarrow}^q(\mathbf{r}) \end{pmatrix}.$$

Because of the structural similarity between the Dirac equation and the HFB equation in coordinate space, we encounter here similar computational challenges: for example, the spectrum of quasiparticle energies  $E$  is unbounded from above and below. The spectrum is discrete for  $|E| < -\lambda$  and continuous for  $|E| > -\lambda$  (see Fig 6). For even-even nuclei it is customary to solve the HFB equations with a positive quasiparticle energy spectrum  $+E_\alpha$  and consider all negative energy states as occupied in the HFB ground state.



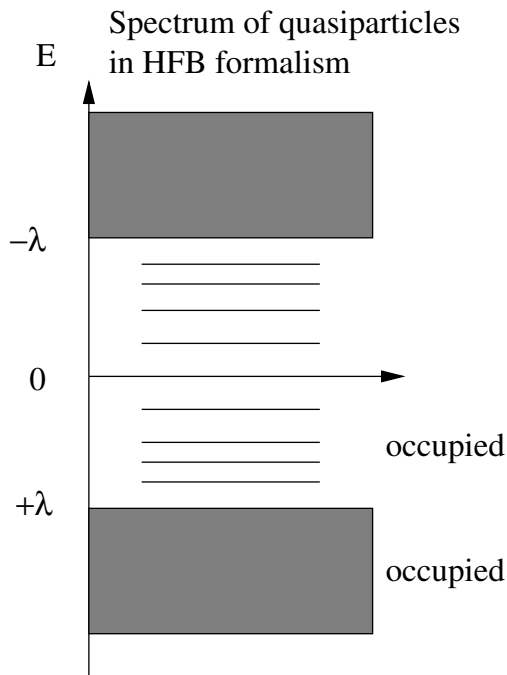


Figure 6: Quasiparticle energy spectrum. It is discrete for  $+\lambda < E < -\lambda$ . The negative energy states are occupied in the HFB ground state.

### 2.3 Two-dimensional Reduction for Axially Symmetric Systems

The main approximation in this work is the assumption that the nucleus is symmetric with respect to an intrinsic frame of reference, the  $z$ -axis. We assume that the HFB quasiparticle Hamiltonian is invariant under rotations  $\hat{R}_z$  around the  $z$ -axis,

$$[\mathcal{H}, \hat{R}_z] = 0 . \quad (58)$$

Due to the axial symmetry of the problem, it is advantageous to introduce cylindrical coordinates  $(\phi, r, z)$ , see Figure 7. The rotations around the  $z$ -axis are generated by the operator

$$\hat{R}_z(\phi) = \exp[-i\phi\hat{j}_z/\hbar] . \quad (59)$$

The requirement (58) is then equivalent to

$$[\mathcal{H}, \hat{j}_z] = 0 . \quad (60)$$

Because of the above condition, it is possible to construct simultaneous eigenfunctions of the generalized Hamiltonian  $\mathcal{H}$  and the  $z$ -component of the angular momentum,  $\hat{j}_z$

$$\mathcal{H} \psi_{n,\Omega,q}(\phi, r, z) = E_{n,\Omega,q} \psi_{n,\Omega,q}(\phi, r, z) \quad (61)$$

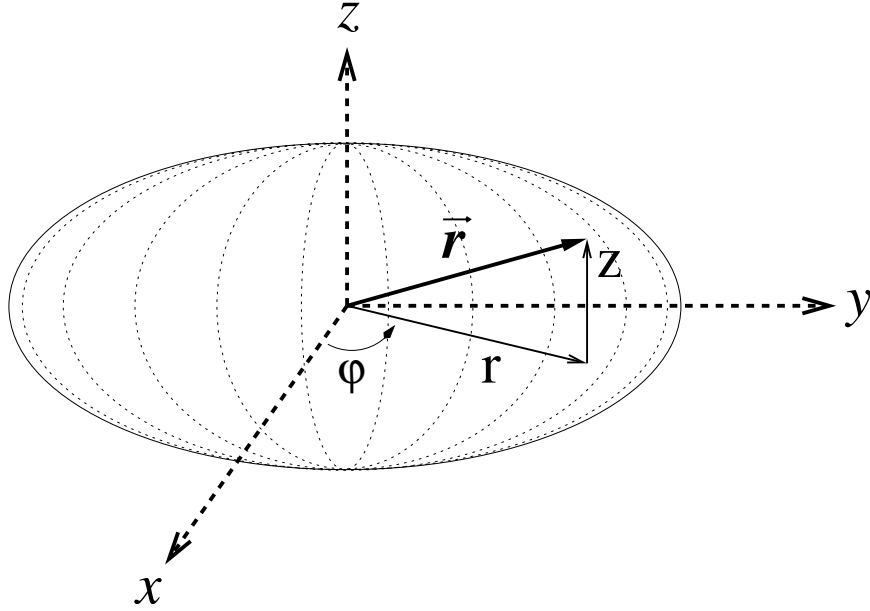


Figure 7: Cylindrical coordinates in the axial symmetry. For objects symmetric with respect to the  $z$ -axis the angular dependence disappears. Most nuclei ground states can be described using this symmetry.

$$\hat{j}_z \psi_{n,\Omega,q}(\phi, r, z) = \hbar\Omega \psi_{n,\Omega,q}(\phi, r, z) , \quad (62)$$

which implies that the 4-spinor wavefunction can be separated in angular and  $(r, z)$ -dependence parts. In the four-dimensional spinor space, the eigenvalue equation for  $\hat{j}_z$  is

$$\hbar \begin{pmatrix} -i\partial_\phi + \frac{1}{2} & 0 & 0 & 0 \\ 0 & -i\partial_\phi - \frac{1}{2} & 0 & 0 \\ 0 & 0 & -i\partial_\phi + \frac{1}{2} & 0 \\ 0 & 0 & 0 & -i\partial_\phi - \frac{1}{2} \end{pmatrix} \begin{pmatrix} \psi_{n,\Omega,q}^{(1)}(\phi, \uparrow) \\ \psi_{n,\Omega,q}^{(1)}(\phi, \downarrow) \\ \psi_{n,\Omega,q}^{(2)}(\phi, \uparrow) \\ \psi_{n,\Omega,q}^{(2)}(\phi, \downarrow) \end{pmatrix} = \hbar\Omega \begin{pmatrix} \psi_{n,\Omega,q}^{(1)}(\phi, \uparrow) \\ \psi_{n,\Omega,q}^{(1)}(\phi, \downarrow) \\ \psi_{n,\Omega,q}^{(2)}(\phi, \uparrow) \\ \psi_{n,\Omega,q}^{(2)}(\phi, \downarrow) \end{pmatrix} \quad (63)$$

The  $(r, z)$  part of the wavefunctions have been left out in this step since  $\hat{j}_z$  only operates on the angular part. This is equivalent to writing four independent equations

$$\left(-i \frac{\partial}{\partial \phi} + \frac{1}{2} - \Omega\right) \psi_{n,\Omega,q}^{(1)}(\phi, \uparrow) = 0 , \quad (64)$$

$$\left(-i \frac{\partial}{\partial \phi} - \frac{1}{2} + \Omega\right) \psi_{n,\Omega,q}^{(1)}(\phi, \downarrow) = 0 , \quad (65)$$

$$\left(-i \frac{\partial}{\partial \phi} + \frac{1}{2} - \Omega\right) \psi_{n,\Omega,q}^{(2)}(\phi, \uparrow) = 0, \quad (66)$$

$$\left(-i \frac{\partial}{\partial \phi} - \frac{1}{2} + \Omega\right) \psi_{n,\Omega,q}^{(2)}(\phi, \downarrow) = 0. \quad (67)$$

Solving each equation and after normalization, the angular part of the four-spinor wavefunction takes the form

$$\psi_{n,\Omega,q}(\phi) = \frac{1}{\sqrt{2\pi}} \begin{pmatrix} e^{i(\Omega-\frac{1}{2})\phi} \\ e^{i(\Omega+\frac{1}{2})\phi} \\ e^{i(\Omega-\frac{1}{2})\phi} \\ e^{i(\Omega+\frac{1}{2})\phi} \end{pmatrix}, \quad (68)$$

with the quantum numbers  $\Omega = \pm\frac{1}{2}, \pm\frac{3}{2}, \pm\frac{5}{2}, \dots$  corresponding to each  $n$ th energy state. The simultaneous  $\mathcal{H}, j_z$  quasiparticle eigenfunctions now take the form

$$\psi_{n,\Omega,q}(\phi, r, z) = \begin{pmatrix} \phi_{n,\Omega,q}^{(1)}(\phi, r, z) \\ \phi_{n,\Omega,q}^{(2)}(\phi, r, z) \end{pmatrix} = \frac{1}{\sqrt{2\pi}} \begin{pmatrix} e^{i(\Omega-\frac{1}{2})\phi} \phi_{n,\Omega,q}^{(1)}(r, z, \uparrow) \\ e^{i(\Omega+\frac{1}{2})\phi} \phi_{n,\Omega,q}^{(1)}(r, z, \downarrow) \\ e^{i(\Omega-\frac{1}{2})\phi} \phi_{n,\Omega,q}^{(2)}(r, z, \uparrow) \\ e^{i(\Omega+\frac{1}{2})\phi} \phi_{n,\Omega,q}^{(2)}(r, z, \downarrow) \end{pmatrix}. \quad (69)$$

We introduce the following useful notation to denote explicitly the spinors of the upper and lower components of the wavefunctions

$$\begin{aligned} U_{n\Omega q}^{(1,2)}(r, z) &= \phi_{n,\Omega,q}^{(1,2)}(r, z, \uparrow), \\ L_{n\Omega q}^{(1,2)}(r, z) &= \phi_{n,\Omega,q}^{(1,2)}(r, z, \downarrow). \end{aligned} \quad (70)$$

Since the angular dependence is determined exclusively by  $\Omega$ , we can define a Hamiltonian  $h$  that is uniquely defined by  $\Omega$ . Now, we get  $[h, j_z] = 0$  for each value of  $\Omega$ . Evaluating this commutator using the matrix form of  $j_z$  in Eq.(63), we can determine the  $\phi$ -dependence of the HFB quasiparticle Hamiltonian and arrive at the following structure for the Hamiltonian

$$h(\phi, r, z) = \begin{pmatrix} h'_{\uparrow\uparrow}(r, z) & e^{-i\phi} h'_{\uparrow\downarrow}(r, z) \\ e^{+i\phi} h'_{\downarrow\uparrow}(r, z) & h'_{\downarrow\downarrow}(r, z) \end{pmatrix}, \quad (71)$$

and the pairing Hamiltonian

$$\tilde{h}(\phi, r, z) = \begin{pmatrix} \tilde{h}'_{\uparrow\uparrow}(r, z) & e^{-i\phi} \tilde{h}'_{\uparrow\downarrow}(r, z) \\ e^{+i\phi} \tilde{h}'_{\downarrow\uparrow}(r, z) & \tilde{h}'_{\downarrow\downarrow}(r, z) \end{pmatrix}. \quad (72)$$

Inserting equations (71) and (72) into the eigenvalue Eq. (57), we arrive at the *reduced eigenvalue 2-D problem* [38] in cylindrical coordinates:

$$\begin{pmatrix} (h'_{\uparrow\uparrow} - \lambda) & h'_{\uparrow\downarrow} & \tilde{h}'_{\uparrow\uparrow} & \tilde{h}'_{\uparrow\downarrow} \\ h'_{\downarrow\uparrow} & (h'_{\downarrow\downarrow} - \lambda) & \tilde{h}'_{\downarrow\uparrow} & \tilde{h}'_{\downarrow\downarrow} \\ \tilde{h}'_{\uparrow\uparrow} & \tilde{h}'_{\uparrow\downarrow} & -(h'_{\uparrow\uparrow} - \lambda) & -h'_{\uparrow\downarrow} \\ \tilde{h}'_{\downarrow\uparrow} & \tilde{h}'_{\downarrow\downarrow} & -h'_{\downarrow\uparrow} & -(h'_{\downarrow\downarrow} - \lambda) \end{pmatrix} \begin{pmatrix} U_{n,\Omega,q}^{(1)} \\ L_{n,\Omega,q}^{(1)} \\ U_{n,\Omega,q}^{(2)} \\ L_{n,\Omega,q}^{(2)} \end{pmatrix} = E_{n,\Omega,q} \begin{pmatrix} U_{n,\Omega,q}^{(1)} \\ L_{n,\Omega,q}^{(1)} \\ U_{n,\Omega,q}^{(2)} \\ L_{n,\Omega,q}^{(2)} \end{pmatrix} \quad (73)$$

Here, quantities  $\tilde{h}'$ ,  $h'$ ,  $U$  and  $L$  are all functions of  $(r, z)$  only. Also,  $\tilde{h}'$  and  $h'$  contain the implicit isospin dependence  $q$ . The dependence on the azimuthal angle ( $\phi$ ) has vanished from the eigenvalue problem. This was expected since we are working in a geometry that describes objects symmetric respect to the  $z$ -axis. Eq. (73) is the main mathematical structure that we implement in computational calculations. For a given angular momentum projection quantum number  $\Omega$ , we solve the eigenvalue problem to obtain energy eigenvalues  $E_{n,\Omega,q}$  and eigenvectors  $\psi_{n,\Omega,q}$  for the corresponding HFB quasiparticle states.

Finally, we state the normalization condition for the four-spinor quasiparticle wavefunctions, Eq. (69)

$$\int d^3r \psi_{n\Omega q}^\dagger(\mathbf{r}) \psi_{n\Omega q}(\mathbf{r}) = 1, \quad (74)$$

which, using the notation established on Eqs. (70) for the four-spinor wavefunction, leads to

$$\int_0^\infty r dr \int_{-\infty}^\infty dz \left[ |U_{n\Omega q}^{(1)}(r, z)|^2 + |L_{n\Omega q}^{(1)}(r, z)|^2 + |U_{n\Omega q}^{(2)}(r, z)|^2 + |L_{n\Omega q}^{(2)}(r, z)|^2 \right] = 1. \quad (75)$$

### 2.3.1 Densities and currents

Making use of the definitions for the normal density and pairing density, Eqs. (38) and (39), we apply the bi-spinor structure of the quasiparticle wave functions to find the corresponding expressions in axial symmetry:

$$\rho_q(r, z) = \frac{1}{2\pi} \left( 2 \sum_{\Omega>0}^{\Omega_{max}} \right) \times \sum_{E_n>0}^{E_{max}} \left[ |U_{n\Omega q}^{(2)}(r, z)|^2 + |L_{n\Omega q}^{(2)}(r, z)|^2 \right] \quad (76)$$

$$\tilde{\rho}_q(r, z) = -\frac{1}{2\pi} \left( 2 \sum_{\Omega>0}^{\Omega_{max}} \right) \times \sum_{E_n>0}^{E_{max}} \left[ U_{n\Omega q}^{(2)}(r, z) U_{n\Omega q}^{(1)}(r, z) + L_{n\Omega q}^{(2)}(r, z) L_{n\Omega q}^{(1)}(r, z) \right] \quad (77)$$

Similarly, starting from definition (40) we obtain expression for the kinetic energy density

$$\begin{aligned} \tau_q(r, z) = \frac{1}{2\pi} \left( 2 \sum_{\Omega > 0}^{\Omega_{max}} \right) \sum_{E_n > 0}^{E_{max}} \left[ \frac{(\Omega - 1/2)^2}{r^2} |U_{n\Omega q}^{(2)}|^2 + \frac{(\Omega + 1/2)^2}{r^2} |L_{n\Omega q}^{(2)}|^2 \right. \\ \left. + \left| \frac{\partial U_{n\Omega q}^{(2)}}{\partial r} \right|^2 + \left| \frac{\partial L_{n\Omega q}^{(2)}}{\partial r} \right|^2 + \left| \frac{\partial U_{n\Omega q}^{(2)}}{\partial z} \right|^2 + \left| \frac{\partial L_{n\Omega q}^{(2)}}{\partial z} \right|^2 \right]. \end{aligned} \quad (78)$$

To get the divergence of the current, Eq.(41), the Pauli spin matrices must to be evaluated in cylindrical coordinates

$$\sigma = \mathbf{e}_r \sigma_r + \mathbf{e}_\phi \sigma_\phi + \mathbf{e}_z \sigma_z, \quad (79)$$

with the components

$$\sigma_r = \sigma \cdot \mathbf{e}_r = \cos \varphi \sigma_x + \sin \varphi \sigma_y = \begin{pmatrix} 0 & e^{-i\varphi} \\ e^{i\varphi} & 0 \end{pmatrix}, \quad (80)$$

$$\sigma_\phi = \sigma \cdot \mathbf{e}_\phi = -\sin \varphi \sigma_x + \cos \varphi \sigma_y = \begin{pmatrix} 0 & -ie^{-i\varphi} \\ ie^{i\varphi} & 0 \end{pmatrix} \quad (81)$$

and

$$\sigma_z = \begin{pmatrix} 1 & 0 \\ 0 & -1 \end{pmatrix}, \quad (82)$$

to explicitly get

$$\begin{aligned} \nabla \cdot \mathbf{J}_q(\mathbf{r}) &= \frac{1}{2\pi} \left( 2 \sum_{\Omega > 0}^{\Omega_{max}} \right) \sum_{E_n > 0}^{E_{max}} 2 \left[ \frac{\partial U_{n\Omega q}^{(2)}}{\partial r} \frac{\partial L_{n\Omega q}^{(2)}}{\partial z} - \frac{\partial L_{n\Omega q}^{(2)}}{\partial r} \frac{\partial U_{n\Omega q}^{(2)}}{\partial z} \right. \\ &+ \left. \frac{\Omega - 1/2}{r} U_{n\Omega q}^{(2)} \left( \frac{\partial U_{n\Omega q}^{(2)}}{\partial r} - \frac{\partial L_{n\Omega q}^{(2)}}{\partial z} \right) - \frac{\Omega + 1/2}{r} L_{n\Omega q}^{(2)} \left( \frac{\partial U_{n\Omega q}^{(2)}}{\partial z} + \frac{\partial L_{n\Omega q}^{(2)}}{\partial r} \right) \right]. \end{aligned}$$

A particularly important variable in the control of the calculations is the particle number. The total number of protons or neutrons is obtained by integrating over the corresponding particle density (Eq.76), as follows

$$\begin{aligned} N_q &= \int d^3r \rho_q(\mathbf{r}) \\ &= 2\pi \int_0^\infty r dr \int_{-\infty}^\infty dz \rho_q(r, z) \\ &= 2 \sum_{\Omega > 0}^{\Omega_{max}} \sum_{E_n > 0}^{E_{max}} \int_0^\infty r dr \int_{-\infty}^\infty dz \left[ |U_{n\Omega q}^{(2)}|^2 + |L_{n\Omega q}^{(2)}|^2 \right] \end{aligned}$$

The Hartree-Fock-Bogoliubov formalism is now complete for the axial symmetry. The wavefunctions can explicitly be expressed in this symmetry to construct the densities and, therefore, the HFB Hamiltonian. The detailed method of numerical calculations will be explained on Chapter V, based solely on the characteristics of the nucleus involved and on the input parameters defining the two-body interaction used.

## CHAPTER III

### HFB EQUATIONS USING THE SKYRME INTERACTION

The Skyrme interaction is one of the most widely used energy functionals for nuclear structure calculations. It was originally proposed in 1956 by T.H.R. Skyrme et al. [39], and fine tuned by D. Vautherin et al. and D.M. Brink et al. [40] in 1972. The functional involves the set of local densities and currents already described on Chapter II. One of the most important features of the Skyrme interaction is that its mathematical form -mainly the inclusion of  $\delta$  functions- simplifies calculations tremendously.

This chapter begins with the description of the general form of the Skyrme forces representing the fundamental two-body interaction. The values of the different parameterizations will be shown, and finally the energy functional and mean field under axial symmetry will be presented.

#### 3.1 Standard Skyrme interaction

The density-dependent two-body effective N-N interaction under the Skyrme force parameterization is given by [39, 41]

$$\begin{aligned}
 v_{12} &= t_0 (1 + x_0 \hat{P}_\sigma) \delta(\mathbf{r}_1 - \mathbf{r}_2) \\
 &+ \frac{1}{2} t_1 (1 + x_1 \hat{P}_\sigma) \{ \delta(\mathbf{r}_1 - \mathbf{r}_2) \hat{k}^2 + \hat{k}'^2 \delta(\mathbf{r}_1 - \mathbf{r}_2) \} \\
 &+ t_2 (1 + x_2 \hat{P}) \hat{\mathbf{k}}' \cdot \delta(\mathbf{r}_1 - \mathbf{r}_2) \hat{\mathbf{k}} + \frac{1}{6} t_3 (1 + x_3 \hat{P}_\sigma) \rho^\alpha \delta(\mathbf{r}_1 - \mathbf{r}_2) \\
 &+ i W_0 (\hat{\sigma}_1 + \hat{\sigma}_2) \cdot \{ \hat{\mathbf{k}}' \times \delta(\mathbf{r}_1 - \mathbf{r}_2) \hat{\mathbf{k}} \} ,
 \end{aligned} \tag{83}$$

$\hat{P}_\sigma$  being the spin-exchange operator, and  $\hat{\mathbf{k}}, \hat{\mathbf{k}}'$  relative momentum operators

$$\hat{\mathbf{k}} = \frac{1}{2i}(\nabla_1 - \nabla_2) , \quad \hat{\mathbf{k}}' = -\frac{1}{2i}(\nabla_1 - \nabla_2) . \tag{84}$$

The first term ( $t_0$ ) in Eq. (83) describes a pure  $\delta$ -force with a spin exchange; the second and third terms ( $t_1, t_2$ ) are the effective range parts; the term proportional to  $t_3$  represents the three-body force, originally proposed as

$$v_{123} = t_3 \delta(\mathbf{r}_1 - \mathbf{r}_2) \delta(\mathbf{r}_2 - \mathbf{r}_3) , \tag{85}$$

but for spin-saturated even-even nuclei this is equivalent to the density-dependent two-body interaction contained in Eq. (83). The fifth term ( $W_0$ ) in Eq. (83) represents a two-body spin orbit interaction.

Constants  $x_0, x_1, x_2, x_3, t_0, t_1, t_2, t_3, W_0$  and  $\alpha$  have been fitted to binding energies and radii of known nuclei all over the periodic table (see Table 1). Sometimes  $W_0$  is named  $t_4$  in the literature.

Table 1: Skyrme force parameters. Units for  $t_0$  through  $t_3$  and  $W_0$  are (MeV fm<sup>3</sup>), remaining terms are dimensionless.  $W_0$  values for SkI3,SkI4,SkP,SkO,SkO' are split into  $b_4, b'_4$  because of inclusion of new terms (see Table 2).  $\alpha$  and  $\hbar^2/2m$  are valid for old and new parameterizations.

Force	$t_0$	$t_1$	$t_2$	$t_3$	$x_0$	$x_1$
SkM* [42]	-2645.0	410.0	-135.0	15595.0	0.090	0.0
$Z_\sigma$ [43]	-1983.76	362.25	-104.27	11861.4	1.1717	0.0
SkT6 [44]	-1794.2	294.0	-294.0	12817.0	0.392	-0.5
SLy4 [45]	-2488.913	486.818	-546.395	13777.0	0.8340	-0.3438
SkI1 [46]	-1913.619	439.809	2697.594	10592.267	-0.954536	-5.782388
SkI3 [46]	-1762.88	561.608	-227.090	8106.2	0.3083	-1.1722
SkI4 [46]	-1855.827	473.829	1006.855	9703.607	0.405082	-2.889148
SkP [5]	-2931.70	320.618	-337.409	18708.96	0.29215	0.65318
SkO [47]	-2103.653	303.352	791.674	13553.252	-0.210701	-2.810752
SkO' [47]	-2099.419	301.531	154.781	13526.464	-0.029503	-1.325732
Force	$x_2$	$x_3$	$W_0$	$\alpha$	$\hbar^2/2m$	
SkM* [42]	0.0	0.0	130	1/6	20.73398	
$Z_\sigma$ [43]	0.0	1.7620	123.69	1/4	20.7525	
SkT6 [44]	-0.5	0.5	107	1/3	20.750	
SLy4 [45]	-1.0	1.3540	123	1/6	20.73553	
SkI1 [46]	-1.287379	-1.561421	124.26	1/4	20.7525	
SkI3 [46]	-1.0907	1.2926		1/4	20.7525	
SkI4 [46]	-1.325150	1.145203		1/4	20.7525	
SkP [5]	-0.53732	0.18103		1/6	20.73398	
SkO [47]	-1.461595	-0.429881		1/4	20.73553	
SkO' [47]	-2.323439	-0.147404		1/4	20.73553	

The form of the interaction in Eq. (83) with parameters  $x_0, x_1, x_2, x_3, t_0, t_1, t_2, t_3, t_4$ , has



been changed to an equivalent one with  $b_1, b'_1, b_2, b'_2, b_3, b'_3, b_4, b'_4$ , parameters [35]. This is done through the transformation

$$\begin{pmatrix} t_1 \\ t_1 x_1 \\ t_2 \\ t_2 x_2 \end{pmatrix} = \begin{pmatrix} \frac{4}{3} & \frac{8}{3} & -\frac{2}{3} & -\frac{4}{3} \\ -\frac{2}{3} & -\frac{4}{3} & \frac{4}{3} & \frac{8}{3} \\ 4 & -\frac{8}{3} & 2 & -\frac{4}{3} \\ -2 & \frac{4}{3} & -4 & \frac{8}{3} \end{pmatrix} \begin{pmatrix} b_1 \\ b_2 \\ b'_1 \\ b'_2 \end{pmatrix} \quad (86)$$

and

$$\begin{aligned} t_0 &= \frac{4}{3}b_0 - \frac{2}{3}b'_0 \\ t_0 x_0 &= -\frac{2}{3}b_0 + \frac{4}{3}b'_0 \\ t_3 &= \frac{16}{3}b_3 - \frac{8}{3}b'_3 \\ t_3 x_3 &= -\frac{8}{3}b_3 + \frac{16}{3}b'_3 \\ W_0 &= 2b_4 = 2b'_4 . \end{aligned} \quad (87)$$

The last equation only holds for certain forces. The “new parameterization” corresponding to the forces in Table 1 are shown in Table 2 in the next section. It can be observed in Table 2 that  $b_4$  and  $b'_4$  have different values in the case of forces like SkI and SkO. The next sections describe the energy density and the mean field under this “new parameterization”.

### 3.2 Energy density

In coordinate space, the calculation of the energy expectation value for an arbitrary interaction involves carrying out an integration over six dimensions. One of the primary advantages of an interaction that contains delta functions, like the Skyrme one, is that the evaluation of such integral becomes substantially simplified, by reducing the integral to only three dimensions

$$E = \langle \Phi | H | \Phi \rangle = \int d^3r \mathcal{H}(\mathbf{r}) \quad (88)$$

The Hamiltonian density  $\mathcal{H}(\mathbf{r})$  is composed of several terms

$$\mathcal{H} = \mathcal{K} + \mathcal{H}_0 + \mathcal{H}_{LS} + \mathcal{H}_C , \quad (89)$$

where the kinetic energy is given by

$$\mathcal{K} = \frac{\hbar^2}{2m} \tau \quad . \quad (90)$$

The value for the constant  $\hbar^2/2m$  involving the nucleon mass depends on the parameters used (corresponding values are listed in Table 1). The density-dependent terms in the Skyrme interaction are included in

$$\begin{aligned} \mathcal{H}_0 = & \frac{b_0}{2} \rho^2 - \frac{b'_0}{2} \sum_q \rho_q^2 \\ & + \frac{b_3}{3} \rho^{\alpha+2} - \frac{b'_3}{3} \rho^\alpha \sum_q \rho_q^2 \\ & + b_1 (\rho\tau - j^2) - b'_1 \sum_q (\rho_q \tau_q - j_q^2) \\ & - \frac{b_2}{2} \rho \nabla^2 \rho + \frac{b'_2}{2} \sum_q \rho_q \nabla^2 \rho_q \quad , \end{aligned} \quad (91)$$

where the general form of the particle densities ( $\rho, \rho_q$ ) and kinetic energy densities ( $\tau, \tau_q$ ) are described by Eqs. (38) and (40) from the last chapter. The current densities ( $\mathbf{j}, \mathbf{j}_q$ ) appearing in this term are identically zero for time-independent states and they will not be part of the energy density.

The finite-range spin-orbit terms have the form

$$\begin{aligned} \mathcal{H}_{LS} = & - b_4 \rho \nabla \cdot \mathbf{J} - b'_4 \sum_q \rho_q (\nabla \cdot \mathbf{J}_q) \\ & + \frac{\theta_{ls}}{12} \left[ \left( \frac{3}{2} b_1 + b_2 - b'_1 + 6b'_2 \right) \mathbf{J}^2(\mathbf{r}) + \left( -b_1 - 2b_2 + \frac{1}{2} b'_1 - 3b'_2 \right) \sum_q \mathbf{J}_q^2(\mathbf{r}) \right] \end{aligned} \quad (92)$$

In this work we use standard Skyrme forces (SkM\* and Sly4), for which the  $\mathbf{J}^2, \mathbf{J}_q^2$  terms in the spin-orbit functional are neglected ( $\theta_{ls} = 0$ ).

The Coulomb term contains an integral over the proton density as well as the Slater exchange term,

$$\mathcal{H}_C = \frac{e^2}{2} \int d^3r' \rho_p(\mathbf{r}) \frac{1}{|\mathbf{r} - \mathbf{r}'|} \rho_p(\mathbf{r}') - \frac{3}{4} e^2 \left( \frac{3}{\pi} \right)^{1/3} [\rho_p(\mathbf{r})]^{4/3} \quad . \quad (93)$$

Table 2: New parameterizations of the Skyrme forces. Values for  $b_0$ ,  $b'_0$ ,  $b_1$ ,  $b'_1$ ,  $b_2$ ,  $b'_2$ ,  $b_3$ ,  $b'_3$ ,  $b_4$ , and  $b'_4$  have been calculated using relations (86) and (87), from old parameterization [40, 42, 35]. Numbers have been rounded up to three decimal places.

Force	$b_0$	$b'_0$	$b_1$	$b'_1$	$b_2$
SkM*	-2764.025	-1560.55	68.75	68.125	170.625
$Z_\sigma$	-3145.945	-3316.251	64.495	58.315	148.877
SkT6	-2145.863	-1600.426	0.0	0.0	110.25
SLy4	-3526.790	-3320.210	32.484	-49.289	185.325
SkI1	1000.310	869.809	32.354	-49.803	-432.059
SkI3	-2034.628	-1424.936	32.301	-127.914	100.074
SkI4	-2231.708	-1679.676	32.271	-75.310	-121.462
SkP	-3359.948	-2322.346	44.642	89.284	190.343
SkO	-1882.032	-608.585	22.537	15.075	-72.754
SkO'	-2068.449	-987.770	19.156	8.312	41.250
Force	$b'_2$	$b_3$	$b'_3$	$b_4$	$b'_4$
SkM*	68.437	3898.75	1949.375	65.0	65.0
$Z_\sigma$	61.405	5577.823	6707.621	61.845	61.845
SkT6	0.0	4005.312	3204.25	53.5	53.5
SLy4	62.665	5776.007	6385.639	61.5	61.5
SkI1	-1136.719	580.693	-2810.714	62.13	62.13
SkI3	-124.799	3336.309	3632.793	94.254	0.0
SkI4	-528.369	3814.977	3991.101	183.097	-180.351
SkP	140.223	5100.600	3185.341	50.0	50.0
SkO	-358.023	2660.027	237.585	176.578	-198.749
SkO'	-128.648	3132.384	1192.344	143.895	-82.889

### 3.3 Single Particle Hamiltonian

The single particle Hartree–Fock Hamiltonian in Eq. (57) contains a kinetic energy, a nuclear potential, and a spin–orbit term

$$h_q = \hat{t}_q + \hat{v}_q + \hat{w}_q . \quad (94)$$

For the Skyrme effective interaction, the Hamiltonian can be written as

$$h_q = -\nabla \cdot \frac{\hbar^2}{2m_q^*} \nabla + U_q + U_C \cdot \delta_{q,p} + \frac{1}{2i} (\nabla \cdot \mathbf{I}_q + \mathbf{I}_q \cdot \nabla) - i\mathbf{B}_q \cdot (\nabla \times \sigma) , \quad (95)$$

where the first term corresponds to the kinetic energy ( $\hat{t}_q$ ),  $U_q$  is the nuclear central field ( $\hat{v}_q$ ) and  $U_C$  is the Coulomb interaction, in the case of protons. The spin-orbit field part ( $\hat{w}_q$ ) is

given by  $\mathbf{B}_q \cdot (\nabla \times \sigma)$ .

Several effective quantities appear in this equation. The effective mass is defined by

$$\frac{\hbar^2}{2m_q^*} = \frac{\hbar^2}{2m} + b_1 \rho - b'_1 \rho_q , \quad (96)$$

the effective current density by

$$\mathbf{I}_q = - 2 b_1 \mathbf{j} + 2 b'_1 \mathbf{j}_q , \quad (97)$$

and the effective spin density by

$$\mathbf{B}_q = b'_1 \mathbf{J}_q + b_4 \nabla \rho + b'_4 \nabla \rho_q . \quad (98)$$

As previously indicated, all of the terms in Eq.(97) vanish for bound states. Also, the first term in Eq.(98) is usually ignored.

The next sections show the construction of operators for the axial symmetry representation. The wavefunctions, Eqs. (69), show the same structure for upper and lower components when the Hamiltonian operates on them. We use this property of the quasiparticle wavefunctions, therefore only a bi-spinor structure is shown in the derivation of the operators, since the final result can be straightforwardly generalized for the four-spinor wavefunction.

### 3.3.1 Kinetic Energy Operator

Starting from the general kinetic energy term in Eq. (95)

$$- \hat{t}_q = \nabla \cdot \frac{\hbar^2}{2m_q^*} \nabla \psi , \quad (99)$$

In the evaluation of the kinetic energy we make use of the  $\varphi$  independence of the effective mass. The following operator identity is useful [48]:

$$\nabla \cdot f \nabla \psi = (\nabla f) \cdot (\nabla \psi) + f \nabla^2 \psi . \quad (100)$$

Applying the cylindrical form of the Laplacian operator to the standard form of the upper or lower component of the wavefunction in Eq. (69), and making use of the axial symmetry of  $f$  we find

$$f \nabla^2 \psi = \frac{f}{\sqrt{2\pi}} \begin{pmatrix} e^{i(\Omega-1/2)\varphi} \left( \frac{\partial^2 U}{\partial r^2} + \frac{1}{r} \frac{\partial U}{\partial r} - \left( \frac{\Omega-1/2}{r} \right)^2 U + \frac{\partial^2 U}{\partial z^2} \right) \\ e^{i(\Omega+1/2)\varphi} \left( \frac{\partial^2 L}{\partial r^2} + \frac{1}{r} \frac{\partial L}{\partial r} - \left( \frac{\Omega+1/2}{r} \right)^2 L + \frac{\partial^2 L}{\partial z^2} \right) \end{pmatrix} \quad (101)$$

and

$$(\nabla f) \cdot (\nabla \psi) = \frac{1}{\sqrt{2\pi}} \begin{pmatrix} e^{i(\Omega-1/2)\varphi} \left( \frac{\partial f}{\partial r} \frac{\partial U}{\partial r} + \frac{\partial f}{\partial z} \frac{\partial U}{\partial z} \right) \\ e^{i(\Omega+1/2)\varphi} \left( \frac{\partial f}{\partial r} \frac{\partial L}{\partial r} + \frac{\partial f}{\partial z} \frac{\partial L}{\partial z} \right) \end{pmatrix} . \quad (102)$$

$U$  and  $L$  represent the upper and lower spinors of either  $\phi^{(1)}$  or  $\phi^{(2)}$  in wavefunctions (69). In spin space, the kinetic energy operator for the two-dimensional spinors  $U^{(i)}(r, z), L^{(i)}(r, z)$  defined in Eq.(70) can be written as

$$-\hat{t}_q = \begin{pmatrix} t_{11} & 0 \\ 0 & t_{22} \end{pmatrix} , \quad (103)$$

whose elements are given by

$$t_{11} = f \left( \frac{\partial^2}{\partial r^2} + \frac{1}{r} \frac{\partial}{\partial r} - \left( \frac{(\Omega - 1/2)}{r} \right)^2 + \frac{\partial^2}{\partial z^2} \right) + \frac{\partial f}{\partial r} \frac{\partial}{\partial r} + \frac{\partial f}{\partial z} \frac{\partial}{\partial z} \quad (104)$$

$$t_{22} = f \left( \frac{\partial^2}{\partial r^2} + \frac{1}{r} \frac{\partial}{\partial r} - \left( \frac{(\Omega + 1/2)}{r} \right)^2 + \frac{\partial^2}{\partial z^2} \right) + \frac{\partial f}{\partial r} \frac{\partial}{\partial r} + \frac{\partial f}{\partial z} \frac{\partial}{\partial z} , \quad (105)$$

$f$  being the effective mass given in Eq. (96).

### 3.3.2 Nuclear Potential Operator

The local potential terms acting on  $\phi^{(1)}$  or  $\phi^{(2)}$  can also be cast into a matrix form

$$\hat{v}_q = \begin{pmatrix} v_{11} & 0 \\ 0 & v_{22} \end{pmatrix} , \quad (106)$$

where

$$v_{11} = v_{22} = U_q + U_C . \quad (107)$$

For Skyrme forces SkM\* and SLy4 the effective nuclear potential is given by

$$\begin{aligned} U_q &= b_0 \rho - b'_0 \rho_q + b_1 \tau - b'_1 \tau_q \\ &+ \frac{b_3}{3} (\alpha + 2) \rho^{\alpha+1} - \frac{b'_3}{3} \left[ \alpha \rho^{\alpha-1} \sum_q \rho_q^2 + 2 \rho^\alpha \rho_q \right] \\ &- b_4 \nabla \cdot \mathbf{J} - b'_4 \nabla \cdot \mathbf{J}_q + b'_2 \nabla^2 \rho_q - b_2 \nabla^2 \rho , \end{aligned} \quad (108)$$

and the Coulomb field together with the Slater exchange correction is

$$U_C = e^2 \int d^3 r' \frac{\rho_p(\mathbf{r}')}{|\mathbf{r} - \mathbf{r}'|} - e^2 \left( \frac{3}{\pi} \right)^{1/3} [\rho_p(\mathbf{r})]^{1/3} . \quad (109)$$

### 3.3.3 Evaluation of the Coulomb Potential

The calculation of the Coulomb potential requires the evaluation of the integral

$$U_C(\mathbf{r}') = e^2 \int d^3r \frac{\rho_p(\mathbf{r})}{|\mathbf{r} - \mathbf{r}'|} . \quad (110)$$

The direct integration method was selected since the axial symmetry of the system can be exploited to reduce the computational effort. In order to avoid dealing with the singularities, we follow a technique used by Vautherin, et. al [49]. Using the relation

$$\nabla_{\mathbf{r}}^2 |\mathbf{r}' - \mathbf{r}| = \frac{2}{|\mathbf{r}' - \mathbf{r}|} , \quad (111)$$

we ignore surface terms and integrate the formal solution by parts two times

$$\begin{aligned} U_C(\mathbf{r}') &= e^2 \int d^3r \frac{\rho_p(\mathbf{r})}{|\mathbf{r}' - \mathbf{r}|} \\ &= \frac{1}{2} e^2 \int d^3r \rho_p(\mathbf{r}) \nabla^2 |\mathbf{r}' - \mathbf{r}| \\ &= \frac{1}{2} e^2 \int d^3r [\nabla^2 \rho_p(\mathbf{r})] |\mathbf{r}' - \mathbf{r}| \end{aligned}$$

The integral is expressed in cylindrical coordinates, and the definition of the Poisson equation is used,

$$\begin{aligned} U_C(\mathbf{r}') &= e^2 \int_0^\infty r dr \int_{-\infty}^{+\infty} dz \int_0^\pi d\varphi [\nabla^2 \rho_p(r, z)] \sqrt{(z - z')^2 + r^2 + r'^2 + 2rr' \cos \varphi} \\ &= 2e^2 \int_0^\infty r dr \int_{-\infty}^{+\infty} dz [\nabla^2 \rho_p(r, z)] \sqrt{(z - z')^2 + (r + r')^2} \int_0^{\pi/2} d\xi \sqrt{1 - \chi \sin^2 \xi} \end{aligned}$$

The integral over  $\xi$  is the defining equation for  $E(\chi)$  — a complete elliptic integral of the second kind that can be easily evaluated.

### 3.3.4 Spin-orbit Operator

When acting on either component of the HFB four-spinor wavefunction, the Hartree-Fock spin-orbit operator

$$\hat{w}_q = -i \mathbf{B}_q \cdot (\nabla \times \sigma) ; , \quad (112)$$

can similarly be written the form

$$\hat{w}_q = \begin{pmatrix} w_{11} & w_{12} \\ w_{21} & w_{22} \end{pmatrix} , \quad (113)$$

with [48]

$$\begin{aligned}
 w_{11} &= \mathcal{B}_r \frac{\Omega - 1/2}{r} \\
 w_{12} &= \left[ -\mathcal{B}_z \frac{\Omega + 1/2}{r} - \mathcal{B}_z \frac{\partial}{\partial r} + \mathcal{B}_r \frac{\partial}{\partial z} \right] \\
 w_{21} &= \left[ -\mathcal{B}_z \frac{\Omega - 1/2}{r} + \mathcal{B}_z \frac{\partial}{\partial r} - \mathcal{B}_r \frac{\partial}{\partial z} \right] \\
 w_{22} &= -\mathcal{B}_r \frac{\Omega + 1/2}{r},
 \end{aligned}$$

$\mathcal{B}_r$  and  $\mathcal{B}_z$  for the spin-orbit part representation of the potential operator are given by:

$$\begin{aligned}
 \mathcal{B}_r &\equiv \mathbf{B}_q \cdot \mathbf{e}_r = \nabla_r (b_4 \rho + b'_4 \rho_q) \\
 \mathcal{B}_z &\equiv \mathbf{B}_q \cdot \mathbf{e}_z = \nabla_z (b_4 \rho + b'_4 \rho_q)
 \end{aligned}$$

$b_4$  and  $b'_4$  values are shown in Table 2 for different forces.

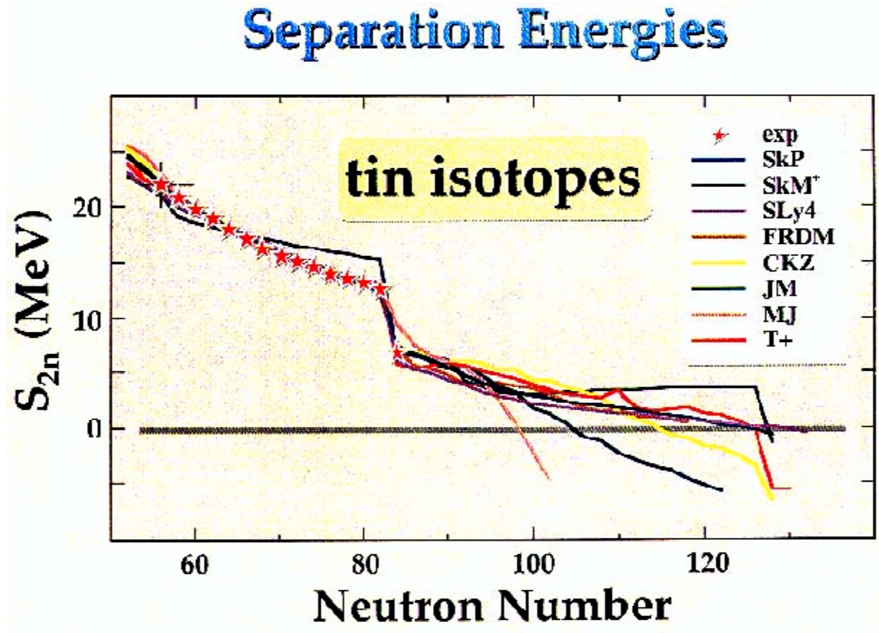


Figure 8: Two-neutron separation energies for a chain of tin isotopes [4]. The results of the calculations -some of them with Skyrme forces- are compared with the experimental measurements.

The single-particle Hartree-Fock Hamiltonian, Eq. (94), is used depending on the parameterization utilized, to construct the Hartree-Fock-Bogoliubov Hamiltonian. As mentioned before, the calculations presented in this work are limited to the SkM\* [42] and SLy4 [45] forces. The former has been extensively used and a significant number of results is available. The latter is more recent and has been shown to improve the results when compared to experimental data. Figure 8 shows this evidence.



## CHAPTER IV

### BASIS SPLINE REPRESENTATION

The solution of the Hartree-Fock-Bogoliubov equations in coordinate space requires a suitable method of numerical representation that generates highly accurate results. Typically, the low-order finite difference method is the most widely used for solving differential equations on a lattice. The basis-splines (B-spline) method used in this work provides a higher order interpolation alternative and, analogous to the finite difference method, leads to a vector-matrix representation of continuous functions on a lattice. The advantage of the B-spline method is that it produces the same level of accuracy as the finite difference with a smaller number of points [50], thereby reducing significantly the computational load.

The solution of differential equations through the B-splines method has been successfully demonstrated in a number of physical applications. More importantly, the representation of the B-splines on the lattice shown here has been applied extensively on nuclear structure [51, 50, 52, 48, 53].

The representation of functions and operators based on the B-splines method is discussed in this chapter. The iterative technique based in the B-spline representation will be described in the next chapter.

#### 4.1 B-Spline representation of functions

The Basis-Spline functions  $B_i^M(x)$  are piecewise-continuous polynomials (i.e. Legendre type) of order  $(M - 1)$  [51]. These segments of polynomials are joined together at points called *knots*. The number of knots  $\{x_i\}$  on the grid is rather arbitrary, as are the positions of the knots on the lattice. Figure 9 shows a spline of order  $M = 5$  generated in a linear region  $(x_i, x_{i+5})$ .

A continuous function  $f(x)$  defined in the interval  $(x_{min}, x_{max})$  is approximated in terms of B-splines as

$$\bar{f}(x) \approx \sum_{i=1} B_i^M(x) a^i , \quad (114)$$

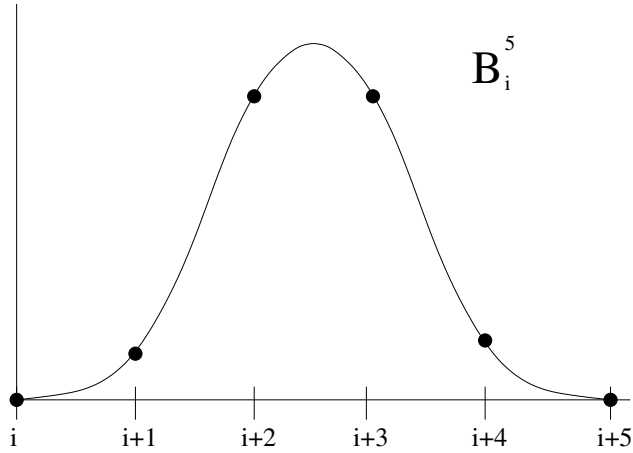


Figure 9: Spline of order  $M=5$ . The knots are indicated as black dots. This is the case of a linear distribution of the knots. The spline shown starts on  $x_i$  and finishes at  $x_{i+M}$ .

where  $M$  is the splines order and  $a^i$  are the expansion coefficients. The sum goes over the total number of splines used in the basis set.

#### 4.1.1 Collocation method

The collocation method requires Eq.(114) to be evaluated exactly at a set of *collocation* points  $\{x_\alpha\}$ . There is a number of ways to choose where to place the collocation points. In our approach we selected the positions at which the maxima of the splines occur [48]. With this choice, the number of collocation points is equal to the number of splines used in the set of Eq. (114). Furthermore, this distribution of the collocation points assigns more points to the boundaries, where critical boundary conditions are expected to take place.

The set of splines  $B_i^M$  is generated in a physical region, and a number of arbitrary segments ( $N$ ) inside the mesh must be defined. The knots are defined by distributing a series of points ( $N + 1$ ) inside the physical region and adding  $M - 1$  points at the boundaries. The number of knots then, is given by

$$\mathcal{N} = 2M + N - 1, \quad (115)$$

and the number of splines in the set is  $M + N - 1$ . Figure 10 shows a set of 5th-order splines within a region (0,8). The corresponding number of knots is 17 and the number of collocation

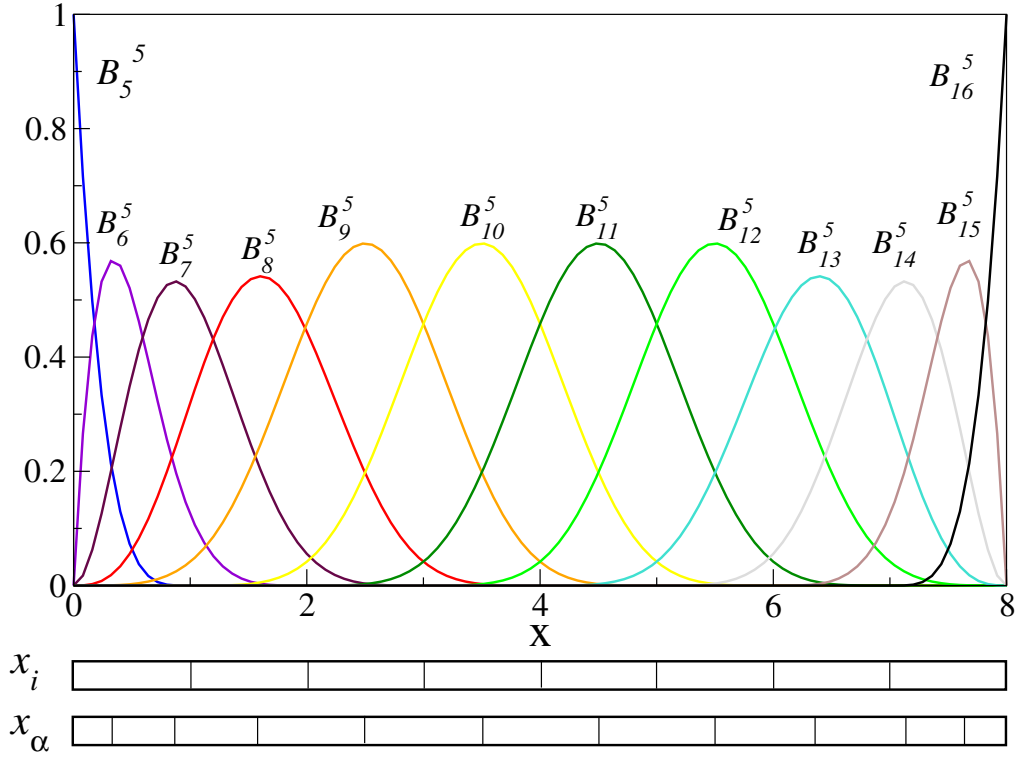


Figure 10: Set of splines of order  $M = 5$  from a region 0 to 8. The positions of the knots  $x_i$  and the collocation points  $x_\alpha$  are marked on the bars. The boundaries present a knot multiplicity of 5 each one.

points is 12 (the same, of course, as the number of splines). This is based on  $N = 8$ . The distribution of the collocation points ( $x_\alpha$ ) is not entirely linear, only in the central region, where  $M \leq \alpha \leq N$ . In Fig. 10 these points correspond to where the maximum of the four central splines are located. In this region the spacing is exactly of 1 unit between nodes, but it gets tighter at both ends.

#### 4.1.2 Representation of the eigenvalue problem

The typical eigenvalue problem includes equations of the type

$$\begin{aligned} \mathcal{O}\bar{f}(x) &= \bar{g}(x) \\ \text{with } \bar{g}(x) &= \lambda \bar{f}(x). \end{aligned} \tag{116}$$

The operator  $\mathcal{O}$  represents the Hamiltonian of the system and  $\bar{f}$  is the eigenvector (wave-function) corresponding to the eigenvalue  $\lambda$  (energy).

Because the functions  $f(x)$  and  $g(x)$  are approximations to the exact functions  $\bar{f}(x)$  and  $\bar{g}(x)$ , the operator equation will in general only be approximately fulfilled

$$\mathcal{O}f(x) - g(x) = R(x) . \quad (117)$$

The quantity  $R(x)$  is called the *residual*. It is a measure of the accuracy of the lattice representation. The collocation method requires the residual to vanish

$$\int v(x) \delta(x - x_\alpha) R(x) dx \stackrel{!}{=} 0 . \quad (118)$$

The volume element weight function  $v(x)$  in the integrals emphasizes that the formalism applies to arbitrary curvilinear coordinates. Our case of interest is in the use of polar coordinates, where this function has the form  $v(x) = x$ .

Condition (118) assures that the expansion is evaluated exactly at the collocation points:

$$f_\alpha = f(x_\alpha) = \sum_{i=M}^{N+M} B_i^M(x_\alpha) a^i = \sum_{i=M}^{N+M} B_{\alpha i} a^i = \bar{f}_\alpha \quad (119)$$

The last line of Eq.(119) shows already the notation being used below in what remains of the current derivation of the collocation method. The expansion coefficients  $a^i$  come from the exact evaluation of the original function at the collocation points, giving an adequate extrapolation to the rest of the points. We can evaluate the expansion coefficients  $a^i$  by inversion of Eq. (119):

$$a^i = \sum_{\alpha} \tilde{B}^{i\alpha} f_\alpha , \quad (120)$$

where  $\tilde{B}^{i\alpha}$  is the inverted  $B_{\alpha i}$  matrix including the evaluation at the boundary points. Now the sum goes over the collocation points. Suppose that the expansion coefficients of  $f(x)$  and  $g(x)$  are  $a^i$  and  $b^j$  respectively. Using the collocation method condition (118) and inserting the B-spline expansion (119) of the functions  $f(x)$  and  $g(x)$ , Eq. (117) can be rewritten

$$\sum_i [\mathcal{O}B]_{\alpha i} a^i - \sum_j B_{\alpha j} b^j = 0 , \quad (121)$$

$$\text{or } \sum_{i\beta} [\mathcal{O}B]_{\alpha i} \tilde{B}^{i\beta} f_\beta = \sum_{j\gamma} B_{\alpha j} \tilde{B}^{j\gamma} g_\gamma . \quad (122)$$

Making use of the spline property  $\sum_j B_{\alpha j} \tilde{B}^{j\gamma} = \delta_\alpha^\gamma$  on the left side of (122), we end up with

$$\sum_{i\beta} [\mathcal{O}B]_{\alpha i} \tilde{B}^{i\beta} f_\beta = g_\alpha , \quad (123)$$

to finally get the collocation-method representation of an operator

$$\mathcal{O}_\alpha^\beta = \sum_i [\mathcal{O}B]_{\alpha i} \tilde{B}^{i\beta} \quad (124)$$

#### 4.1.3 Basis Spline Galerkin method

The collocation method gives a way to achieve reduction of local error. The Galerkin method provides a global error reduction to the B-splines representation. To derive the Galerkin representation, we multiply Eq. (117) from the left with the spline function  $B_k(x)$  and integrate over  $x$  with the proper weight element

$$\int v(x) B_k(x) \mathcal{O}f(x) dx - \int v(x) B_k(x) g(x) dx = \int v(x) B_k(x) R(x) dx . \quad (125)$$

Various schemes exist to minimize the residual function  $R(x)$ ; in the Galerkin method one requires that there be no overlap between the residual and an arbitrary B-spline function

$$\int v(x) B_k(x) R(x) dx \stackrel{!}{=} 0 . \quad (126)$$

This condition amounts to a global reduction of the residual. We apply the Galerkin condition to Eq.(125) and insert the B-Spline expansions for the functions  $f(x)$  and  $g(x)$ , like it was done in the last section

$$\sum_i \left[ \int v(x) B_k(x) \mathcal{O}B_i(x) dx \right] a^i - \sum_i \left[ \int v(x) B_k(x) B_i(x) dx \right] b^i = 0 . \quad (127)$$

Defining the matrix elements

$$\mathcal{O}_{ki} = \int v(x) B_k(x) \mathcal{O}B_i(x) dx , \quad G_{ki} = \int v(x) B_k(x) B_i(x) dx . \quad (128)$$

transforms the differential equation into a matrix  $\times$  vector equation

$$\sum_i \mathcal{O}_{ki} a^i = \sum_i G_{ki} b^i . \quad (129)$$

The matrix  $G_{ki}$  is called the *Gram* matrix and represents the nonvanishing overlap integrals between different B-Spline functions. In analogy to the splines, it holds property

$$\sum_k G^{jk} G_{ki} = \delta_i^j . \quad (130)$$

Again, the expansion coefficients  $a^i$  and  $b^i$  are substituted with corresponding inversions on Eq. (129)

$$\sum_{i\beta} \mathcal{O}_{ki} \tilde{B}^{i\beta} f_\beta = \sum_{j\alpha} G_{kj} \tilde{B}^{j\alpha} g_\alpha . \quad (131)$$

Solving for  $g_\alpha$  we get

$$\sum_\beta \mathcal{O}_\alpha^\beta f_\beta = g_\alpha \quad (132)$$

with the differential operator definition on the Galerkin method:

$$\mathcal{O}_\alpha^\beta = \sum_{ijk} \tilde{B}_{\alpha i} G^{ij} \mathcal{O}_{jk} \tilde{B}^{k\beta} . \quad (133)$$

The operators representations, Eqs. (124,133), are ideal for matrix operations and can be implemented for computer calculations. The splines formalism derived so far assumes that the operator acting on the function  $f$  operates solely on a given coordinate. Typically, mean field problems involve functions of several variables. In our symmetry, the operators are the first and second derivatives with respect to  $r$  or  $z$ . Luckily, the rest of the operators are only local potentials that act trivially on the wavefunctions. Therefore, the implementation of the splines representation can be treated the same way as in the operators case.

## CHAPTER V

### NUMERICAL IMPLEMENTATION

This chapter includes the description of the techniques used to implement the HFB equations from Chapter II for numerical calculations.

A basis-splines hybrid method [51, 53, 48] is used to represent the Hamiltonian in the lattice. The derivative operators are constructed using the Galerkin method as described on Chapter IV; this amounts to a global error reduction. The local potentials are represented by the basis-spline collocation method to achieve local error reduction. With the use of the Skyrme forces, the lattice representation transforms the differential operator equation into a matrix form

$$\sum_{\nu=1}^N \mathcal{H}_{\mu}^{\nu} \psi_{\nu}^{\Omega} = E_{\mu}^{\Omega} \psi_{\mu}^{\Omega} \quad (\mu = 1, \dots, N) . \quad (134)$$

For a given quantum number  $\Omega$ , we solve the eigenvalue problem through means of direct diagonalization on a two-dimensional grid  $(r_{\alpha}, z_{\beta})$ , where  $\alpha = 1, \dots, N_r$  and  $\beta = 1, \dots, N_z$  represent the number of physical elements in each direction (collocation points,  $x_{\alpha}$ ). Each of the four components of the spinor wavefunction  $\psi(r, z)$  is represented on the two-dimensional lattice by an expansion in basis-spline functions  $B_i(x)$  evaluated at the lattice support points. After each diagonalization of the Hamiltonian, the wavefunctions are reconstructed from the resultant matrix. The output of the calculations depends strongly on the maximum number of the angular momentum projection,  $\Omega$  as it will be shown on Chapter VI.

The starting point of the calculations requires the use of a beforehand generated set of wavefunctions or densities. They can be provided by solving solving the Schrödinger equation for a given well-defined analytical potential. A better approximation to the initial wavefunctions is usually contributed by the outcome of a Hartree Fock + BCS previous calculation. It makes the HFB calculation process converge substantially faster.

Since the problem of Eq. (134) is self-consistent we use an iterative method for the solution. In every iteration the full HFB Hamiltonian is constructed in coordinate space,

and diagonalized. The Fermi level,  $\lambda$ , is recalculated after every iteration is completed. The new value of  $\lambda$  is used for the next iteration. Due to the axial symmetry the diagonalization is performed for each value of  $j_z$  ( $\Omega$ ) and isospin (n,p) separately. This iterative process is done until a suitable convergence is achieved. Typically 15-20 iterations are sufficient to obtain convergence at the level of one part in  $10^5$  for the total binding energy.

## 5.1 Initialization

The HFB calculations are performed in several stages, as seen in Figure 12. This figure shows a flowchart of the logic behind the HFB computations. We can observe two main blocks: one corresponds to the initialization of the HFB calculations and the second is the HFB calculation process itself after reading the initial parameters.

The second stage, or main program, requires a set of approximate wavefunctions or densities to start the iterative process. The input files containing these quantities are read, and several steps are performed repeatedly as indicated by the outer arrow on the lower block in Fig. 12.

One of the options for the input of the initial step is the use of HF+BCS. This has been already theoretically described in Chapter II. Its outcome (particle densities mainly) is used as a starting point in the HFB calculation. The second option is to use the wavefunctions generated from the solution of the Schrödinger equation with the axially deformed Woods-Saxon potential [48] described next.

### 5.1.1 Deformed Woods-Saxon potential

This approach consists of the solution of the eigenvalue problem based in the deformed Woods-Saxon potential

$$U_{WS} = V_0 \frac{1 + \kappa(N - Z)/(N + Z)}{1 + \exp(\xi/a)}, \quad (135)$$

where  $V_0$  is the strength parameter ( $\approx 50$  Mev),  $\kappa$  is an isospin parameter,  $a$  is the diffuseness parameter and  $\xi$  is the perpendicular distance to the nuclear surface. The single-particle Hamiltonian ( $H = t + v$ , where  $v = U_{WS}$ ) is constructed based on this form of the nuclear potential with corresponding parameters [54]. The resulting Hamiltonian is then diagonalized



to get a set of wavefunctions and eigenenergies corresponding to the defined grid and nucleus characteristics. The output is stored in a separate file to be used by the HF+BCS program or to be directly read by the HFB code. In this way then, a simple solution of the eigenvalue

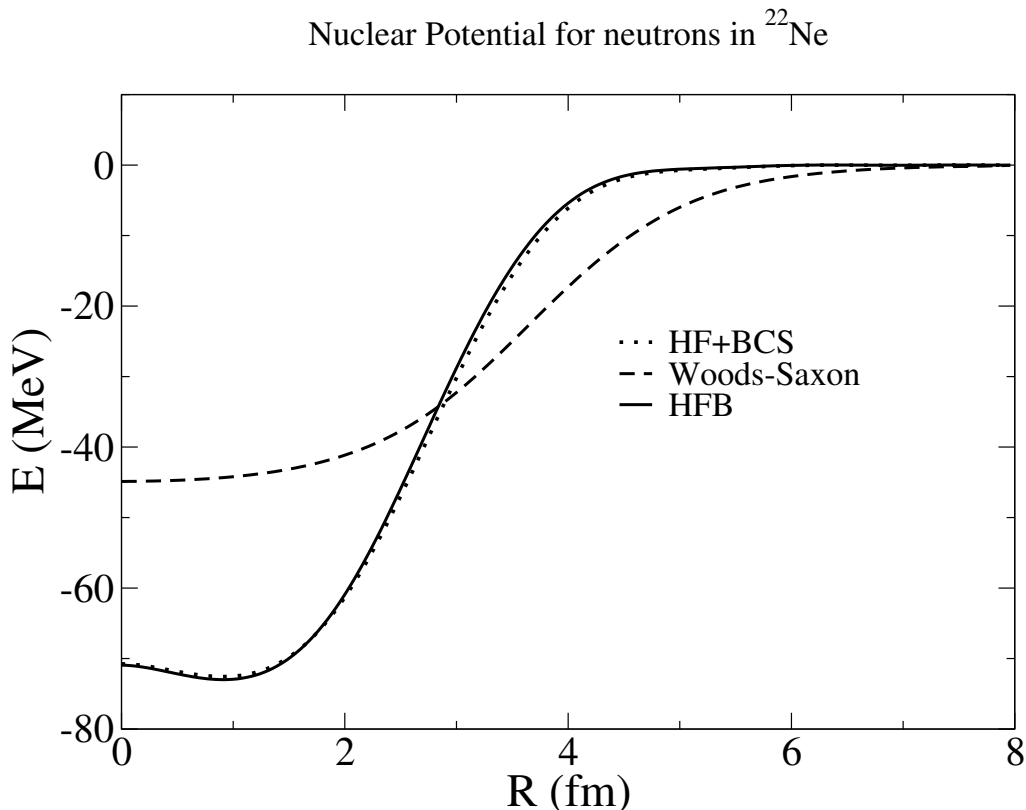


Figure 11: Neutron potential for  $^{22}\text{Ne}$  as function of the radial coordinate, for the Woods-Saxon potential, HF+BCS and HFB. The potential calculated with HF+BCS is substantially closer to the HFB mean field than the Woods-Saxon potential.

problem for the Woods-Saxon potential is useful for generating the HFB input. It is better, though, to make use of the HF+BCS output, since its approximate solution is closer to the one resulting from HFB. Figure 11 reaffirms this statement by showing the W-S potential and the mean field of HF+BCS in  $^{22}\text{Ne}$ . They are compared to the mean field resultant from the HFB calculation. The HF potential is practically the same as the HFB potential in this case because the degree of pairing of  $^{22}\text{Ne}$  is very small.

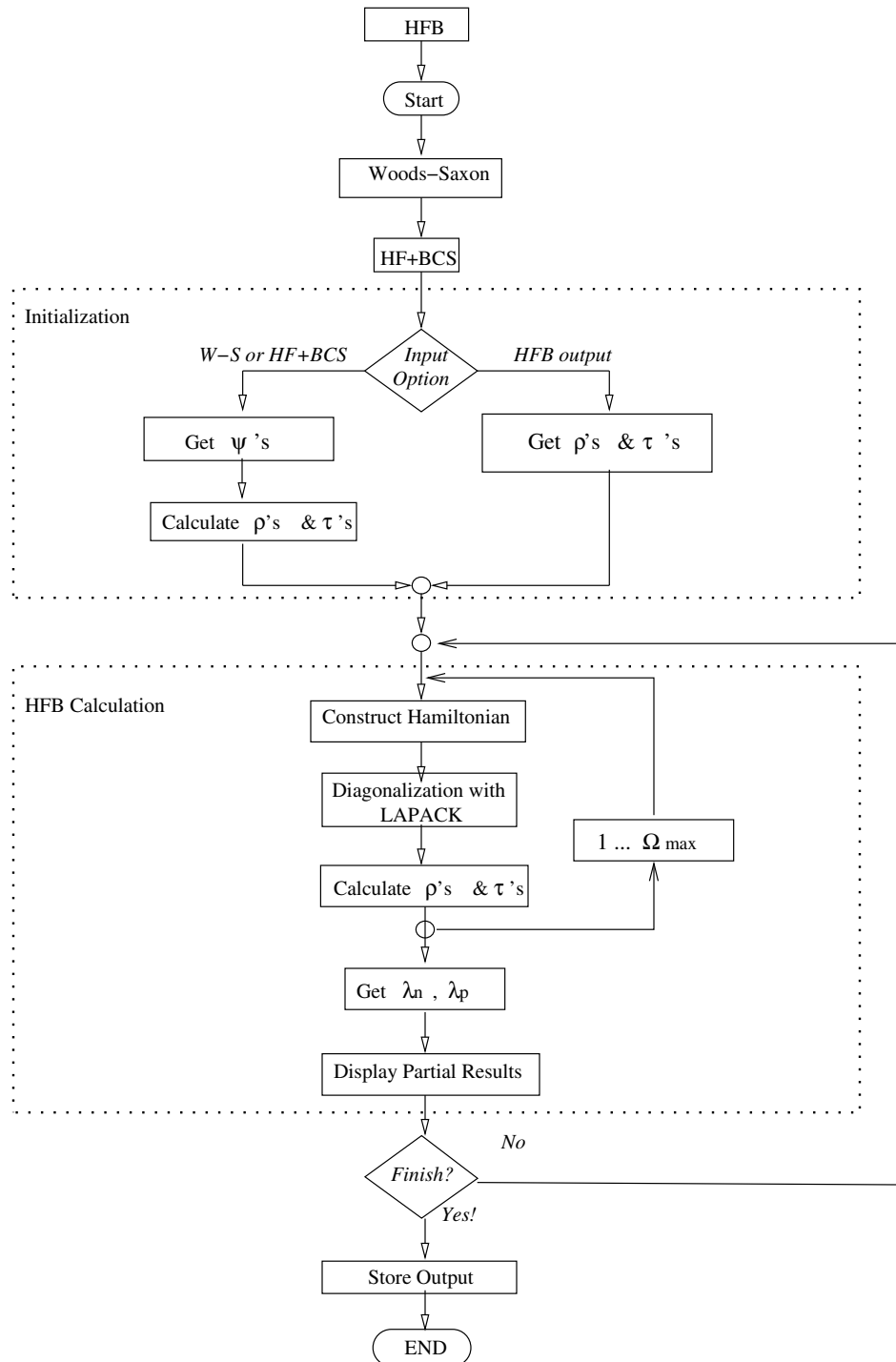


Figure 12: Flowchart of the HFB calculations. There are two main logical blocks: the first one for the initialization and the second one for the actual HFB calculations. The process is iterative until convergence is reached. All the output information is stored at the end in case it is needed for further iterations.

## 5.2 Description of the main iterative process

The main block in Fig. 12 labeled “HFB Calculation” receives the output of the deformed Woods-Saxon (wavefunctions) or HF+BCS (densities). If the user chooses to use Woods-Saxon potential, the single particle wavefunctions are passed as HFB input parameters. In this case, the main HFB routine constructs the initial densities from such wavefunctions. On the other hand, if the initialization choice is made from the HF+BCS outcome, the particle densities  $\rho$  and  $\tau$  will be read directly by the HFB code. Before this setting up of the initial densities, the pertinent mesh information is read.

All the above steps are made in the stage called “Initialization” in Fig. 12. The goal of this first step is to get the initial densities, which will be used to form the Hamiltonian in the first iteration of the HFB process. The iterative calculation explained next is done for neutrons and protons separately. From the initial densities, the potentials  $U_q, U_C, \mathbf{B}_q \cdot (\nabla \times \sigma)$  are constructed according to corresponding representation in coordinate space for cylindrical coordinates (Chapter III). Now, for every  $\Omega$  number, the single-particle Hamiltonian and pairing Hamiltonian, Eqs. (95) and (53) are constructed. The resulting Hamiltonian is then diagonalized using specialized LAPACK libraries. The wavefunctions and corresponding eigenenergies for a given isospin and projection of angular momentum are obtained from this process. The quasiparticle wavefunctions are then normalized using condition (75), and the densities  $\rho_q, \tau_q$  are constructed with the eigenvectors obtained. The partial results of the particle and pairing densities are then accumulated until the same process is applied to all the  $\Omega$  values, for a given isospin.

The density matrices are then mixed to the ones calculated previously, according to a *damping factor* selected in the input file. A percentage of the new result is added to the remaining percentage of the older result to form a composite density

$$\rho = dmp * \rho_i + (dmp - 1) * \rho_{i-1} , \quad (136)$$

$dmp$  being a factor between 0 and 1. This is done in order to avoid large changes in the densities and smooth out the results from iteration to iteration. Fig. 13 shows the damping factor effect on the binding energy calculation of  $^{22}Ne$ . It can be observed that the closer to one this factor is chosen, the more oscillations will occur in the evolutions of the result. On

the other hand, if the value is close to zero, more iterations will be needed since the whole process is slower to converge. An optimum damping value can be found between zero and one.

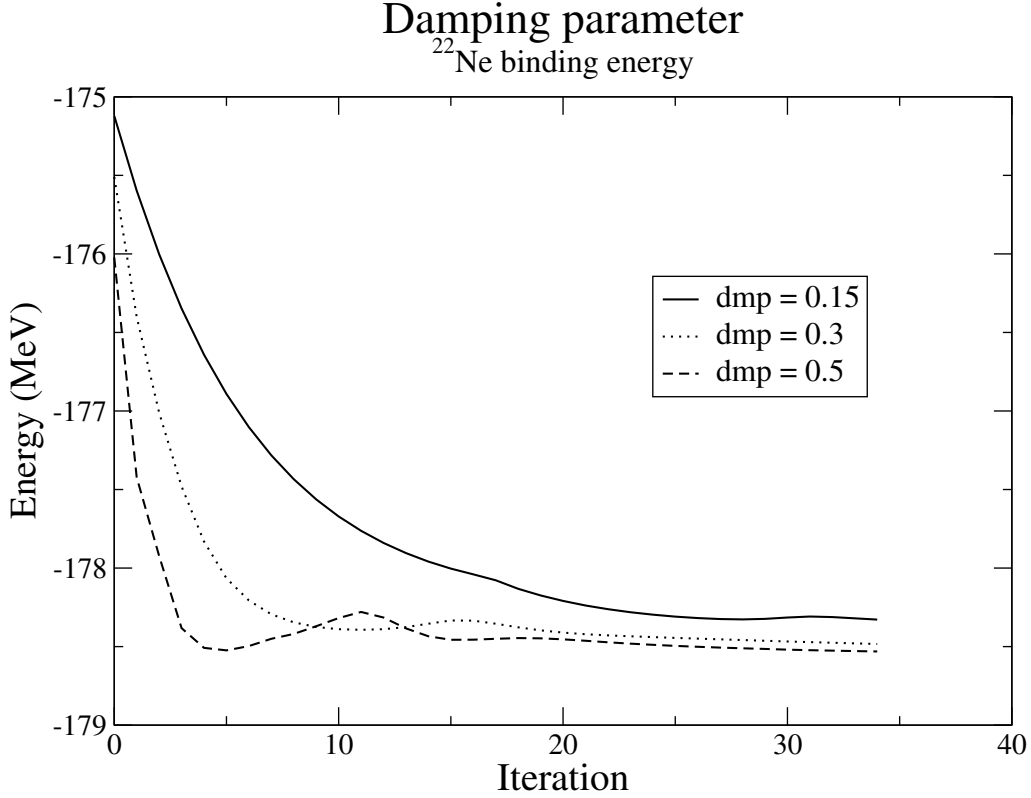


Figure 13: Calculation of binding energy in  $^{22}\text{Ne}$  vs. iteration number. Three different values of the damping factor are shown. The best value in this case is the middle one,  $\text{dmp}=0.3$ , since it gives the least oscillatory behavior and converges rapidly.

After the diagonalization process is completed, the Fermi level  $\lambda$ , is calculated for neutrons and protons. It is calculated by means of a simple root search using the equations [5]

$$\Delta_n = 2E_n \sqrt{N_n(1 - N_n)} \quad (137)$$

$$N_n = \frac{1}{2} \left[ 1 - \frac{\varepsilon_n - \lambda}{((\varepsilon_n - \lambda)^2 + \Delta_n^2)^{\frac{1}{2}}} \right], \quad (138)$$

where  $N_n$  is the norm of the second component of the  $E_n^\Omega$  quasiparticle energy state, and  $\varepsilon_n$  is the equivalent single-particle energy according to the BCS-like relation

$$\varepsilon_n = E_n(1 - 2N_n) + \lambda, \quad (139)$$

for that state.  $\Delta_n$  is the energy gap corresponding to each state, but only has an auxiliary meaning. The calculated value  $\lambda$  in this way is used for the next iteration.

Once the calculations of one iteration are finished, the binding energy is computed. The values of the binding energy components are obtained integrating each energy density, Eqs. (90), (91) and (92). The partial energies and the total binding energy are written to the output file. Other quantities stored for display are particle number of neutrons and protons,  $N_q$ , the corresponding energy gaps  $\Delta_q$  (Eq. 55), quadrupole moments  $(Q_{zz}, Q_{20}, \beta_2)$  and Fermi energies  $\lambda_q$ .

For the next iteration, the calculated values of the particle and pairing densities, along with the new Fermi level, will be utilized to construct the Hamiltonian for each  $\Omega$ , and so on. The process described above is done until a suitable convergence is achieved. When all the calculations have been made according to the maximum number of iterations, then the program stores the final values of  $\lambda_q$ ,  $\Delta_q$ , and information about the grid in use. The quasiparticle spectrum and the equivalent single particle spectrum are stored in a separate file, with their corresponding occupancies. A set of output files for plotting the potentials and wavefunctions are also generated. The output files generated might also be useful for performing further iterations, if higher convergence is desired.

### 5.3 First test of a trivial case: $^{16}\text{O}$

The HFB theory differs from the HF theory in the inclusion of the pairing treatment. When there is no pairing, both cases must give the same outcome. This reasoning is behind the decision to perform a calculation on stable oxygen isotope  $^{16}\text{O}$ . This nucleus has four single particle states with occupation of exactly one: three with  $\Omega = 1/2$  and one with  $\Omega = 3/2$ .

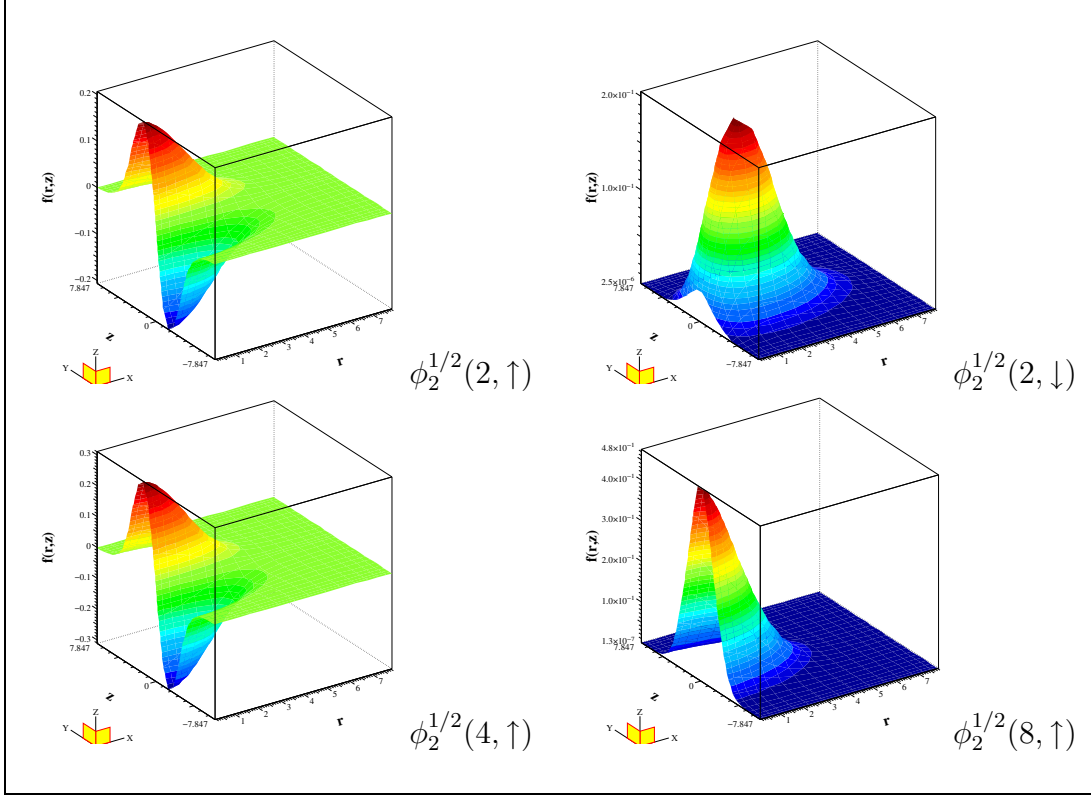


Figure 14: Main  $^{16}\text{O}$  wavefunctions in the  $s_{1/2}$  shell. They are labeled according to the quasiparticle spectrum. The  $\phi_2^{1/2}(8, \uparrow)$  wavefunction corresponds to the state of the lowest equivalent single-particle energy. All three states have an occupancy of exactly one.

Table 3: HFB+SkM\* calculations for  $^{16}\text{O}$  with different methods. The total binding energy and the single particle energies of the states shown on Fig.14 are displayed for comparison with Hartree-Fock calculations.

	HF(1D)[55]	HF(3D)[50]	HF+BCS [48]	HFB
B. E. (MeV)	-127.73	-127.73	-127.74	-127.74
$E(s_{1/2})$ (MeV)	-33.307	-33.308	-33.307	-33.307
$E(p_{3/2})$ (MeV)	-19.882	-19.880	-19.884	-19.884
$E(p_{1/2})$ (MeV)	-13.551	-13.545	-13.541	-13.541

Figure 14 shows the wavefunctions in axial symmetry of the occupied states. Furthermore, since there are no pairing effects, the energy gap for both neutrons and protons is zero. In such case the calculated binding energy and other observables are the same in the HFB and HF frame, as shown in Table 3. Here, the calculations made with one-dimensional and three-dimensional HF codes are included. This is done to show that the HFB code is able to reproduce the results of HF calculations in the limit of nuclei without pairing.

All four computations in Table 3 give the same binding energy value, with slight differences in the occupied single-particle states (in the order of a few KeVs). The conclusion of this demonstration is that, at least in the axial symmetry, the results in the case of a non-gap nucleus are exactly the same. More tests are performed in the next section for nuclei showing more complicated features.

## CHAPTER VI

### RESULTS

This chapter shows several results of tests and studies made with axially symmetric HFB code. The results and their discussions are divided in three sections. The first one presents a series of studies of the observable variables performed on  $^{22}\text{O}$ , in terms of the numerical parameters involved in the computations. The second section includes a study of the tin isotope  $^{150}\text{Sn}$ . This section is focused on the energy spectrum and the characteristics of the quasiparticle wavefunctions corresponding to  $^{150}\text{Sn}$ . The last section shows the results of calculations performed on  $^{22}\text{O}$ ,  $^{150}\text{Sn}$ ,  $^{102}\text{Zr}$ . These are compared to calculations made with other methods. The reproducibility of such results through the axial HFB computations is tested for the cases in which the characteristics (mainly geometrical shapes) of the mentioned nuclei allow such comparisons.

#### 6.1 Numerical parameters: $^{22}\text{O}$ calculations

This section presents a series of studies of the numerical parameters in axially symmetric HFB calculations. In particular, the study of the observables dependence on the equivalent single particle energy cutoff, the lattice box size, the number of mesh points, and the maximum angular momentum quantum number  $\Omega_{max}$ . The numerical tests are carried out for  $^{22}\text{O}$ . This neutron-rich isotope has an  $N/Z$  ratio of 1.75 and is close to the experimentally confirmed dripline nucleus  $^{24}\text{O}$ .

##### 6.1.1 Energy cutoff

The numerical solution of the HFB equations on a 2-D lattice results in a set of quasiparticle wavefunctions and energies. The quasiparticle energy spectrum contains both bound and (discretized) continuum states. The number of eigenstates is determined by the dimensionality of the discrete HFB Hamiltonian, which is  $N = (4 \cdot N_r \cdot N_z)^2$ , for fixed isospin projection  $q$  and angular momentum projection  $\Omega$ . Typically, quasiparticle energies up to



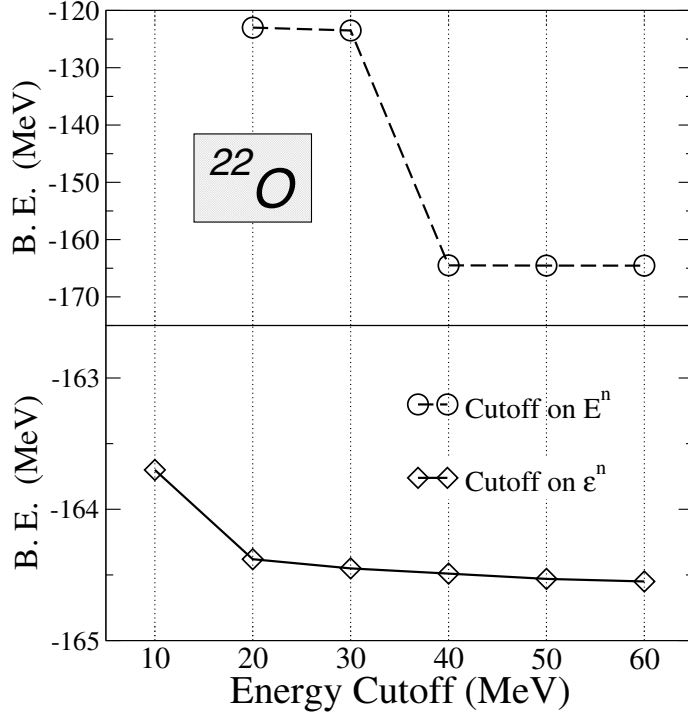


Figure 15: Binding energy of  $^{22}\text{O}$  vs. energy cutoff. Top: cutoff in the quasiparticle spectrum, bottom: cutoff in the equivalent single particle spectrum. All calculations were performed with B-Spline order  $M = 7$ ,  $N_r = 18$  lattice points, angular momentum projection  $\Omega_{max} = \frac{5}{2}$  and box size  $R = 10fm$ .

about 1 GeV are obtained in the calculations. It is well-known that zero-range pairing forces require a limited configuration space in the  $p - p$  channel because the interaction matrix elements decrease too slowly with excitation energy [6]. One therefore introduces an energy cutoff, either in the quasiparticle energy ( $E_{max}$ ) or in the equivalent single particle energy ( $\mathcal{E}_{max}$ ). Hence, in the case of zero-range pairing forces the infinite summations over quasiparticle energies in the expressions for the densities  $\rho$ ,  $\tau$ , and current  $J$  are terminated at a maximum quasiparticle energy.

The quantity  $E_{max}$  has to be chosen such that the maximum quasiparticle energy exceeds the depth of the mean field nuclear potential, and all of the bound states have to be included in the sums [5]. The prescription of Refs. [5, 20] is followed to set the cutoff energy in terms of the equivalent single particle energy spectrum,  $\mathcal{E}_n$ . A pairing strength of  $V_0 = -170MeV fm^3$

is utilized in these calculations, as previously explained on Chapter II.

Even though  $\mathcal{E}_{max}$  is a fixed parameter in the HFB calculations, it is interesting to analyze the sensitivity of observables to the value of the energy cutoff. Fig. 15 shows the plots of the total nuclear binding energy for cutoff values of  $\mathcal{E}_{max}$  between 10 and 60 MeV and the same for  $E_{max}$  from 20 to 60 MeV. It can be found in both cases that the binding energy remains essentially constant for cutoff values of 40 MeV and above. Clearly, a cutoff below 40 MeV results in significant changes in the binding energy because quasiparticle levels with large occupation probabilities are left out. This result is in agreement with the 1-D radial calculations of Ref.[6].

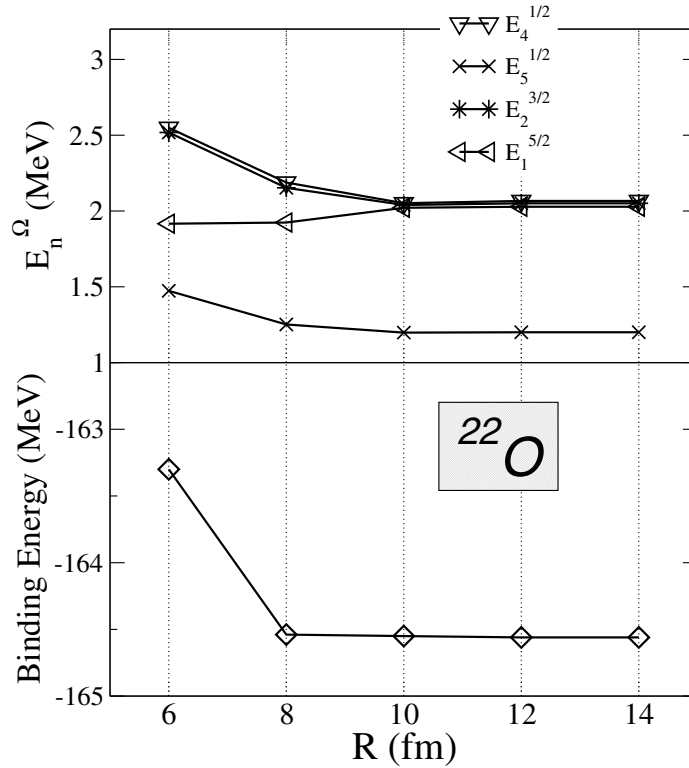


Figure 16: Bottom: Total binding energy of  $^{22}\text{O}$  as a function of the box size  $R$ . Top: Quasiparticle energies for states with large occupation probability ( $N_n$ ) as a function of  $R$ . The spline order used was  $M = 9$ ,  $N_r = 19$  grid points,  $\Omega_{max} = \frac{9}{2}$ , and cutoff energy  $\mathcal{E}_{max} = 60$  MeV.

### 6.1.2 Lattice box size

When using cylindrical coordinates, the lattice box size  $R$  defines the boundary in radial ( $r$ ) direction; the box size in  $z$  direction is  $2R$ . The value of  $R$  must be chosen large enough for the wavefunctions to vanish at the outer edges of the box and needs to be adjusted for optimal accuracy and computing time. Figure 16 shows the dependence of the binding energy on  $R$  for  $^{22}\text{O}$ . The maximum mesh spacing (the meaning of this concept has already been explained on Chapter IV) was kept at a constant value of  $\Delta r \approx 1\text{fm}$ . Figure 16 also presents some of the quasiparticle energy levels  $E_n^\Omega$  with large occupation probability  $N_n$ ; these levels correspond to low-lying states in the equivalent single-particle spectrum. Evidently, the quasiparticle energies and the total binding energy converge in essentially the same way with increasing box size. Figure 16 shows that convergence is reached at  $R=10$  fm. The behavior of the quasiparticle states with respect to the mesh boundaries has also been discussed in Ref. [6]. For heavier systems, the box size has to be increased. A safe initial guess for  $R$  is about three times the classical nuclear radius:

$$R = 3 \times 1.2A^{\frac{1}{3}} \text{ fm} \quad (140)$$

Tests also show that one may utilize the same mesh spacing for both light and heavy nuclei.

### 6.1.3 Number of mesh points

One of the major advantages of the B-Spline technique is that one can utilize a relatively coarse grid that results in a lattice Hamiltonian matrix of low dimensions. Figure 17 shows several observables as a function of the number of radial mesh points, for a fixed box size  $R = 8$  fm. The binding energy, neutron Fermi level, and pairing gap for  $^{22}\text{O}$  reach their asymptotic values at about 18 grid points in radial direction. For the fixed  $(r, z)$  boundary conditions utilized in our work, the B-Spline lattice points show a non-linear distribution, with more points in the vicinity of the boundaries, as explained on Chapter IV. In the central region, the grid spacing for 18 radial points is 0.75 fm.

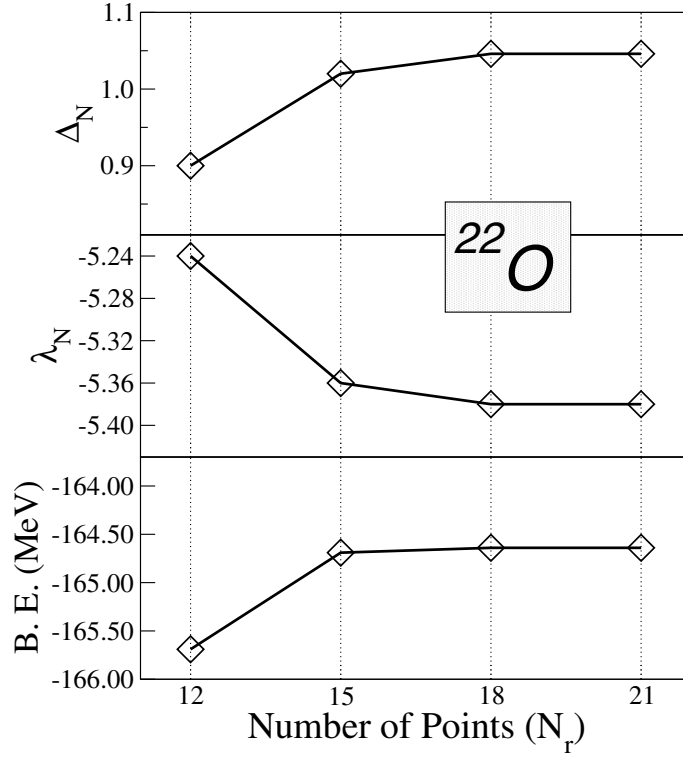


Figure 17: Total binding energy, Fermi level and pairing gap for neutrons in  $^{22}\text{O}$  vs. number of mesh points in radial direction, for fixed box size  $R = 10$  fm. The quantities  $\Omega_{max}$  and  $\mathcal{E}_{max}$  are the same as in Fig. 2

#### 6.1.4 Projection of the angular momentum, $\Omega$

It has been mentioned in the formalism section that all observables can be expressed by sums over *positive*  $j_z$  quantum numbers  $\Omega > 0$ . The maximum value  $\Omega_{max}$  increases, in general, with the number of protons and neutrons ( $Z, N$ ) and also depends on the nuclear deformation. There is no *a priori* criterion to fix  $\Omega_{max}$ ; this numerical parameter needs to be determined from test calculations in various mass regions. There have been performed calculations for  $^{22}\text{O}$  using  $\Omega_{max}$  values from  $5/2$  to  $13/2$ . Figure 18 displays the results for the total binding energy, neutron Fermi energy and neutron pairing gap. All three observables converge at  $\Omega = 9/2$ , with commensurate differences beyond this number.

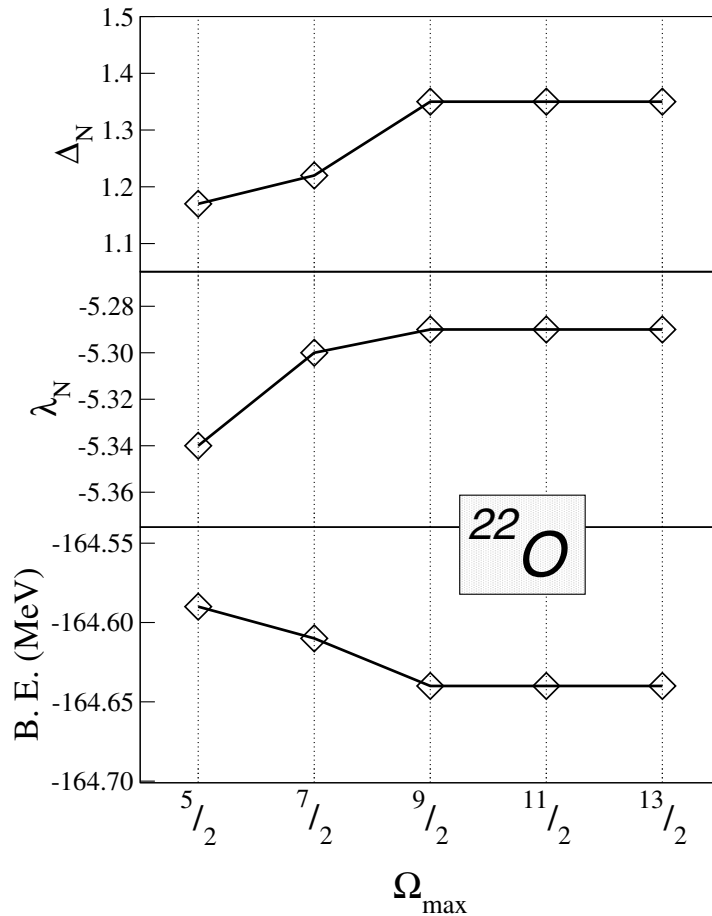


Figure 18: Binding energy, neutron Fermi level, and average neutron pairing gap for  $^{22}\text{O}$  vs. maximum angular momentum projection  $\Omega_{\max}$ . Box size  $R = 10$  fm,  $N_r = 18$  and an energy cutoff of 60 MeV were used.

## 6.2 Tests of Axially symmetric HFB results.

Converged numerical results of the axially symmetric HFB (2-D HFB) code are presented in this section. The goal is to demonstrate the accuracy of the Basis-Spline expansion technique on a two-dimensional coordinate lattice by comparison with the one-dimensional coordinate space results of Dobaczewski et al. [6, 34] for spherical nuclei (1-D HFB). For this purpose, a light, neutron-rich spherical nucleus has been chosen:  $^{22}\text{O}$ , with  $N/Z = 1.75$  and a heavy system,  $^{150}\text{Sn}$ , with  $N/Z = 2.0$ . Finally, it will be presented results for a strongly deformed medium-heavy system,  $^{102}\text{Zr}$  with  $N/Z = 1.55$ . This system was chosen because it allows us to compare the results of this work (which treat the continuum states accurately) to the two-dimensional “transformed harmonic oscillator” (2-D HFB+THO) expansion technique recently developed by Stoitsov et al. [20]. In this framework, a local-scaling point

transformation of the spherical harmonic oscillator is used to expand the quasiparticle wavefunctions in a set of bound single-particle wavefunctions.

Table 4: Calculations for  $^{22}\text{O}$  for HFB+SLy4. The axially symmetric calculations (2D HFB) of this work used a box size  $R = 10\text{fm}$  with maximum  $\Omega = \frac{9}{2}$  and an energy cutoff of 60 MeV. The spherical calculation of Ref. [34] was made with  $R = 25\text{fm}$  and a  $j = \frac{21}{2}$ . All calculations were made with a cutoff of 60 MeV.

	1-D HFB [34]	2-D HFB+THO[56]	2-D HFB(this work)
B. E. (MeV)	-164.60	-164.52	-164.64
$\lambda_n$ (MeV)	-5.26	-5.27	-5.29
$\lambda_p$ (MeV)	-18.88	-18.85	-18.16
$\Delta_n$ (MeV)	1.42	1.41	1.36
$\Delta_p$ (MeV)	0.00	0.00	0.00
$R_{rms}$ (fm)	2.92	2.92	2.92
$\beta_2$	*	0.00002	0.0007

### 6.2.1 Light, spherical nucleus $^{22}\text{O}$

In Table 4 the 2-D HFB results for the spherical isotope  $^{22}\text{O}$  are compared to the ones with the 1-D radial HFB method of Ref.[5]. Corresponding HFB results in the 2-D THO basis with 20 oscillator shells are also given. All calculations were performed with the Skyrme SLy4 force in the p-h channel and a pure delta interaction (pairing strength  $V_0 = -170\text{MeV fm}^3$ ) in the p-p channel, corresponding to volume pairing. The table lists several observables: the total binding energy (for comparison, the experimental value is  $-162.03\text{MeV}$ ), the Fermi level for protons and neutrons, the neutron energy gap (for protons, the gap is exactly zero in all three calculations), the *rms* radius, and the quadrupole deformation (note that both 2-D calculations predict essentially zero deformation). Overall, the results of the axially symmetric code of the present work agree with the other two calculations in all the observables. The binding energy predicted by our 2D-lattice code is very close (within 40 keV) to the 1-D lattice result, while the THO method result differs by 80 keV. This larger discrepancy might be related to the proximity of the oxygen isotope to the neutron dripline, where the

HFB calculations in coordinate representation are expected to work better.

Table 5: Comparison of calculations *HFB + SLy4* for  $^{102}\text{Zr}$  with two different methods in the axial symmetry. The configurational space calculations (THO) were made by Ref. [56] with 20 oscillator shells and pairing strength of  $-187.10 \text{ MeV fm}^3$ . Calculations by the coordinate space HFB 2-D code were made using a box size  $R = 12 \text{ fm}$  with  $N_r = 19$ , maximum  $\Omega = \frac{11}{2}$ ,  $V_0 -170 \text{ MeV fm}^3$  and the energy cutoff of  $60 \text{ MeV}$ .

	Exp.	2-D HFB+THO	2-D HFB(this work)
B. E. (MeV)	-863.7	-859.40	-861.10
$\lambda_n$ (MeV)		-5.42	-5.49
$\lambda_p$ (MeV)		-12.10	-12.00
$\Delta_n$ (MeV)		0.56	0.27
$\Delta_p$ (MeV)		0.62	0.36
$R_{rms}$ (fm)		4.58	4.58
$\beta_2$	0.5	0.429	0.430

### 6.2.2 Deformed neutron-rich nucleus: $^{102}\text{Zr}$

As stated before, the main motivation for developing an axially symmetric code is to perform highly accurate calculations for deformed nuclei, including the continuum states. The zirconium isotope  $^{102}\text{Zr}$  is a heavy nucleus with strong prolate quadrupole deformation in its ground state (see Figure 19). Its neutron to proton ratio of  $N/Z = 1.55$  places it into the neutron-rich domain although it is likely far away from the neutron dripline (in the 1-D spherical HFB+SkP approximation [33] the last bound nucleus in the chain is predicted to be  $^{136}\text{Zr}$ ). This zirconium isotope has been chosen primarily because the results can be compared to the stretched harmonic oscillator expansion (THO) method mentioned above which does not involve any continuum states.

Table 5 presents the results of the 2-D HFB calculations in coordinate space with the results obtained by the 2-D HFB+THO method. A comparison of the total binding energy of the system in both methods shows a difference of less than 1 MeV which can be considered small in comparison to the absolute value of the energy (as seen in Table 5, the experimen-

tal binding energy value is  $-863.7$  MeV). The pairing strength parameter,  $V_0$ , used in each calculation also makes a difference. Other observables (Fermi levels, rms-radius and deformation  $\beta_2$ ) agree quite well, also. However, substantial differences are found in the energy gap values ( $\Delta_n, \Delta_p$ ); these may be attributed to the different density of states used in the two methods (see Eq. (54)).

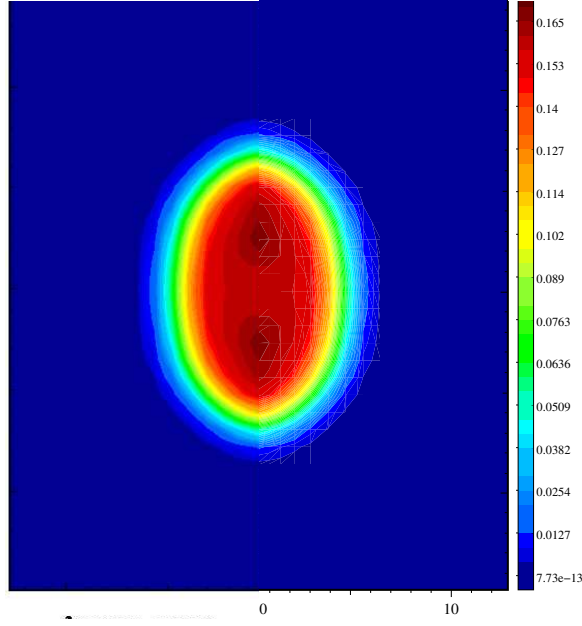


Figure 19:  $^{102}\text{Zr}$  total mass density. The density scale according to the color intensity is shown on the right. The distance (fm) is labeled at the bottom for the radial direction. This nucleus shows strong prolate deformation.

### 6.2.3 Heavy nucleus $^{150}\text{Sn}$

Next, the results for  $^{150}\text{Sn}$  are presented. This tin isotope is a heavy nucleus far away from the valley of  $\beta$ -stability and it is located close to the two-neutron drip-line. Table 6 shows the comparison of the 2-D HFB results [57, 58] with the radial 1-D HFB calculations of Refs. [6, 34]. The 2-D calculations predict a very small quadrupole deformation  $\beta_2 = 0.005$  (almost a spherical shape), which allowed the comparison of the 2-D HFB results with those



done using the 1-D HFB code.

One difference between these two calculations is the box size used. In the axially symmetric calculations it was 20 fm in  $r$  direction and 40 fm in the  $z$  axis, whereas the 1-D code had a 30 fm radial box. Also, the density of points has a different meaning in the radial code, since it uses a different grid than the one used in the B-Splines technique for our 2-D code. For these calculations the resulting mesh spacing in the 1-D code was 0.25 fm, whereas the maximum mesh spacing in the 2-D one was 1.1 fm. In the 2-D calculations an approximately  $3000 \times 3000$  matrix was diagonalized for each  $\Omega$  and isospin value, and for each major HFB iteration. The full calculation required about 30 HFB iterations.

Table 6: Comparison of calculations for spherical nucleus  $^{150}\text{Sn}$ . The Skyrme force used is SLy4. The 1-D calculations were made by Ref. [34], using a box size  $R = 30$  and a linear spacing of points of 0.25 fm, with  $j_{max}$  of  $\frac{21}{2}$ . Calculations by the 2-D HFB code were made using a box size  $R = 20\text{fm}$  with  $N_r = 23$ , maximum  $\Omega = \frac{13}{2}$ . In both calculations the pairing strength  $V_0$  was set to  $-170\text{ MeV fm}^3$ , and the energy cutoff to  $60\text{ MeV}$ .

Observables	1-D HFB	2-D HFB
B. E. (MeV)	-1129	-1130
$\lambda_n$ (MeV)	-0.96	-0.94
$\lambda_p$ (MeV)	-17.54	-17.34
$\Delta_n$ (MeV)	1.02	0.97
$\Delta_p$ (MeV)	0.00	0.00
$R_{rms}$ (fm)	5.12	5.13
$\beta_2$	*	0.005

Like in the oxygen isotope case, the agreement is very good. However, even when both methods predict this nucleus to be spherical some small numerical discrepancies exist due to the different nature of each method. A possible source of such differences is the fact that the 2-D code yields  $\beta_2 = 0.005$  whereas the 1-D code assumes an exactly spherical shape.

Table 6 also contains another interesting piece of information on  $^{150}\text{Sn}$ : the neutron Fermi level  $\lambda_n$  in both HFB+SkM\* and HFB+SLy4 cases is located less than 1 MeV below the continuum which shows the proximity of this nucleus to the two-neutron dripline.

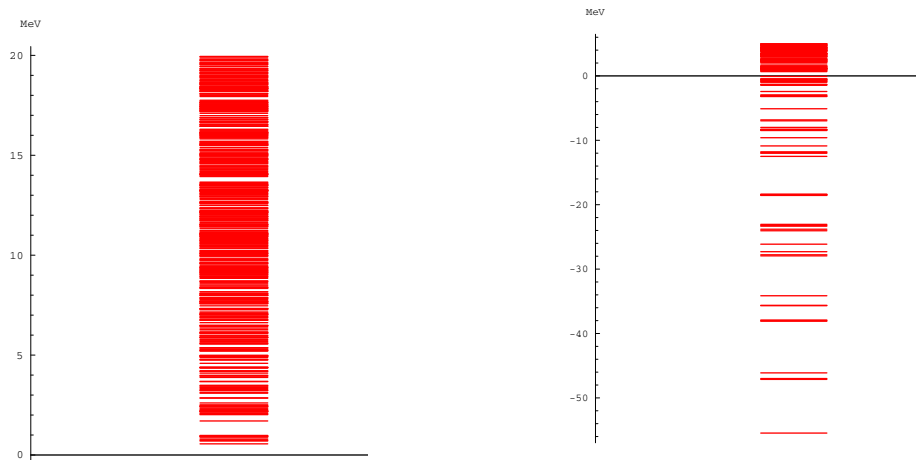


Figure 20: Quasiparticle energy spectrum of  $^{150}\text{Sn}$  for neutrons and equivalent single particle spectrum. The first one is shown up to an energy of 20 MeV. The second up to an equivalent single particle energy of 5 MeV. The  $\Omega$ 's are considered up to  $13/2$ .

### 6.3 Analysis of the quasiparticle spectrum in $^{150}\text{Sn}$

The results of the last section will be analyzed in the next sections, in terms of the quasiparticle spectrum and the corresponding wavefunctions. The equivalent single-particle spectrum of  $^{150}\text{Sn}$  is introduced in the first part of this section. The qualitative features of the wavefunctions are studied in the second part and the differences between bound and continuum states will be shown.

#### 6.3.1 Quasiparticle states in $^{150}\text{Sn}$

The left side of Fig. 20 shows the quasiparticle spectrum of  $^{150}\text{Sn}$  for  $HFB + SLy4$ . The lowest four states correspond to the discrete part of the spectrum, since they are below the Fermi level ( $\lambda = 0.88\text{MeV}$ ). The rest is shown up to 20 MeV. It is the continuum part, but because of the numerical discretization it looks like a very dense discrete spectrum. On the right side of Fig. 20 is the equivalent single particle spectrum, closely related to the quasiparticle spectrum by means of the relation in Eq. (139). Now the equivalent

single particle spectrum looks more familiar, with the lowest state close to the bottom of the attractive part of the nuclear potential. Above the Fermi level ( $\approx -1 \text{ MeV}$ ) it can be observed an expected high density of levels that correspond to the continuum ( $E > 0$ ). The Fermi level itself is close to zero, characteristic of the nuclear systems near the driplines (in this case, the neutron dripline).

### 6.3.2 $^{150}\text{Sn}$ wavefunctions

We can investigate some properties of the wavefunctions corresponding to  $^{150}\text{Sn}$  states. Fig. 21 shows wavefunctions for selected states. This figure shows only the predominant spinor wavefunctions for each state. It is shown also the equivalent single particle energy ( $\varepsilon_n$ ) and occupation ( $N_n$ ) for each state. The wavefunctions are accommodated and numbered according to the quasiparticle energy (from top to bottom the quasiparticle energies are decreasing, as in the spectrum on Fig. 20). If we look at the negative equivalent single-particle states (all except number 350), they show an increasing number of nodes as they become more negative, since they belong to bound states. These states have a higher occupancy, mainly in those of most negative s.p. energies. The wavefunctions corresponding to positive single-particle energy states, on the other hand (no. 350), show a strong oscillatory behavior. This is expected, since they are part of the continuum. Other states close to the Fermi level, have a similar amplitude in all four of their spinor wavefunctions, like the no. 3. This kind of states contribute the most to the pairing density and pairing energy.

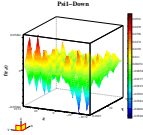
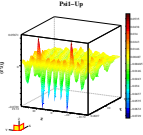
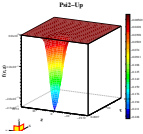
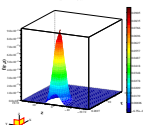
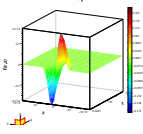
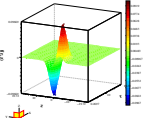
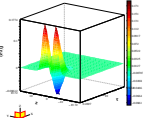
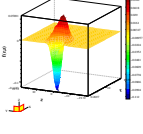
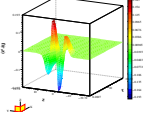
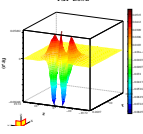
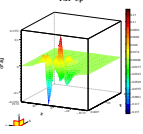
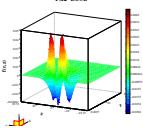
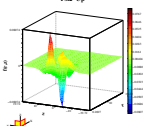
No	Q.P.E. (MeV)	S.P.E. (MeV)	$N_n$	$\phi_1(\uparrow)$	$\phi_1(\downarrow)$	$\phi_2(\uparrow)$	$\phi_2(\downarrow)$
350	60.0	59.1	0.000				
316	54.5	-55.4	0.999				
269	46.2	-47.0	0.998				
124	22.2	-23.0	0.997				
10	2.42	-2.95	0.917				
3	0.86	-0.47	0.237				

Figure 21: Wavefunctions corresponding to selected neutron states with  $\Omega = 1/2$  in  $^{150}\text{Sn}$ . They are shown according to descending quasi-particle energy. Corresponding equivalent single-particle energies and occupation  $N_n$  are also displayed. The states with negative single-particle energies show the typical behavior of bound states. High-continuum states show an expected oscillatory behavior. The states close to the Fermi level (like the bottom one) contribute the most to the pairing energy.

## 6.4 Calculations in the sulfur isotope chain

This section presents a series of systematic calculations on the sulfur isotope chain. The selection of these nuclei was based in previous predictions and calculations [59, 33]. The properties of the neutron-rich sulfur chain will be analyzed and the last bound even nucleus in the chain will be determined by computing the two-neutron separation energies.

The summary of the axially symmetric  $HFB + Sly4$  calculations is shown in Table 7. The values for the Fermi level ( $\lambda$ ), the pairing gap ( $\Delta$ ), deformation parameter  $\beta_2$  and the binding energies are shown. These kind of calculations are not to be confronted with the experimental values, since they depend on the force utilized to emulate the nucleon-nucleon interaction. However, the experimental binding energies are included for reference purposes only. The calculations in Table 7 were only performed over those isotopes close to the neutron dripline.

Table 7: Calculations for  $S$  isotopes from  $A=42$  to  $A=52$ . In the calculations  $R$  varied from 12 fm ( $S^{44}$ ) to 13 fm ( $S^{52}$ ) in each direction. The maximum grid spacing was 1 fm, spline order of 7 and  $\Omega_{max}(n) = 9/2$ ,  $\Omega_{max}(p) = 7/2$ . Experimental data for even-even nuclei is available up to  $S^{48}$  [2].

Isotope	$R_{rms}$ (fm)	$\lambda_n$ (MeV)	$\Delta_n$ (MeV)	$\beta_2$	B. E. (MeV) <i>HFB + Sly4</i>	B. E. (MeV) Exp
$S^{42}$	3.44	-5.33	0.84	-0.09	-342.5	-343.72
$S^{44}$	3.48	-4.13	0.09	-0.06	-352.0	-353.50
$S^{46}$	3.58	-3.05	0.10	-0.11	-358.3	-359.16
$S^{48}$	3.66	-2.18	0.05	-0.04	-363.0	-362.80
$S^{50}$	3.77	-0.77	0.05	-0.01	-365.3	N/A
$S^{52}$	3.83	0.10	0.90	-0.05	-365.2	N/A

### 6.4.1 Sulfur dripline

The exact location of the driplines has been measured experimentally only for some nuclei. On the proton rich side it has been determined up to  $Z=83$ . On the neutron rich

side, however, the dripline has been measured only for the lightest nuclei (up to  $N=8$ ). Theoretically, predicted driplines are strongly model dependent. The estimation of the dripline is based in the difference in masses between adjacent nuclei, rather than in the value of the masses themselves. The study of the driplines is based then, on the *separation energies*. The definition of the two-neutron separation energy is giving by

$$S_{2n}(Z, N) = B(Z, N) - B(Z, N + 2), \quad (141)$$

where  $B(Z, N)$  is the ground state energy of the nucleus with separation energy  $S_{2n}(Z, N)$ , and  $B(Z, N + 2)$  the ground state energy of the neighboring even isotope.

### Sulfur two-neutron separation energies

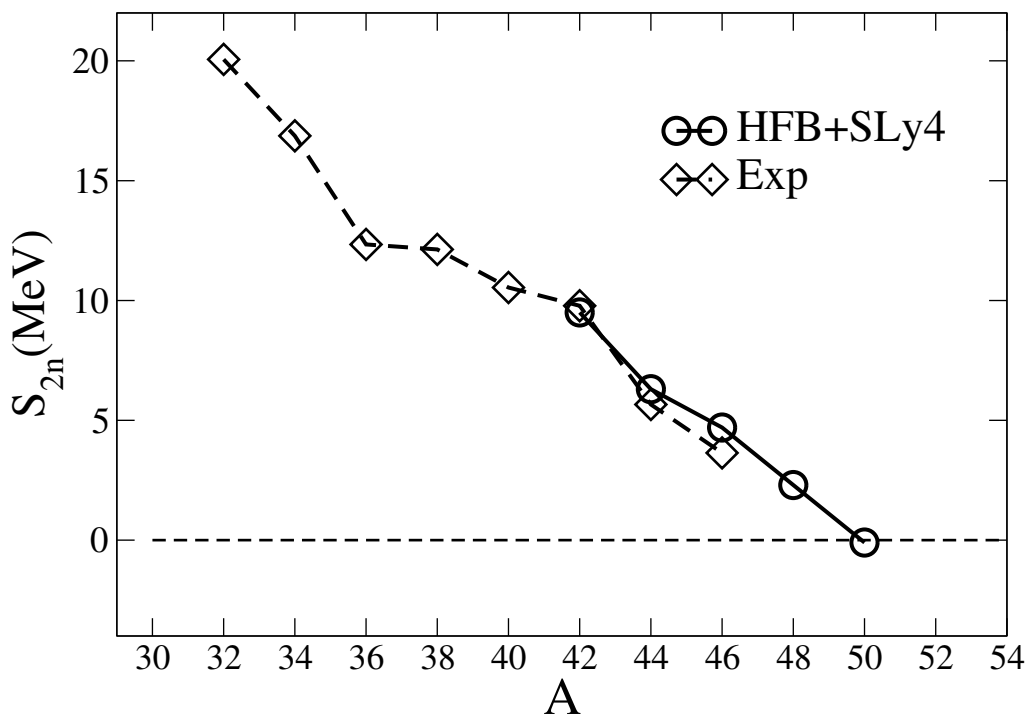


Figure 22: Two-neutron separation energies for sulfur isotopes. The dripline is located where the separation energy becomes zero.

The determination of the two-neutron dripline is given by the vanishing two-neutron separation energy

$$S_{2n}(Z, N) = 0 \quad (142)$$

The ability to calculate the nuclei over the dripline regions is possible only by making use of a theory that handles the continuum properly. It has been concluded previously that full HFB methods resolve this difficulty arising from continuum states. In the present section it will be determined the two-neutron drip line in the Hartree-Fock-Bogoliubov framework with Skyrme interaction. This study will be performed over the sulfur chain of even isotopes.

Figure 22 shows the two-neutron separation energies corresponding to the sulfur isotopes in Table 7. The separation energies from  $^{32}S$  to  $^{52}S$  based on the experimental binding energies are also shown in Fig. 22.

The calculated separation energies shown in Fig. 22 cannot be used for comparison with the experimental values at the vanishing separation energy point because of the unavailable experimental data beyond  $^{48}S$ . In Fig. 22 the *HFB + SLy4* calculations have the same overall tendency to the vanishing dripline as the experimental data. The last bound nucleus in the sulfur chain is  $^{48}S$  according to the calculations and the experimental values. This result disagrees with the one calculated with the spherical *HFB + SkP\** model [5, 6, 33], which predicts  $^{52}S$  to be last nucleus located just inside the two-neutron dripline in the sulfur isotope chain. The *HF + SIII* model [59] uses a constant gap approximation with  $\Delta_n = \Delta_p = 75keV$  for the same calculation. In this model the nucleus  $^{52}S$  is already unstable. The relativistic mean field (RMF) [59] calculation predicts  $^{54}S$  to be inside the dripline. This shows again, that the separation energies are sensitive to the method and force utilized and so is the dripline.

The calculated Fermi energies for *HFB+SLy4* shown in Fig. 23 confirm another expected feature of nuclei approaching the driplines. The neutron Fermi level for each isotope gets smaller with increasing number of neutrons. When the dripline is crossed then  $\lambda$  becomes positive, which means that the coupling to the continuum is predominant, making the nucleus totally unbound. Even though isotope  $^{50}S$  still shows a negative Fermi level, it corresponds to the unbound nuclei according to the two-neutron separation energies in Fig. 22.

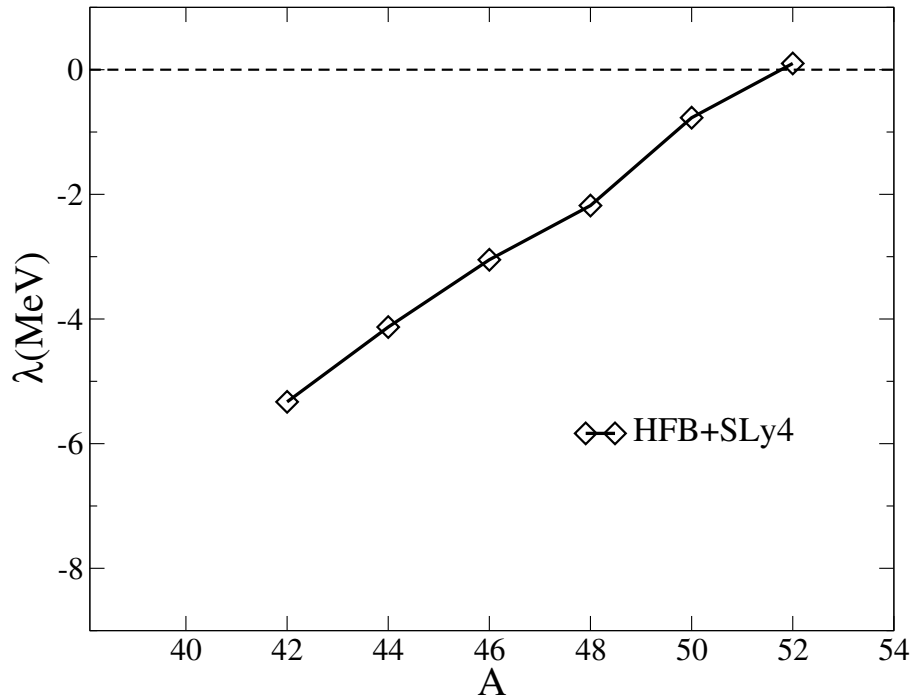


Figure 23: Fermi level for Sulfur isotopes. As the neutron number increases, it gets closer to zero until it goes positive past the dripline, at  $^{50}\text{S}$ .

#### 6.4.2 Skins and Halos

One of the most interesting phenomena for nuclei far from stability is the increase in their radial dimension with decreasing particle separation energy [60]. In light neutron rich nuclei near the neutron dripline, protons and neutrons are decoupled and the extra neutrons form a layer on the surface of such nuclei called a *neutron skin*. The neutron skin is observed as an excess of neutrons at large distances, greater than the radius of the proton distribution. In heavier nuclei near the neutron drip line, some of the neutrons diffuse out from the nucleus and form an extremely thin cloud called a neutron halo. A halo nucleus has loosely bound few-nucleon systems with considerably more neutrons than protons. In neutron-rich weakly bound nuclei one expects to find both the skin and the halo.

There is no definite way to quantify and parameterize the skins and halos. Some people use the difference in the root mean square (rms) radius to characterize the spatial extension of the neutron density



$$\Delta R_{np} = \langle r_n^2 \rangle - \langle r_p^2 \rangle, \quad (143)$$

with

$$R_{rms} = \sqrt{\langle r^2 \rangle} = \sqrt{\frac{\int d^3\mathbf{r} r^2 \rho(\mathbf{r})}{\int d^3\mathbf{r} \rho(\mathbf{r})}} \quad (144)$$

$$= \sqrt{\frac{\int d^3\mathbf{r} r^2 \rho(\mathbf{r})}{A}}. \quad (145)$$

If one wants to calculate the  $R_{rms}$  for neutrons or protons only, the number of nucleons,  $A$ , has to be substituted by  $N$ , or  $Z$ , and the total density  $\rho$  by  $\rho_n$  or  $\rho_p$ .

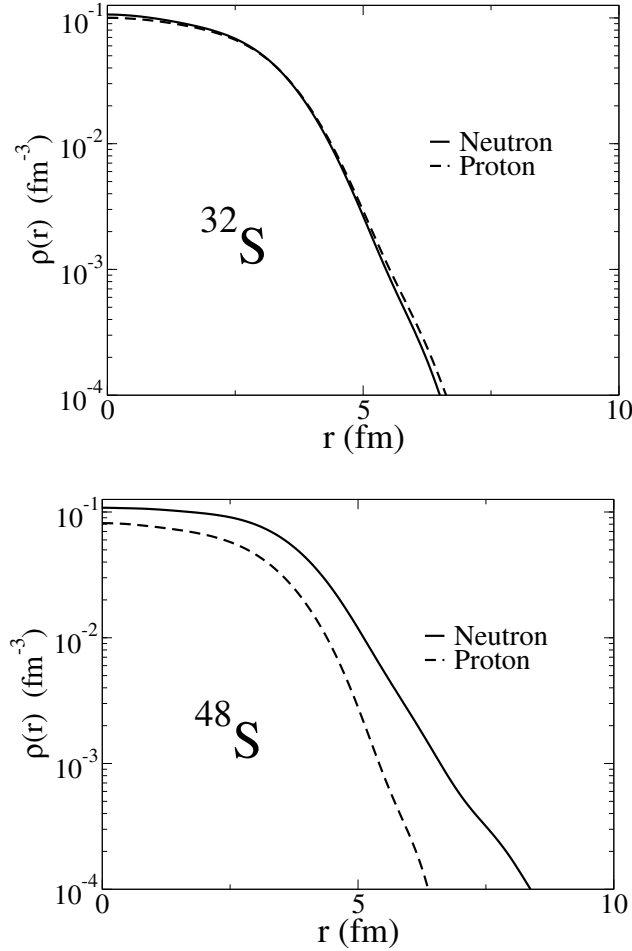


Figure 24: Neutron and proton radial densities of sulfur isotopes  $^{32}\text{S}$  and  $^{48}\text{S}$ . The stable one ( $^{32}\text{S}$ ) shows practically no difference in its densities. Dripline nucleus  $^{48}\text{S}$  shows densities differences typical of a nucleus with a nuclear halo.

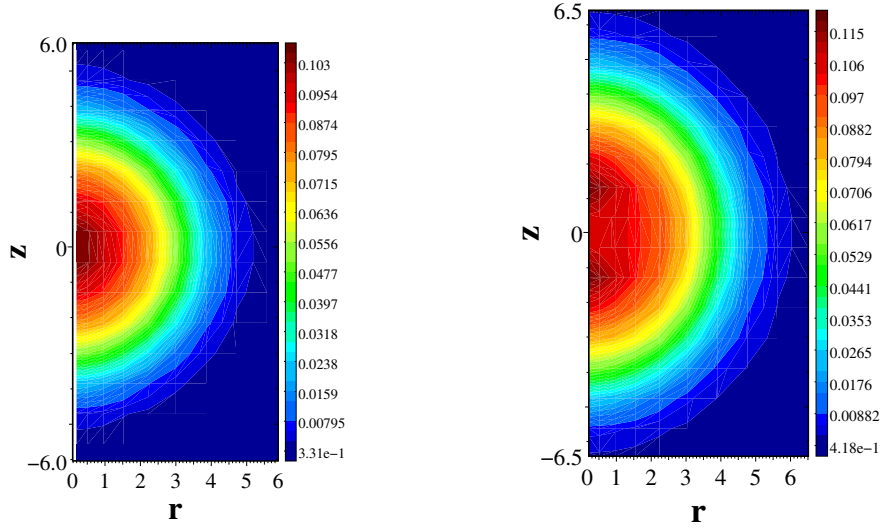


Figure 25: Neutron densities corresponding to sulfur isotopes in Fig. 24. It can be observed the nearly spherical shape of the neutron distribution in both cases. The neutrons in  $^{48}\text{S}$  are significantly more spread out than the one in  $^{32}\text{S}$ .

To illustrate the halos and skins in nuclei, the sulfur isotopes calculations of Table 7 will be used. Figure 24 shows plots of the neutron and proton densities vs. radius for sulfur isotopes  $^{32}\text{S}$  and  $^{48}\text{S}$ . The variable  $r$  stands for the radial coordinate when  $z = 0$ . Even when this calculations are for axial symmetry, we can safely use one-dimensional plots for the case of sulfur isotopes, given their nearly-spherical shape (for the plots shown in Fig.24 the corresponding deformation are  $\beta = 0.06, 0.01$ ). The first plot in Fig. 24 corresponds to the stable  $^{32}\text{S}$ . The other,  $^{48}\text{S}$ , is located right inside the sulfur dripline point, according to the study of the last section. The proton and neutron densities are shown in each graph. The logarithmic scale is used in these plots to enhance the difference between proton and neutron densities. For stable nuclei the spatial distribution of the neutron and proton densities is almost indistinguishable, as seen in Fig. 24 for  $^{32}\text{S}$ . On the other hand, the  $^{48}\text{S}$  plot shows a very noticeable difference between neutron and proton distribution. An increasing difference of up to 5 fm is observed. This a typical feature corresponding to a neutron halo.

## CHAPTER VII

### CONCLUSIONS

The axial symmetry imposed on the Hartree-Fock-Bogoliubov calculations of this thesis is expected to be well suited in describing the ground states of most of the deformed nuclei far from stability. The HFB approach for such nuclei works especially well in treating strong coupling to the continuum, which has been shown to be crucial for obtaining convergence. Undoubtedly the most valuable contribution of this work has been the development of the axial HFB code with quasiparticle energies up to 60 MeV. Previous models of HFB calculations have described nuclei by either imposing spherical symmetry or reaching only up to a limited quasiparticle energy. In this sense, the axial HFB is an innovation to the existing codes in nuclear structure theory, and therefore, highly attractive for applications in even-even nuclei.

The  $^{22}\text{O}$  calculations shown are a noticeable indication of the convergence and accuracy of the 2-D HFB code with increasing box size, cutoff energy and grid spacing. The study of these parameters allowed us to conclude the suitable criteria for calculating heavier nuclei.

It was shown also that calculations made with the axially symmetric HFB computations agree with radial HFB calculations for spherical nuclei. The great agreement shown for  $^{150}\text{Sn}$  calculations was definitely the most important test for demonstrating that the 2-D axially symmetric code can reproduce the results of the widely accepted 1-D HFB calculations.

The prediction of dripline-nuclei was demonstrated through the calculations of several sulfur isotopes. The corresponding two-neutron separation energies in these nuclei defined  $^{48}\text{S}$  to be right on the two-neutron drip-line for the  $S$  chain. The quality of neutron skins in nuclei was also illustrated with the calculations of the  $S$  isotopes.

All these results are highly encouraging and could be the starting point for future efforts in making the axially symmetric code more practical and efficient. With a sufficiently fast code we could elaborate massive calculations that would enable us to compute the drip lines for a wide range of light and heavy nuclei, for instance.

## 7.1 Possible future work

The HFB code is able to make use of a few Skyrme parameterizations, namely,  $SkM^*$  and  $SLy4$ . According to Eq. (92) from Chapter III, the lack of the terms corresponding to  $\Theta = 1$  restricts the calculations to these two forces only. If one wants to be able to use more forces from Table 2, the current  $j_q$  has to be included. This requires the suitable representation of  $j_q$  in the symmetry represented here. Once this is accomplished, more forces like  $SkP$  and  $SkO$  can be used, and more results can be compared to previous work with these forces by other authors.

As already mentioned, the present diagonalization method for the HFB calculations consumes too much computing time. Currently there is no other way to accomplish the solution of the HFB equations in coordinate space by other numerical method, at least for the axial symmetry presented in this work. This restriction only permits to perform calculations over limited box sizes and density of points. As it is, the HFB code can only be used to perform calculations with grid spacing greater than 0.75 fm. This means that a maximum box size of 25 fm can be achieved, enough for a nucleus like  $^{150}Sn$  but not for a heavier one. One possible alternative to the full diagonalization is the application of the damped relaxation method described on Refs. [61, 62]. In this approach, the wavefunctions are calculated as

$$\Psi_\lambda^{k+1} = O[\Psi_\lambda^k - x_0 D(E_0)(h^k - \epsilon_\lambda^k)\Psi_\lambda^k] , \quad (146)$$

where  $D(E_0)$  is the damping operator and  $O$  is the Gram-Schmidt orthonormalization of the whole set of eigenfunctions, with the Hamiltonian  $h^k$  and eigenenergies  $\epsilon_\lambda^k$ . Since the damping operator  $D(E_0)$  has to be constructed with all the set of energies, this can be inconvenient for the case of HFB problem. In principle, the HFB energy spectrum is infinite from both extremes and this is the dilemma for applying the damping method in HFB. However, if one successfully comes up with a damping operator suitable for the HFB quasiparticle spectrum, the new code could be run substantially faster.

Finally, we have to keep in mind the restrictions due to the nature of the HFB theory. The work developed here is currently limited to calculations of properties in even-even nuclei because of the initial assumption of the total angular momentum in nuclei to be zero. Therefore, some work could be done to allow the 2-D HFB code to perform calculations on

odd-even, given that these nuclei represent 1-quasiparticle excitations in the HFB formalism [22].

## APPENDIX A

### ALTERNATIVE DIAGONALIZATION: SYMMETRIC EIGENVALUE PROBLEM

The diagonalization of a symmetric matrix is computationally less expensive and we can take advantage of this by rearranging the eigenvalue problem of Eqs. (116). We want to represent operator  $O$  that operates over the exact function  $\bar{f}$

$$O(r, z)\bar{f}(r, z) = \bar{g}(r, z) . \quad (147)$$

For now we will assume that the operator is a sum of two independent operators acting on different coordinates

$$O(r, z) = O(r) + O(z) . \quad (148)$$

Expand functions  $\bar{f}$  and  $\bar{g}$  in splines and substitute them in Eq. (147) using definition (114), only for  $r$  and  $z$  at the same time

$$\sum_{ij} \{O_r B_i(r) B_j(z) + B_i(r) O_z B_j(z)\} a^{ij} = \sum_{kl} B_k(r) B_l(z) b^{kl} . \quad (149)$$

Multiplying from left by

$$\int v(r) w(z) B_m(r) B_n(z) dr dz \quad (150)$$

results in

$$\sum_{ij} (O_{mi}^r G_{nj}^z + G_{mi}^r O_{nj}^z) a^{ij} = \sum_{kl} (G_{mk}^r G_{nl}^z) b^{kl} , \quad (151)$$

where  $O^r$ ,  $O^z$ ,  $G^r$  and  $G^z$  are given by

$$\begin{aligned} O_{mi}^r &= \sum_{ij} \int v(r) B_m(r) O_r B_i(r) dr \\ O_{nj}^z &= \sum_{ij} \int w(z) B_n(z) O_z B_j(z) dz \\ G_{nj}^z &= \sum_{ij} \int w(z) B_n(z) B_j(z) dz \\ G_{mi}^r &= \sum_{ij} \int v(r) B_m(r) B_i(r) dr , \end{aligned}$$

and coefficients  $a$  and  $b$  are given by inversion in terms of splines

$$a^{ij} = \sum_{\alpha\beta} \tilde{B}_r^{i\alpha} \tilde{B}_z^{j\beta} f_{\alpha\beta}$$

$$b^{kl} = \sum_{\alpha\beta} \tilde{B}_r^{k\alpha} \tilde{B}_z^{l\beta} g_{\alpha\beta} .$$

Substituting these coefficients in Eq. (151) we get in compact form

$$\sum_{ij\alpha\beta} (O_{mi}^r G_{nj}^z \tilde{B}_r^{i\alpha} \tilde{B}_z^{j\beta} + G_{mi}^r O_{nj}^z \tilde{B}_r^{i\alpha} \tilde{B}_z^{j\beta}) f_{\alpha\beta} = \sum_{ij\alpha\beta} G_{mi}^r G_{nj}^z \tilde{B}_r^{i\alpha} \tilde{B}_z^{j\beta} g_{\alpha\beta} . \quad (152)$$

Now multiply Eq.(152) from left by

$$\sum_{mn} G_z^{j'n} G_r^{i'm} \quad (153)$$

and use the Gram property (analog to the splines property)

$$\sum_b G^{a'b} G_{ba} = \delta_a^{a'} \quad (154)$$

to get

$$\sum_{im\alpha\beta} (G_r^{i'm} O_{mi}^r \tilde{B}_r^{i\alpha} \tilde{B}_z^{j'\beta} + \sum_{jn\alpha\beta} G_z^{j'n} O_{nj}^z \tilde{B}_r^{i'\alpha} \tilde{B}_z^{j\beta}) f_{\alpha\beta} = \sum_{\alpha\beta} \tilde{B}_r^{i'\alpha} \tilde{B}_z^{j'\beta} g_{\alpha\beta} \quad (155)$$

Finally, multiply by

$$\sum_{i'j'} \tilde{B}_{\beta'j'}^z \tilde{B}_{\alpha'i'}^r \quad (156)$$

to get

$$\sum_{\alpha} O_{\alpha'}^{\alpha}(r) f_{\alpha\beta'} + \sum_{\beta} O_{\beta'}^{\beta}(z) f_{\alpha\beta} = g_{\alpha'\beta'} \quad (157)$$

where

$$O_{\alpha'}^{\alpha}(r) = \sum_{i'i'm} \tilde{B}_{\alpha'i'}^r G_r^{i'm} O_{mi}^r \tilde{B}_r^{i\alpha} \quad (158)$$

$$O_{\beta'}^{\beta}(z) = \sum_{jj'n} \tilde{B}_{\beta'j'}^z G_z^{j'n} O_{nj}^z \tilde{B}_z^{j\beta} \quad (159)$$

This is the representation of operators  $O(r)$  and  $O(z)$  in the Galerkin scheme.

To get the representation in way suitable for using direct diagonalization, it is necessary to modify these equations. A convenient way to do so is to get symmetric forms of the matrices corresponding to the operators. Eq. (157) does not involve symmetric operators

yet. Starting from Eq.(152), substitute the function  $\bar{g}(r, z)$  using the eigenvalue problem definition

$$g_{\alpha\beta} = \lambda f_{\alpha\beta} , \quad (160)$$

and multiply by

$$\sum_{mn} \tilde{B}_r^{\gamma m} \tilde{B}_z^{\delta n} \quad (161)$$

to get

$$\begin{aligned} \sum_{ijmn\alpha\beta} (\tilde{B}_r^{\gamma m} \tilde{B}_z^{\delta n} O_{mi}^r G_{nj}^z \tilde{B}_r^{i\alpha} \tilde{B}_z^{j\beta} + \tilde{B}_r^{\gamma m} \tilde{B}_z^{\delta n} G_{mi}^r O_{nj}^z \tilde{B}_r^{i\alpha} \tilde{B}_z^{j\beta}) f_{\alpha\beta} \\ = \lambda \sum_{kl\alpha\beta} \tilde{B}_r^{\gamma m} \tilde{B}_z^{\delta n} G_{mi}^r G_{nj}^z \tilde{B}_r^{i\alpha} \tilde{B}_z^{j\beta} f_{\alpha\beta} \end{aligned} \quad (162)$$

Now, we will define

$$\begin{aligned} \mathcal{G}_z^{\delta\beta} &= \sum_{jn} \tilde{B}_z^{\delta n} G_{nj}^z \tilde{B}_z^{j\beta} \\ \mathcal{G}_r^{\gamma\alpha} &= \sum_{im} \tilde{B}_r^{\gamma m} G_{mi}^r \tilde{B}_r^{i\alpha} \\ \mathcal{O}_z^{\delta\beta} &= \sum_{jn} \tilde{B}_z^{\delta n} O_{nj}^z \tilde{B}_z^{j\beta} \\ \mathcal{O}_r^{\gamma\alpha} &= \sum_{im} \tilde{B}_r^{\gamma m} O_{mi}^r \tilde{B}_r^{i\alpha} \end{aligned}$$

Using this notation we get the expression that can be used for the direct diagonalization method that uses symmetric matrices on both sides:

$$\sum_{\alpha\beta} (\mathcal{G}_z^{\delta\beta} \mathcal{O}_r^{\gamma\alpha} + \mathcal{G}_r^{\gamma\alpha} \mathcal{O}_z^{\delta\beta}) f_{\alpha\beta} = \lambda \sum_{\alpha\beta} \mathcal{G}_r^{\gamma\alpha} \mathcal{G}_z^{\delta\beta} f_{\alpha\beta} . \quad (163)$$

This equation can be adapted to the form

$$AX_n = y_n BX_n , \quad (164)$$

X representing the eigenvector of the n-th eigenvalue,  $y_n$ ; and A and B being two symmetric matrices. This form of the eigenvalue problem is numerically faster to solve. Equation (164) was derived assuming that the operator was composed of two operators acting on  $r$  or  $z$  independently. The case of the operator being a mixture of both ( $O(r, z)$ ) has to be incorporated in the same scheme.



## APPENDIX B

### EXPECTATION VALUES OF ONE-BODY OPERATORS IN 2-D

Our goal is to calculate the expectation value of an arbitrary 1-body operator in the HFB ground state. In coordinate representation, the operator  $A$  is given by

$$A = \sum_{i=1}^N A(x_i) \quad (165)$$

where  $x_i = (\mathbf{r}_i, \sigma_i, q_i)$  denotes all degrees of freedom for nucleon  $i$ . In occupation number representation, the same operator has the form

$$\hat{A} = \int dx \hat{\psi}^\dagger(x) A(x) \hat{\psi}(x) \quad (166)$$

and the expectation value of  $A$  is given by

$$\begin{aligned} \langle A \rangle &= \int dx \langle \Phi_0 | \hat{\psi}^\dagger(x) A(x) \hat{\psi}(x) | \Phi_0 \rangle = \\ &= \int d^3r \sum_{\sigma} \sum_q \langle \Phi_0 | \hat{\psi}^\dagger(\mathbf{r}\sigma q) A(\mathbf{r}\sigma q) \hat{\psi}(\mathbf{r}\sigma q) | \Phi_0 \rangle \end{aligned} \quad (167)$$

Expanding the nucleon field operators in terms of single-particle basis states one finds

$$\langle A \rangle = \int d^3r \sum_{\sigma, q} \sum_{i, j} \rho_{i, j} \phi_j^*(\mathbf{r}\sigma q) A(\mathbf{r}\sigma q) \phi_i(\mathbf{r}\sigma q) \quad (168)$$

Inserting the expression for  $\rho_{i, j}$ , Eq.(34) we obtain

$$\langle A \rangle = \int d^3r \sum_{\sigma=\pm\frac{1}{2}} \sum_{q=\pm\frac{1}{2}} \sum_{\alpha} \phi_2^*(\alpha, \mathbf{r}\sigma q) A(\mathbf{r}\sigma q) \phi_2(\alpha, \mathbf{r}\sigma q) \quad (169)$$

This is the most general expression for the ground state expectation value of the 1-body observable  $A$ .

We now evaluate some specific observables. For the mean square mass radius, we have  $A(\mathbf{r}\sigma q) = \mathbf{r}^2 / (Z + N)$  which leads to

$$\langle r^2 \rangle = \frac{1}{A} \int d^3r \rho(\mathbf{r}) \mathbf{r}^2 \quad (170)$$

In the case of axially symmetry nuclei we find after transforming to cylindrical coordinates

$$\langle r^2 \rangle = \frac{1}{A} 2\pi \int_0^\infty r dr \int_{-\infty}^\infty dz \rho(r, z) (r^2 + z^2) \quad (171)$$

The root mean square mass radius is defined as the square root of this quantity, i.e.

$$r_{rms} = \sqrt{\langle r^2 \rangle} \quad (172)$$

The mean square charge radius can be obtained from the above expressions by the obvious substitutions  $A \rightarrow Z$  and  $\rho \rightarrow \rho_p$ .

The center of mass vector can be obtained in an analogous fashion. In this case we have  $A(\mathbf{r}\sigma q) = \mathbf{r}/(Z + N)$  which yields

$$\langle \mathbf{R}_{cm} \rangle = \frac{1}{A} \int d^3r \rho(\mathbf{r}) \mathbf{r} \quad (173)$$

which leads to the following relations in cylindrical coordinates

$$\langle z_{cm} \rangle = \frac{1}{A} 2\pi \int_0^\infty r dr \int_{-\infty}^\infty dz z \rho(r, z), \quad \langle r_{cm} \rangle = \frac{1}{A} 2\pi \int_0^\infty dr r^2 \int_{-\infty}^\infty dz \rho(r, z) \quad (174)$$

For the intrinsic quadrupole moment we have  $A(\mathbf{r}\sigma q) = e(\frac{1}{2} + q)(3z^2 - \mathbf{r}^2)$  from which we obtain

$$\begin{aligned} \langle Q_{zz} \rangle &= e \int d^3r (3z^2 - \mathbf{r}^2) \sum_{\sigma, \alpha} \sum_{q=\pm\frac{1}{2}} (\frac{1}{2} + q) |\phi_2(\alpha, \mathbf{r}\sigma q)|^2 \\ &= e \int d^3r (3z^2 - \mathbf{r}^2) \rho_p(\mathbf{r}) \end{aligned} \quad (175)$$

In the case of axially symmetry nuclei we find after transforming to cylindrical coordinates

$$\langle \frac{Q_{zz}}{e} \rangle = 2\pi \int_0^\infty r dr \int_{-\infty}^\infty dz (2z^2 - r^2) \rho_p(r, z) \quad (176)$$

## REFERENCES

- [1] DOE/NSF Nuclear Science Advisory Committee, *Opportunities in nuclear science, a long-range plan for the next decade*, US Dept. of Energy, 2002.
- [2] G. Audi and A.H. Wapstra, Nuclear Physics **A565**, 1 (1993).
- [3] A.C. Mueller and B.M. Sherrill, Ann. Rev. Nucl. Part. Sci. **43**, 529 (1993).
- [4] *Scientific opportunities with an advanced ISOL facility*, Technical report, ORNL, 1997.
- [5] J. Dobaczewski, H. Flocard and J. Treiner, Nucl. Phys **A422**, 103 (1984).
- [6] J. Dobaczewski, W. Nazarewicz, T.R. Werner, J.F. Berger, C.R. Chinn and J. Dechargé, Phys. Rev. **C53**, 2809 (1996).
- [7] K.L. Kratz , J.P.Bitouzet, P. Möller and B. Pfeiffer, Astrophys. J. **403**, 216 (1993).
- [8] W.M. Howard , S. Goriety, M. Rayet and M. Arnould, Astrophys. J. **417**, 713 (1993).
- [9] RIA Physics White Paper, Technical report, RIA 2000 Workshop, Raleigh-Durham, NC, 2000.
- [10] P. Navratil, B.R. Barrett and W.E. Ormand, Phys. Rev **C56**, 2542 (1997).
- [11] D. D. S.E. Koonin and K. Langanke, Phys. Rep. **1**, 278 (1997).
- [12] K.T.R. Davies, K.R.S. Devi, S.E. Koonin and M.R. Strayer, Vol. 3, in *Treatise on Heavy Ion Science*, edited by D. Bromley, volume 3, page 3, Plenum, New York, 1985.
- [13] J.W. Negele, Rev. Mod. Phys. **54**, 913 (1982).
- [14] B.D. Serot, Rep. Prog. Phys. **55**, 1855 (1992).
- [15] P. Ring, Prog. Part. Nucl. Phys. **37**, 193 (1996).
- [16] W. Pöschl, D. Vretenar, G.A. Lalazissis and P. Ring, Phys. Rev. Lett. **79**, 3841 (1997).
- [17] P.-H. Heenen and R.V.F. Janssens, Phys. Rev. **C57**, 159 (1998).
- [18] J. Terasaki, P.-H. Heenen, H. Flocard and P. Bonche, Nucl. Phys. **A600**, 371 (1996).
- [19] J.L. Egido and L.M. Robledo, Phys. Rev. Lett. **70**, 2876 (1993).
- [20] M.V. Stoitsov, J. Dobaczewski, P. Ring and S. Pittel, Phys. Rev. **C61**, 034311 (2000).
- [21] C.R. Chinn, J.-F. Berger, D. Gogny and M.S. Weiss, Phys. Rev. C **45**, 1700 (1992).
- [22] P. Ring and P. Schuck, editor, *The Nuclear Many-Body Problem*, Springer Verlag, New York, 1980.

- [23] J.-P. Blaizot and G. Ripka, editor, *Quantum theory of finite systems*, The MIT Press, Cambridge, MA, 1986.
- [24] A. L. Fetter and J. D. Walecka, editor, *Quantum theory of many-particle systems*, McGraw Hill, New York, 1971.
- [25] J. Bardeen, L. N. Cooper and J. R. Schrieffer, *Phys. Rev.* **108**, 1175 (1957).
- [26] K. Bennaceur, J. Dobaczewski and M. Płoszajczak, *Phys. Rev.* **C60**, 034308 (1999).
- [27] S. T. Belyaev, Introduction to the Bogoliubov canonical transformation method, in *The Many-Body Problem*, edited by C. DeWitt, 1959.
- [28] W. Nazarewicz, J. Dobaczewski, T.R. Werner, J.A. Maruhn, P.-G. Reinhard, K.Rutz, C.R. Chinn, A.S. Umar and M.R. Strayer, *Phys. Rev.* **C53**, 740 (1996).
- [29] L. D. Landau, *Sov. Phys. JETP* **8**, 70 (1959).
- [30] A. B. Migdal, editor, *Theory of finite Fermi systems and Applications to atomic nuclei*, Wiley Interscience, New York, 1967.
- [31] N. N. Bogoliubov, *Sov. Phys. JETP* **7**, 41 (1958).
- [32] J. G. Valatin, *Nuovo Cimento* **7**, 843 (1958).
- [33] R. Smolańczuk and J. Dobaczewski, *Phys. Rev.* **C48**, R2166 (1993).
- [34] J. Dobaczewski (private communication).
- [35] P.-G. Reinhard, D.J. Dean, W. Nazarewicz, J. Dobaczewski, J. A. Maruhn and M.R. Strayer, *Phys. Rev.* **C60**, 014316 (1999).
- [36] D. Gogny, in *Proceedings of the International Conference on Nuclear Physics*, edited by J. De Boer and H. J. Mang, North Holland, Amsterdam, 1973.
- [37] J. Dechargé and D. Gogny, *Phys. Rev.* **C21**, 1568 (1980).
- [38] V.E. Oberacker and A.S. Umar, *Perspectives in Nuclear Physics*, pages 255–266, World Scientific Publ. Co., 1999.
- [39] T. H. R. Skyrme, *Phil. Mag.* **1**, 1048 (1956).
- [40] D. Vautherin and D.M. Brink, *Phys. Rev.* **C5**, 626 (1972).
- [41] T. H. R. Skyrme, *Nucl. Phys.* **9**, 615 (1959).
- [42] J. Bartel, P. Quentin, M. Brack, C. Guet and H.B. Håkansson, *Nucl. Phys.* **A386**, 79 (1982).
- [43] L. Friedrich and P.-G. Reinhard, *Phys. Rev.* **C33**, 335 (1986).
- [44] F. Tondeur, M. Brack, M. Farine and J. M. Pearson, *Nucl. Phys.* **A420**, 297 (1984).

- [45] E. Chabanat, P. Bonche, P. Haensel, J. Meyer and R. Schaeffer, Nucl. Phys. **A635**, 231 (1998).
- [46] P.-G. Reinhard and H. Flocard, Nucl. Phys. **A584**, 467 (1995).
- [47] M. Bender, P.-G. Reinhard, M. R. Strayer and W. Nazarewics, (in preparation).
- [48] D.R. Kegley, PhD thesis, Vanderbilt University, 1996.
- [49] D. Vautherin and D. M. Brink, Phys. Rev. **C7**, 296 (1973).
- [50] A.S. Umar, M.R. Strayer, J.-S. Wu, D.J. Dean and M.C. Güçlü, Phys. Rev. **C44**, 2512 (1991).
- [51] A.S. Umar, J. Wu, M.R. Strayer and C.Bottcher, J. Comp. Phys. **93**, 426 (1991).
- [52] J.C. Wells, V.E. Oberacker, M.R. Strayer and A.S. Umar, Int. J. Mod. Phys. **C6**, 143 (1995).
- [53] D.R. Kegley, V.E. Oberacker, M.R. Strayer, A.S. Umar and J.C. Wells, J. Comp. Phys. **128**, 197 (1996).
- [54] J. Dudek, Z. Szymanski, T. Werner, A. Faessler and C. Lima, Phys. Rev. **C26**, 1712 (1982).
- [55] P. Bonche, S. E. Koonin and J. W. Negele, Phys. Rev. **C13**, 1226 (1976).
- [56] M. V. Stoitsov (private communication).
- [57] E. Teran, V.E. Oberacker and A.S. Umar, Heavy Ion Physics **6**, 437 (2002).
- [58] E. Teran, V.E. Oberacker and A.S. Umar, Submitted to Phys. Rev. **C** (2003).
- [59] T.R. Werner, J.A. Sheikh, W. Nazarewicz, M.R. Strayer, A.S. Umar and M. Misu, Phys. Let. B **333**, 303 (1994).
- [60] S. Mizutori, J. Dobaczewski, G.A. Lalazissis, W. Nazarewics and P.-G. Reinhard, Phys. Rev. **C61**, 044326 (2000).
- [61] A.S. Umar, M.R. Strayer, R.Y. Cusson, P.-G. Reinhard and D.A. Bromley, Phys. Rev. **C32**, 172 (1985).
- [62] C.Bottcher, M.R. Strayer, A.S. Umar and P.-G. Reinhard, Phys. Rev. **A40**, 4182 (1989).